Universidad de Concepción
Facultad de Ciencias Físicas y Matemáticas
Magister en Ciencias con Mención en Física

Tesis para optar al grado de Magíster en Ciencias con mención en Física

Effects of Gas Dynamics on the Evolution of Young Embedded Star Clusters

Juan Pablo Farías Osses

Profesor Guía:
Dr. Michael Alois Dominik Fellhauer

Departamento de Física
Facultad de Ciencias Físicas y Matemáticas
Universidad de Concepción
Chile

Concepción, Marzo 2016

Agradecimientos

Firstly, I would like to thank my supervisor, Dr. Michael Fellhauer, for his trust in my work and consideration on all my ideas. Thanks for your constant push-forward that have taught me a lot to trust in myself. And thanks also for all the beers!. Thanks to Dr. Inti Pelupessy, for all his patience and everything he taught me. I couldn't have done much without his help.

Quisiera agradecer además, a mis padres Eleodora Osses y Lizandro Farías por su apoyo incondicional durante toda mi carrera hasta en los momentos mas difíciles. A mi hermano Felipe por ayudarme siempre que lo necesité y a mis hermanos Rosa y Lizandro por toda su ayuda y por sus sabios y siempre acertados consejos. Gracias a toda mi gran familia por su apoyo y unidad que nos a sacado adelante a todos.

No puedo dejar de agradecer a mi esposa Daniela por su comprensión y apoyo durante todo este proceso. Agradezco, especialmente, a mi hija Luna, que con su contagiosa alegría es la razón para levantarnos en las mañanas.

Gracias además al soporte financiero recibido de CONICYT a través de Becas de Magíster Nacional, que he recibido durante todo el programa.

UNIVERSIDAD DE CONCEPCIÓN

Resumen

Facultad de Ciencias Físicas y Matemáticas
Departamento de Física

Efectos de la Dinámica de Gases en la Evolución de Cúmulos Estelares Jóvenes

por Juan Pablo Farías

Es sabbido que la mayoría de las estrellas se forman en cúmulos, asociaciones o grupos dentro de nubes moleculares. Sin embargo, solo pocos cúmulos estelares mayores que $\sim$ 5 millones de años están todavía asociados con su gas natal. Esto y el hecho de que no vemos solo cúmulos en el cielo nos lleva a pensar que la expulsión del gas es la principal razón de la destrucción de estos cúmulos jóvenes.

En esta tesis, examinamos la respuesta de cúmulos estelares inicialmente subestructurados a la expulsión instantánea de su gas. Modelamos el gas de fondo utilizando tres diferentes métodos: Usando potenciales de fondo esféricos y estáticos, una esfera gaseosa de Plummer capaz de evolucionar dinámicamente, y realizando simulaciones de formación estelar para obtener un gas de fondo en forma de filamentos desde el cual las estrellas se formaron. Nos concentramos en los efectos de la dinámica del gas en la fase anterior a la expulsión del gas y estudiamos el estado de estos cúmulos al momento de la expulsión del gas para ver si es posible estimar la masa ligada que los cúmulos pueden retener después de expulsar el gas. Estudiamos como las propiedades del gas de fondo así como el componente estelar la tendencia empírica entre la fracción de la masa total que permanece ligada y la fracción estelar local (i.e. la fracción de masa estelar dentro del radio que contiene la mitad de la masa estelar) encontrado en estudios anteriores.

Hemos encontrado que esta tendencia empírica es altamente afectada por el estado dinámico del cúmulo cuando la expulsión del gas comienza, y hemos desarrollado un modelo analítico simple que describe como esta tendencia cambia. También hemos encontrado que la interacción gravitatoria entre las estrellas y el gas por si sola asi como la forma en que el gas esta distribuido no afectan nuestra habilidad para estimar la masa que finalmente permanecerá ligada. Sin embargo, la distribución y forma del gas de fondo así como la forma en que el gas de fondo es modelado, tienen grandes consecuencias en como los cúmulos estelares se "preparan" para la expulsión del gas, i.e., la evolución previa a la expulsión del gas y por ende el estado de los cúmulos al momento de expulsar el gas es altamente afectada por el gas de fondo.

Mostramos que nuestro modelo analítico es capaz de hacer estimaciones con un 10% de precisión para expulsión de gas instantánea sin importar las condiciones del cúmulo, y los factores más (igualmente) importantes que gobiernan la respuesta de cúmulos estelares a la expulsión del gas son la fracción estelar local y el estado dinámico de los cúmulos, ambos medidos al momento de la expulsión del gas.

UNIVERSIDAD DE CONCEPCIÓN

Abstract

Facultad de Ciencias Físicas y Matemáticas
Departamento de Física

Effects of Gas Dynamics on the Evolution of Young Embedded Star Clusters

by Juan Pablo Farías

It is known that almost all stars form in clusters, associations or groups inside molecular clouds. However, just a few of the star clusters older than ~ 5 Myr are still associated with their natal gas. This and the fact that we do not see only clusters in the sky leads us to think that gas expulsion is the principal reason for the destruction of these young clusters. We examine the response of initially substructured star clusters to instantaneous gas expulsion. We model the background gas using three different treatments: Utilizing static and spherical background potentials, a dynamically live Plummer sphere of gas, and performing star formation simulations to obtain a filamentary background gas from which stars are formed. We focus on the effects of gas dynamics in the pre-gas-expulsion phase and study the state of these clusters at the moment of gas expulsion to see if it is possible to estimate the final bound mass that clusters can retain after gas expulsion. We study how the properties of the background gas as well as the stellar component affects the empirical trend between the bound fraction and the local stellar fraction (i.e. the fraction star mass inside the stellar half mass radius) found in previous studies.

We find that this empirical trend is heavily affected by the dynamical state of the cluster when gas expulsion begins, and we developed a simple analytical model that describes how this trend changes. We also find that gravitational interactions between stars as well how the gas is distributed does not affect our ability to estimate the final bound mass. The distribution and shape of the background, as well the way the background gas is modeled, have big consequences in how star clusters "prepare" themselves to gas expulsion, i.e.,the pre-gas-expulsion evolution and thus the state of the clusters at the moment of gas expulsion is heavily affected by the background gas.

We show that our analytical model is able to make estimations with a 10% of accuracy to instantaneous gas expulsion no matter the conditions of the cluster, and the most (equally) important factors that rules the response of a star cluster to gas expulsion are the local stellar fraction and the dynamical state of the clusters, both measured at gas expulsion time.

Contents

List of Figures

List of Tables

Chapter 1

General Introduction

1.1 Star Clusters

Star clusters are basically groups of stars. Those stars are born more or less at the same time in the same molecular cloud. That is the reason why they are so interesting. As they have similar ages and chemical abundances they are an excellent laboratory to test our understanding of star formation and stellar evolution. They are also been used as distance calibrators and the motion of its members help us to understand galactic dynamics. It is this last field where we are specially interested and in this chapter we wish to provide a general idea about star clusters, the concepts and background about the specific field that we are interested in, i.e., the *Infant Mortality* problem.

1.1.1 Types of Star Clusters

As in many other fields in astronomy, the first thing to do is to classify the different types of star clusters. Observationally, they have been classified by their proprieties like the total mass, number of stars, age among many others. The most important types are: Globular Clusters, Open Clusters, T-associations, OB-Associations and Embedded Clusters.

Globular Clusters (GC) are the most massive clusters and the oldest systems with ages of ~ 10 Gyr and more. Even the smallest of them contain 10^4 $M_\odot$ in stars and a few, like Omega Centauri (see left picture of Fig: 1.1) contain $\sim 10^6$ $M_\odot$. A typical tidal radius

Figure 1.1: Two examples of star clusters. **Left:** The GC Omega Centauri, one of the biggest GCs in our galaxy with 4.6×10^6 M$_\odot$. **Right:** The open cluster M25, an example of an OC with thousands of stars and 90 Myr old (in comparison with the $\sim$ 11 Gyr of Omega Centauri).

is about 35 parsecs and some GCs are so dense that star collisions are common inside their nuclei (Maxwell et al., 2012; Chatterjee et al., 2013). They are usually spherical and are distributed in the halo of our Galaxy (Harris, 1996).

Open Clusters (OC) are usually less massive than GCs, their masses fluctuate from $\sim 10^2$ to 10^4 M$_\odot$ and they are young (less than 1 Gyr). Few open clusters have enough members to characterize their size by a dynamically meaningful quantity, such as the core radius or tidal radius. Instead open clusters sizes are based on the apparent angular size of the cluster. However they are usually irregular distributions (see right picture of Fig: 1.1) and characterization by a radius is not always representative. Nevertheless, there is a rather small spread in measured cluster diameters with typical diameters between 4 to 5 pc. They are usually weakly bound and are strongly affected by external forces. We can find them in the disk of our Galaxy.

OB-associations are areas in the sky with a higher than normal concentration of O and B stars. Unlike GCs and OCs they are unbound systems that contain thousands of stars on a volume of the sky of dozens of parsecs.

T-associations consist mostly of T-Tauri stars that are in the pre-main sequence stage of their evolution. They have mostly low mass stars and are the are smallest populations containing usually less that 100 members. T-associations are still embedded in their natal gas.

Embedded Clusters (ECL) are just forming star clusters that are still embedded in their molecular cloud. They are small in size, from one to few dozens of parsecs, but also quite dense in mass. It is not only the stars (containing hundred to thousands of stars) but also the gas mass that keeps the cluster bound and compact. They contain mostly pre main sequence stars of all kinds and they are only observable through IR imaging.

1.1.2 The Relevance of Star Clusters

Most of stars form in groups of a wide range of sizes and masses (Lada and Lada, 2003; Bressert et al., 2010) and thus most of star forming regions, if not all, contain star

Table 1.1: A summary table of the typical parameters of the different star clusters. Numbers in the columns are for comparison purposes and should be used with care, but they provide some flavor of the various cluster types.

	Globular Cluster	Open Cluster	OB associations	T associations	Embedded Cluster
Age [yr]	$\gtrsim 10^9$	$10^6 - 10^9$	$\lesssim 10^6$	$\lesssim 10^6$	$\lesssim 10^5$
Mass [M$_\odot$]	$10^4 - 10^6$	$10^2 - 10^4$	$10^3 - 10^4$	~ 100	$10^2 - 10^4$
Size [pc]	10-100	$\lesssim 10$	$\gtrsim 100$	< 100	$\lesssim 5$
Members	$10^5 - 10^6$	$10^3 - 10^5$	$10^3 - 10^5$	10-100	$10^2 - 10^5$
Star types	Solar Types stars and Red Giants	B,A,F, Red Giants	All kinds of stars	Low mass stars, T Tauri stars	Pre-main sequence Stars of all masses
Location	Halo of Milky Way	Disk of Milky Way	Near Giant Molecular Clouds	Near Dark Clouds	Inside Molecular Clouds

clusters. Building a coherent picture of how clusters form and evolve is critical to our overall understanding of the star formation process.

After they form most cluster disrupt contributing to the field star population of their host galaxy, but some of them remain bound and dense enough to survive for a Hubble time. These surviving clusters provide an invaluable laboratory of stellar dynamics and stellar evolution. It is impossible to follow the evolution of individual stars observationally since timescales are far too long. In star clusters all the members are born at approximate the same time, from ~ 0.3 to 10 Myr depending of the size of the region where they form (Elmegreen et al., 2000), in comparison with the age of the cluster ($\gtrsim 1$ Gyr for a typical GC) with the same chemical composition since they are born from the same material. The only difference between members is then their individual mass.

Because the size of a cluster is typically small compared to its distance from us, all the stars in a given cluster are also effectively at the same distance. This fact is crucial, because it means that the relative brightness of the stars are well-known, even if the distance itself is poorly determined and the absolute luminosities are not known. We can construct a colour-magnitude diagram for a cluster without having to know the zero point of the magnitude scale. The shapes of the colour-magnitude diagram are very different for open and globular clusters.

Stars in open clusters lie on a very narrow main sequence band from low mass stars to high mass stars with a few stars in the giant region of the diagram. Globular clusters instead have a much less prominent main sequence without massive stars, where all the massive stars lie in a well populated giant branch and horizontal branch. These differences are interpreted as age differences with the open clusters being younger. The age of a cluster is therefore equal to the main sequence lifetime of the most massive stars still on the main sequence (called *turn off point*. If we measure the luminosity off the turn off point on the main sequence, and use the mass luminosity elation to find the corresponding mass, then we know the age of the cluster. Most of our knowledge about stellar evolution comes from this interpretation and any stellar evolution model needs to explain the shape of the color-magnitude diagram found in star clusters.

Star clusters are also important in the *cosmic distance ladder* which refers to the different methods of measuring Galactic and extragalactic distances based on distances known by “simpler” methods like paralax. It is possible to measure distances to globular clusters using the colour-magnitude diagram if the distance to one single cluster is well known by a different method. The colour-magnitude diagram of two clusters will in general have the same shape (for the main sequence), but will be shifted in magnitude by an amount equal to the difference in distance modulus between the two. There may also be additional shifts in magnitude and color index resulting from stellar absorption. The general procedure is to apply the effects of absorption, if known, and then slide the diagrams of the two clusters. This method is only an example of how star clusters are used to measure distances. There are other methods as well like the globular cluster luminosity function (Whitmore, 1997) or the moving cluster paralax for nearby clusters (Narayanan and Gould, 1999). Even though these methods are quite old and now there better methods for distance estimation, star cluster were the bottom of the cosmic distance ladder for a long time.

1.2 Brief Overview on Star Cluster Formation

As we saw, star clusters have been quite useful for our understanding of the Universe. However, how they are formed has remained as an open question for a long time. One main difficulty is the fact that star cluster formation is closely linked to the star formation process for which there is not yet a complete theory. The astronomical community has made their best to understand this process and hence astronomers have "split" their efforts into two different, but closely related, ways of study this problem in an empirical fashion: Observationally and numerically.

Observations have been crucial along history to our understanding about the Universe, pushing our way to think to new levels, since most of the time we don't understand what we see and other times confirming what we think it should happen. In the past three decades with the advance of technology and developing of powerful computers, new tools are born in order to help us understand what we see. Numerical simulations of star clusters are developing enormously in the past three decades starting from the three body problem in the early 70's until now the possibility to follow the dynamical evolution of a million bodies. Another remarkable advance in the last two decades has been the possibility to simulate astrophysical gas through hydrodynamical simulations.

In this section we wish to quickly overview our general knowledge about SC formation from these two perspectives with their individual current limitations.

1.2.1 Observations

The first thing necessary to understand the process is acquiring a detailed empirical knowledge from observations to new born star clusters. This is not possible for all the types of clusters we know. Consider, for example, the GCs that are the most massive stellar clusters in the Milky Way. These systems are more than 12 Gyr old and are no longer formed in our Galaxy. Thus we can not obtain direct observations of their formation process in our Galaxy. However, observations of star forming galaxies as the "Antennae" galaxies (Whitmore and Schweizer, 1995), NGC 1275 (Holtzman et al., 1992) and many others (e.g. Larsen and Richtler, 1999), reveal populous systems of compact and massive young star clusters, with all the properties of young globular clusters. This evidence shows that small compact and massive clusters forms wherever there is vigorous star formation. While these and many other observations clearly show where and when dense star cluster form, observing the details of their formation is for now technically not possible.

The situation is considerably better for OCs where the typical ages range from 1 Myr to 1 Gyr. These clusters are still forming in the Milky Way so a direct observational study of their formation process is possible. The main problem of studying their formation and early evolution is that at these stages OCs are completely embedded in molecular gas and dust. They are thus obscured from view at optical wavelengths, where the traditional astronomical techniques are more effective. In the past two decades technology and techniques in the IR imaging, where molecular clouds and dust are considerably less opaque, made enormous advances enabling astronomers to survey and systematically study extreme young embedded clusters in nearby molecular clouds. These studies indicate that embedded clusters are quite numerous and they account for a significant fraction, if not the majority, of star formation present in the Milky Way.

Observations suggest that star formation is a highly inefficient process, current estimates imply that star formation efficiencies (i.e. the amount of gas that turn into stars) is in general less than 30% (Carpenter, 2000; Lada and Lada, 2003; Evans et al., 2009; Tsitali et al., 2010). Why is this process so inefficient is a matter of debate and not well understood yet. Numerical studies, however, offers new tools to understand this contraint as we will se later.

Estimation of the ages and positions of the stars inside star clusters suggests that the timescales for star cluster formation correlates with the size of the region S by a power law of 0.5 as shown in Fig. 1.2 (Efremov and Elmegreen, 1998). Bigger star forming regions form stars for a long period of time. This relationship implies that cluster that form together in small regions will usually have about the same age, whereas clusters that form together in larger regions will have a wider range of ages. Relations between ages and region sizes show a slopes significantly lower than what one would expect for simple crossing times arguments (Efremov and Elmegreen, 1998; Elmegreen et al., 2000) together with the supersonic spectral linewidths found in molecular clouds suggest that the star formation process is largely influenced by supersonic turbulence (Zuckerman and Evans, 1974).

Turbulence in molecular clouds tends to form multiple overdensities that grow enough to fulfill the Jeans instability criterion, i.e., gravity overcomes the internal thermal pressure of the gas cloud leading to further fragmentation and collapse that at the end will turn into proto-stellar cores.

Further observations have shown that clouds do not only collapse spontaneously, pressure shock waves ,e.g. coming from a supernovae explosion, could raise local densities enough to become Jeans instable. This scenario is referred as “triggered” star formation (Elmegreen and Lada, 1977).

Another key in the star cluster formation process is the initial mass function (IMF) that stars form. The IMF indicates how much stars form in a specific mass range. Observations have shown that the IMF remains remarkably invariant. The same form is present in dense clusters and sparse associations and in open and globular clusters. All of these IMFs are also consistent with the mass function in the Galactic field, however there is yet no evidence that can clearly show that the IMF is either universal or not in space and time (see Bastian et al., 2010, for a complete review and discussion).

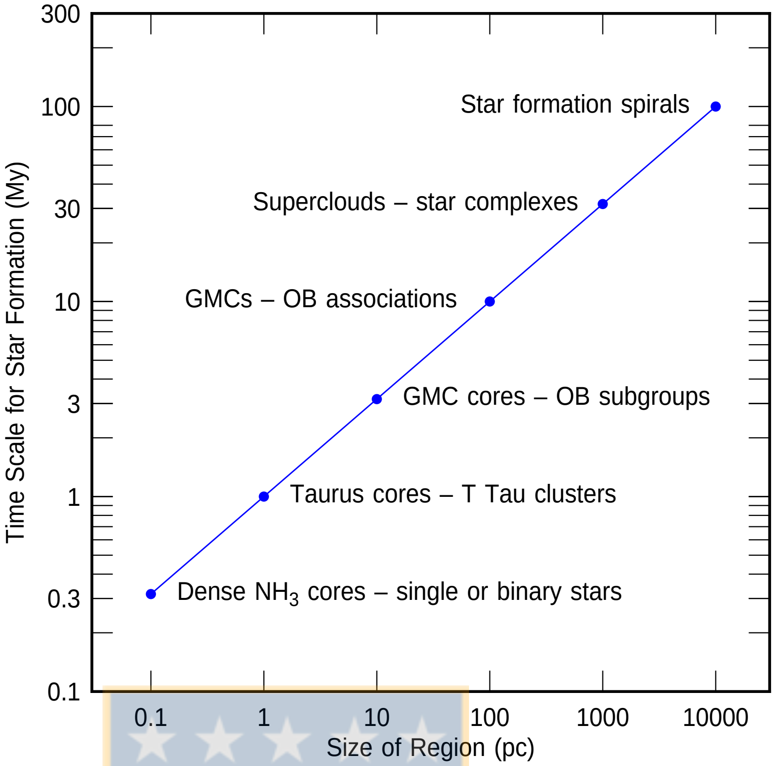

Figure 1.2: Schematic diagram of the relationship between the duration of star formation and the region size (from Efremov and Elmegreen, 1998). Larger regions of star formation form stars for a longer total time

1.2.2 Numerical Studies

While most of the constrains involving cluster formation comes from observations, is impossible to observe the whole process since the timescales are too long. Only in the last fifteen years with the advance in computing power it has been possible to move from simulations on the formation of individual stars and binaries to formation of SCs. However, even with the high-performing-computing facilities is not yet possible to follow the collapse of molecular clouds down to stellar densities in their full complexity. Thus, all simulations of star cluster formation lack of several physical processes or use several approximations, however much can be learned for such “simple” numerical experiments.

First attempts usually model the collapse of molecular clouds utilizing either a barotropic or isothermal equation of state approximation done to emulate the radiative cooling necessary for a cloud to collapse. Since there is observational evidence of supersonic turbulence in molecular clouds (Zuckerman and Evans, 1974) which source is still not well established, initial velocities for the gas are usually chosen to be randomly turbulent with some power spectrum $P \propto k^{-\alpha}$, where k is the wavenumber of the perturbation, i.e., the energy of the full velocity perturbation is distributed mainly in the big or at all scales depending on the power law (normally chosen between $\alpha = 0$ and 4). Then star formation is emulated through “sink” particles of a defined sink radius where bound gas is accreted (Bate et al., 1995). This radius is usually chosen in terms of the resolution limit, the size of the cloud and the computing power, varying from ~ 5 to 50 AU depending of the physical process they are focused on. Thus sink particles can not always be interpreted as protostars, depending of the sink radius they could be interpreted as proto-clusters or even clusters depending of the scale of the simulation. Conditions for the accretion of gas varies between the authors, however all of them agree that gas entering the sink radius need to be at least gravitationally bound to the sink particle to be accreted.

Such simulations have recreated surprisingly well the observed IMF even though no feedback is included, (Bate et al., 2003). They have shown evidence of the "competitive accretion" model first idealized by (Bondi and Hoyle, 1944) which states that low mass sink particles are ejected from gas rich regions due to close encounters truncating their accretion history. Instead high mass stars rapidly mass segregate to dense gaseous regions accreting gas for longer times.

Several studies have experimented with the initial conditions of the cloud, varying the power spectrum of the turbulent velocity field, the Mach number (i.e. the typical gas velocity in comparison with the local sound speed) and the global boundness of the cloud (i.e. the ratio of the kinetic plus thermal energy to the potential energy) finding no statistical difference between the resulting cluster morphology (Schmeja and Klessen, 2006; Girichidis et al., 2012; Klessen and Burkert, 2001) or neither in the resulting IMF (Bate, 2009).

Such simulations obtain star formation rates several times bigger than observed (see Padoan et al., 2014). Without any artificial truncation those simulations would get star formation efficiencies of 100% which are not real. Several efforts have been made in order to understand what stops or slows down the formation of stars, finding that there are several mechanisms that can prevent star formation. Simulations have shown that several factors could stop or diminish star formation: Where driven turbulence is strong enough to prevent local collapse (high Match numbers), the global boundness of the cloud seems to be the more important. Magnetic fields could also prevent collapse, however, it has been shown that it is a secondary effect (Klessen and Burkert, 2000; Padoan and Nordlund, 2011; Padoan et al., 2012; Federrath and Klessen, 2012). Radiative feedback from stars could also affect star formation. This influence has been shown to be strongly dependent of the size and density of the cloud, i.e., how big are the escape velocities in a cloud (see Dale et al., 2013, series of papers).

There is no simulation to date that can emulate all the relevant physical processes present in molecular clouds. However, we have seen how much we can learn from adding or studying one physical process at the time. Before we have the capabilities of a realistic simulation, it is important that we know exactly which physical process can influence the results to what limits, so when technology develops enough to perform a realistic simulation we are able to identify the consequences of each process.

1.3 Basic Concepts of Stellar Dynamics

The objective of this section is to introduce some basic definitions regarding to star clusters that will be used and discussed in the present thesis.

1.3.1 The Virial Ratio

The virial theorem applied to stellar clusters, states that a system is in *virial equilibrium* if:

$$T_* = -\frac{1}{2}\sum_{\mathrm{i}=1}^{N}\mathbf{F}_{\mathrm{i}}\cdot\mathbf{r}_{\mathrm{i}} \tag{1.1}$$

$$= -\frac{1}{2}\Omega_{\mathrm{tot}} \tag{1.2}$$

where T_* is the kinetic energy of all stars in the cluster, $\mathbf{F}_{\mathrm{i}}$ is the force felt by the i^{th} particle by the other $N-1$ particles, $\mathbf{r}_{\mathrm{i}}$ is the position of the i^{th} star and Ω_{tot} is the total potential energy of the cluster (Aarseth, 2003). However, not all systems are in virial equilibrium hence a useful measure of the dynamical state of the cluster is the ratio between the kinetic energy and the total potential energy:

$$Q = -\frac{T_*}{\Omega_{\mathrm{tot}}}. \tag{1.3}$$

The ratio Q is called the *virial ratio* and it can be used to characterize the velocities of a system as well as to distinguish between a bound and an unbound system. Thus, depending of this value we call a system with:

$Q < 0.5$: A cold system. A highly bound system with low velocity particles.
$Q = 0.5$: A virialized system i.e. A system in virial equilibrium.
$Q > 0.5$ and $Q < 1$: A hot system. A loosely bound system with high velocity particles.
$Q > 1$: A unbound system where most of the particles have velocities higher than the escape velocity.

Another important quantity related to the virial theorem is the *virial radius* R_{v} defined for an isolated star cluster in terms of the potential energy, for an isolated system (Aarseth, 2003; Heggie and Hut, 2003):

$$R_{\mathrm{v}} = -\frac{GM_*^2}{2\Omega_*} \tag{1.4}$$

where M_* and Ω_* are the cluster mass and the potential of the isolated star cluster. This radius is useful since it is used as the unit of length by several N-body integrators.

1.3.2 The Collisional Regime

Star clusters are *collisional* systems, meaning that close encounters between two or more particles can strongly affect the dynamical evolution of the cluster. The formal definition of a collisional system requires the understanding of two basic concepts, the relaxation time and the crossing time:

The *crossing time* (t_{cross}) is the time that a typical particle needs to cross the system, i.e., $t_{\mathrm{cross}} = R/v$ where R is the size of the system and v is the typical speed of a star in the system. The value of v will depend of the dynamical state of the system, i.e. a hot system will have higher v than a cold system. However the crossing time is a timescale that is generally used to see how long a dynamical process can last, so it usually is estimated assuming virial equilibrium and spherical symmetry, since we usually do not need the *exact* value.

A typical velocity on a stellar system is the velocity dispersion (σ) of the particles, assuming virial equilibrium we can define the crossing time as (see Aarseth, 2003):

$$t_{\rm cross} \approx 2\frac{R_{\rm v}}{\sigma} \tag{1.5}$$

In virial equilibrium we can estimate the value of σ by $\sigma^2 \approx GM/2R_{\rm v}$ where G is the Newton's gravitational constant and M the total mass of the cluster. Thus the crossing time can be estimated as (Aarseth, 2003; Heggie and Hut, 2003):

$$t_{\rm cross} \quad \approx \quad 2\sqrt{\frac{R_{\rm v}^3}{2GM}} \tag{1.6}$$

This last equation is particularly useful in numerical simulations since a typical N-Body code chose to use units such that $G = 1$, $M = 1$ and $R_{\rm v} = 1$ and thus $t_{\rm cross} = \sqrt{2}$.

The *relaxation time* ($t_{\rm relax}$) is the time-scale where a system looses its memory of its initial state. It is also defined as the typical time-scale that a system needs to reach dynamical equilibrium or to come back to equilibrium after been disturbed. An useful approximation of this time scale is derived in Binney and Tremaine (1987) as follows:

$$t_{\rm relax} \quad \approx \quad \frac{0.1N}{\ln N} \times t_{\rm cross} \tag{1.7}$$

For galaxies with $N \approx 10^{11}$ stars and an age of approximately 10 Gyr and a few hundred crossing times old, the relaxation time-scale for the whole system is much longer than the age of the Universe, in these systems it is possible to neglect the contribution from close encounters, that is what we call a *collisionless* system. On the other hand a GC with $N \approx 10^5$ members and a relaxation time of $t_{\rm relax} \approx 100$ Myr, close encounters may be important over the lifetime of the cluster of ~ 10 Gyr and we can't ignore close encounters, that is what we call a *collisional* system.

In general a system is called collisional when their lifetime or the time range that we are interested on $t_{\rm life} \gg t_{\rm relax}$, and collisionless when $t_{\rm life} \ll t_{\rm relax}$. In this thesis we focus on highly collisional systems, so we need to follow their evolution accordingly.

1.4 Hydrodynamical Equations

As we will see later, in this thesis we will be focus on simulating the natal gas where stars form and evolve. In this section we will introduce the basic hydrodynamical equations that describe the evolution of such fluids. We will focus on self gravitating, compressible fluids as it the kind of fluid that embedded star clusters are born, thus for clarity we will refer to it as *gas*.

Any gas element can be described by 4 independent variables, its density ρ, pressure P, velocity $\mathbf{v}$ and internal specific energy u. Since the velocity is a 3-D vector, then a gas element is described by 6 independent variables.

There exists two different approaches to describe a gas, the *Eulerian* and *Lagrangian* approach. In the first one a fluid element is described considering a spatially fixed volume element on which we see how the independent quantities change inside this volume. In the Lagrangian approach the volume element is followed along its path and see how it changes the internal properties along this way. Both approaches are equally valid and popular, however in this thesis we will focus on the Lagrangian approach, from which is necessary to introduce the *comoving time derivative* D/Dt as:

$$\frac{D}{Dt} \equiv \frac{\partial}{\partial t} + \nabla \cdot \mathbf{v}. \tag{1.8}$$

To describe the 6-D fluid we need to obtain 6 independent equations. We will briefly introduce these basic equations that any hydrodynamical integrator needs to solve:

The first equation is called the *continuity equation*:

$$\frac{D\rho}{Dt} = -\rho \nabla \cdot \mathbf{v} \tag{1.9}$$

this equation says that the density of the gas element will increase if the motion of the gas converges, i.e., when the gas is compressed. The compression of the gas is expressed by $-\nabla \cdot \mathbf{v}$. This equation is obtained assuming the conservation of mass inside the gas element.

Forces acting on the gas element are related through Newton's second law. The equation that relates all the forces acting on the gas element is called the *momentum* equation:

$$\frac{D\mathbf{v}}{Dt} = -\frac{1}{\rho}\nabla P - \nabla\phi + \zeta\nabla^2\mathbf{v} + f \tag{1.10}$$

where p is the pressure, ϕ the gravitational potential, ζ is a viscosity coefficient and f any external force. Note that this equation resumes three independent equations, one for each velocity component. The right hand side of Eq. 1.10 collects any forces that acts on the gas element. The first term says that pressure induce forces in a direction where the pressure diminish ($-\nabla P$), that is the same behaviour when considering a gravitational potential (second term). The third term is related to forces induced by viscosity, i.e., how a gas element interact with the neighbor gas elements. While in the molecular clouds that we will consider viscosity is not present, Lagrangian numerical integrators needs to include a small factor of viscosity in order to avoid singularities, handling shock waves, and because they usually transform a continuum medium into a discrete medium so it has been found empirically that the inclusion of a small artificial viscous factor improve the resulting simulations (Agertz et al., 2007). There are several ways to include and implement artificial viscosity, but we will not discuss this issue in this thesis (see Monaghan, 1992, for details). Any external force (e.g. magnetic fields) can be simply added in this equation as an extra term.

From the first law of thermodynamics we can obtain a fifth equation called the *energy equation*:

$$\frac{Du}{Dt} = T\frac{ds}{dt} - \frac{P}{\rho}\nabla \cdot \mathbf{v} \tag{1.11}$$

where T is the temperature and s is the specific entropy. This equation tell us that the internal energy of the gas element will increase if the specific entropy increases and if the gas element is compressed. Heating sources and cooling processes can be included in ds. Note that for an isolated adiabatic gas s is constant, thus the first term vanishes.

The sixth equation is the *equation of state* of the gas with the form $P = P(T, \rho, \dots)$. This equation is a matter of choice and depends of the kind of gas that we are dealing with. In this thesis we will work with two different equations, the *adiabatic* equation of state:

$$P = K\rho^{\gamma} \tag{1.12}$$

where K is a constant and γ is the adiabatic index, that for an ideal gas $\gamma = 5/3$. This equation described an isolated gas with no heating or cooling processes, we will also use the other extreme, where there exists some ambient temperature T to which the gas rapidly heats or cools when it is compressed or expanded. This situation is modeled by the *isothermal* equation of state that hold when we choose $\gamma = 1$ and P is linearly proportional to ρ:

$$P = K\rho \tag{1.13}$$

1.5 The “Infant Mortality” Problem

In this thesis we will focus on the end part of the star formation process. We have presented an overview about how star clusters form, however, embedded star clusters do not hold their natal gas for long. Even before forming stars that reach the main sequence, proto-stars already inject energy into the surrounding gas via proto-stellar jets, and when a massive star forms, large amounts of energy are radiated into the surroundings until at the end the first supernovae explodes and, depending of the size of the region, it could remove any remaining gas (see Lada and Lada, 2003).

It has been argued that the removal of gas (and hence a big fraction of the binding potential) is a very destructive process that disperses most of star cluster into the field (e.g Hills, 1980; Elmegreen, 1983; Verschueren and David, 1989). While observed age distributions of open and embedded star clusters within 2 kpc from the Sun show a large discrepancy with the predicted distributions through the assumption of a constant rate of star formation in the Galaxy (see Fig. 1.3). This discrepancy seems to confirm that most of star clusters do not survive gas expulsion suggesting that less than $\sim 4\%$ of embedded clusters are able to emerge from their native cloud (Lada and Lada, 2003). This destructive process has been termed the *Infant Mortality* problem.

1.5.1 Classical Picture

There have been several numerical studies investigating this problem (Goodwin, 1997; Kroupa et al., 2001; Geyer and Burkert, 2001; Baumgardt and Kroupa, 2007) and they have found that the two physical parameters that determine the survival of a young cluster to gas expulsion are the SFE ϵ:

$$\epsilon = \frac{M_*}{M_* + M_{\text{gas}}} \tag{1.14}$$

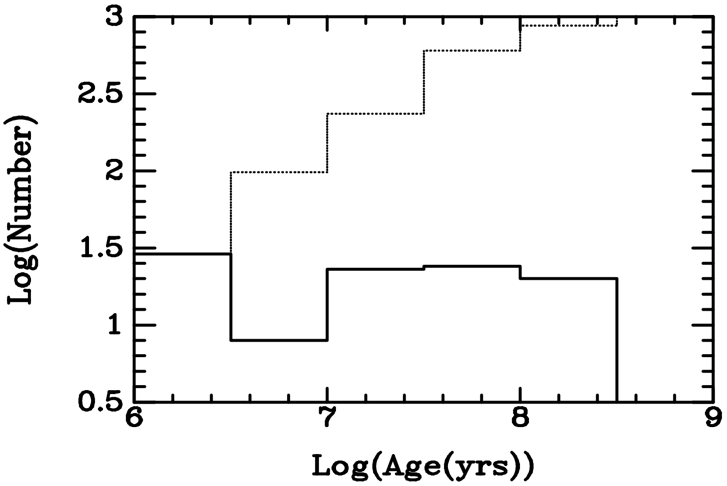

Figure 1.3: The discrepacy between the observed and predicted frequency distribtion of ages for open and embedded star clusters within 2 kpc of the Sun. Observed frequencies in (solid line) compared to that predicted for a constant rate of star formation adjusted for cluster luminosity evolution (dashed line). All embedded clusters fall into the first bin. The large discrepancy between the predicted and observed numbers indicates a high infant mortality ratio for protoclusters. Figure taken from Lada and Lada (2003).

and the timescale of gas expulsion $\tau_{\rm ge}$.

There are two important regimes for $\tau_{\rm ge}$ that correspond to explosive ($\tau_{\rm ge} \ll t_{\rm cross}$) and adiabatic ($\tau_{\rm ge} \gg t_{\rm cross}$) gas expulsion. Analytical and numerical studies show that when gas expulsion is explosive star clusters do not have time to react and stellar velocities become suddenly higher than the escape velocity ($Q \gg 1$) and it is unlikely for a star cluster to retain its members. In the adiabatic regime the star clusters have more time to adapt and pursue equilibrium in their new environment resulting in a high survival rate (see Verschueren and David, 1989; Baumgardt and Kroupa, 2007).

Clusters with a high SFE have more chances to survive since most of the binding energy is stored in the stellar component and the removal of gas may not increase the virial state of the cluster too much. It has been argued from an analytical point of view that clusters will survive gas expulsion only if they have SFE $\gtrsim 50\%$ (Elmegreen, 1983; Wilking and Lada, 1983) but a extensive parameter study performed by Baumgardt and Kroupa (2007) show that with explosive gas expulsion the minimum SFE that a cluster needs for not being completely destructed is actually a SFE of $\sim 35\%$ and about 10% in the adiabatic case.

The parameter study performed Baumgardt and Kroupa (2007) found clear relations between the SFE, $\tau_{\rm ge}$ and the fraction of the cluster mass that remain bound after gas expulsion $f_{\rm bound}$. Using their relations the SFE can then be used to estimate the lower limit of $f_{\rm bound}$ (assuming explosive gas expulsion), if it is possible to measure the SFE of a cluster. This study agreed with several similar numerical studies as we can see in Fig. 1.4 where the data in the literature is plotted together by Baumgardt and Kroupa (2007) for simulations with slow gas expulsion (left points) and explosive gas expulsion (right points). The data in Fig. 1.4 comes from Lada et al. (1984) (green open circles), Geyer and Burkert (2001) (orange open squared and triangles), Boily and Kroupa (2003) (blue filled circles), Fellhauer and Kroupa (2005) (pink filled triangles) and Baumgardt and Kroupa (2007) (black points).

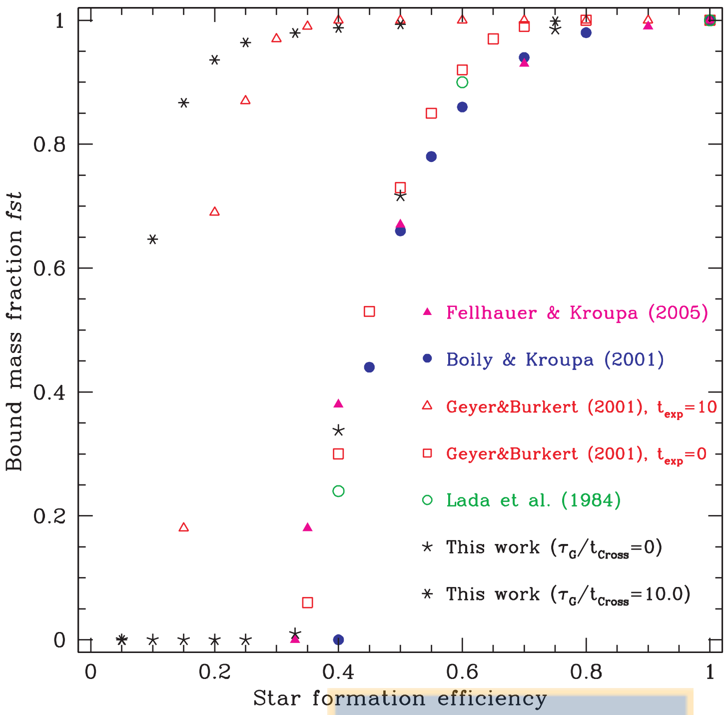

Figure 1.4: Comparison of surviving mass fractions from several numerical studies showing a very good agreement between the authors. For slow gas removal (left points,stars and open triangles) the critical SFE needed to produce a bound cluster is ∼ 10%. While for instantaneous gas expulsion (right points, filled and open circles, filled triangles and open squares) the critical SFE is ∼ 35%. Figure taken from Baumgardt and Kroupa (2007).

1.5.2 The Hierarchical Merging Scenario

The parameter study of Baumgardt and Kroupa (2007) and the general agreement by the authors about the relevance of the gas expulsion timescale and especially the SFE as shown in Fig. 1.4 give the idea that the infant mortality problem is quite well understood. However, most of the analytical and numerical models in the classical picture make very similar assumptions. All the numerical studies discussed in the previous section make use of very simple initial conditions, i.e., spherical distributions (Plummer or King models), virial equilibrium and static spherical background potentials to mimic the gas.

Smith et al. (2011) performed simulations of highly clumpy and fractal clusters distributions (see Goodwin and Whitworth, 2004) motivated by the observational and numerical evidence that star clusters form in highly substructred regions and also with subvirial velocities (e.g. Elmegreen and Elmegreen, 2001; Allen et al., 2007; Gutermuth et al., 2009; Bressert et al., 2010). The inclusion of an initially substrucured distribution increased the chances for a cluster to survive significantly. In this "Hierarchical Merging Scenario" fractal and clumpy distributions rapidly merge suffering a violent relaxation. In such a scenario a global parameter like the SFE fails to estimate $f_{\rm bound}$ as it did in previous studies as we can see in the left panel of Fig. 1.5, where for the same SFE simulations including primordial substructure show a wide range of cluster survival even at low SFE where the classical picture predicted no survival. This shows that in the hierarchical merging scenario the SFE fails to describe how well clusters survive gas expulsion.

The principal difference between spherical virialized star clusters and hierarchical distributions is that hierarchical star clusters (even with virial equilibrium velocities) are not in equilibrium as a spherical distributed cluster. They violently relax rearranging into an equilibrium distribution and such a process could take several crossing times. During this period star clusters expand and contract and a global parameter as the SFE does not give any information about the process. Having this in mind Smith et al. (2011)

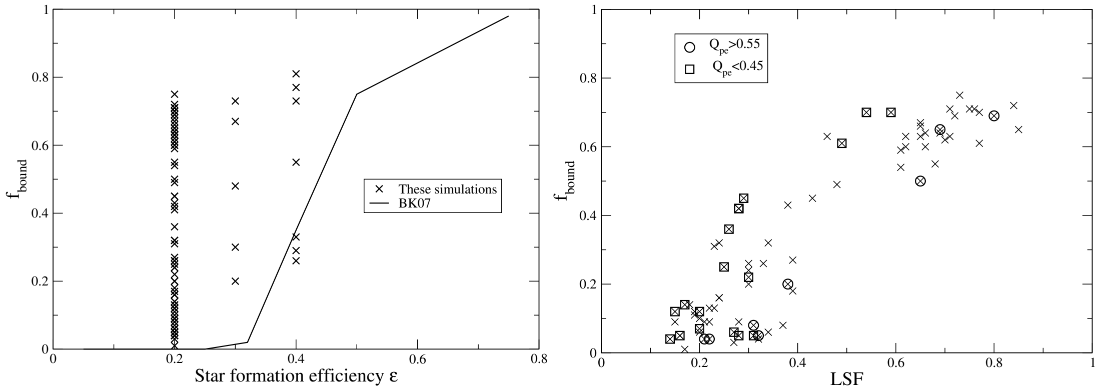

Figure 1.5: The difference in the results between the classical picture and the hierarchical merging scenario and the introduction of the LSF as a estimator of $f_{\rm bound}$. **Left** A comparison between the results of Baumgardt and Kroupa (2007) (solid line) and Smith et al. (2011) (crosses). For low SFE the classical picture predicts no survival, with the inclusion of primodial substructure there is a wide range of cluster survivals, the same happens at higher SFE. **Right** The LSF as an estimator of cluster survival introduced by (Smith et al., 2011). The LSF is a better estimator in the hierarchical merging scenario since it is able to evolve with the cluster. Different symbols show the extremes in virial ratio that cluster have when gas expulsion begins suggesting that the scatter in the trend could be due to the different Q that hierarchical cluster show when gas expulsion begins. Both figures are taken from Smith et al. (2011).

introduced another method of measuring the relative amount of mass in stars measuring the SFE only inside the half mass radius ($r_{\rm h}$) of the cluster, i.e.:

$$\mathrm{LSF} \;=\; \frac{M_*(<r_{\rm h})}{M_*(<r_{\rm h})+M_{\rm gas}(<r_{\rm h})} \tag{1.15}$$

since $r_{\rm h}$ evolves with the cluster also does the LSF. In the right panel of Fig. 1.5 the correlation between the LSF measured at the moment of gas expulsion and the bound fraction is shown. It does a better job estimating the bound fractions. Now, however, the trend is not as narrow as in the classical picture. This is a direct consequence of the hierarchical systems used as initial conditions where together with parameter studies a statistical approach becomes necessary.

It was suggested by Smith et al. (2011) that the scatter seen in the $f_{\rm bound}$-LSF trends could partially be explained by the different Q that the cluster have when gas expulsion begins. The initial relaxation have a high impact on Q that oscillate with time and could have values far from $Q = 0.5$ when gas is expelled. It was already argued in analytical terms by Goodwin (2009) that even more important that the SFE is the dynamical state of clusters when gas is expelled. A cold state can considerably increase the survivability of a star cluster. We tested this suggestion performing numerical simulations of the same systems that Smith et al. (2011) evolved, isolating extremes values of pre-gas expulsion virial ratios and analysing how they affect the response of embedded star clusters to gas expulsion. We have published this study in Farias et al. (2015) about the relevance of the pre-gas expulsion virial ratio and we will show the main results of this study on Chapter 4.

Then we will advance the complexity of our models one step forward. We have seen that the only inclusion of substructure have change the outcome of simulations enormously. However there are still several assumptions made on the simulations and we wonder what we have learned in the past years and if the results presented on the first part of this thesis will still hold in a more realistic scenario. The numerical studies performed by Smith et al. (2011) and the one we published in Farias et al. (2015) were done with equal mass particles in order to isolate effects of substructure only. So we don't know what effects an IMF could have in the $f_{\rm bound}$-LSF trend[1], as well as many other physical processes that have not been tested and could be critical, e.g. stellar evolution, multiplicity, tidal fields, feedback from stars, etc. Furthermore, the same observations that motivated the inclusion of stellar substructure on Smith et al. (2011) show that the observed stellar substructure in embedded star clusters is a direct consequence of the filamentary structure present in the gas they were born. It make no sense to keep looking details of the $f_{\rm bound}$-LSF trend if in a realistic scenario with both stellar and gaseous substructure estimations of $f_{\rm bound}$ through the LSF and $Q_{\rm f}$ becomes completely stochastic. In this thesis we will take advantage of the recently developed astrophysical software AMUSE (Portegies Zwart et al., 2013; Pelupessy et al., 2013) to perform simulations of stellar distributions under the presence of dynamically live gas background, that we will describe together with the different codes and numerical methods utilized in the this thesis on Chapter 2 with the introduction to a new method to measure bound mass in substructured systems, called the "Snowballing" method, in Chapter 3. Then we will reproduce the results published on Farias et al. (2015) utilizing a dynamically live Plummer sphere of gas as a background. We will test what are the implications of the interaction of the gas and stars in the embedded evolution of star clusters and their response to gas expulsion in Chapter 5. Then we will test the $f_{\rm bound}$-LSF trend in a more realistic scenario on Chapter 6, recreating the observed primordial substructure of embedded star cluster performing star formation simulations from which we will obtain the initial conditions for later embedded evolution and subsequent gas expulsion. Finally we will summary and discuss the results of this thesis on Chapter 7.

---

[1] A parallel work is now testing this issue, Dominguez et al. in prep.

Chapter 2

Numerical Methods

2.1 Introduction

In our previous work we made very simplistic models of young star clusters, i.e. we follow the evolution of the cluster using a direct integrator and the gas content was mimicked using a static background potential. This basic setup was realistic enough to understand the basics about cluster survival to gas expulsion, we managed to find a relation between the LSF, the final Virial ratio (Q_f) and the fraction of stellar mass that remains bound after gas expulsion (see Farias et al., 2015).

In this work we advance in the complexity of young embedded star clusters. We now follow the evolution of the gas together with the evolution of the stars. This “simple” step involves a huge change in the numerical treatment of the clusters. A simple direct integrator is not enough since stars and gas have ruled by very different physical laws.

The stellar component of the cluster is ruled completely by gravity[1]. Hence a direct integrator is all that we need. The gaseous component on the other hand need to fulfill the hydrodynamics equations described in Section 1.4 and since it is usually the most important mass component of the cluster its self gravity need also to be followed properly.

In the literature we can find two popular ways to follow the evolution of the gas: the Eulerian approach that solves the equations splitting the space into grids (Mellema et al.,

---

[1] There is other processes involving the stars in clusters like stellar evolution, accretion and expulsion of material in protostars, supernovae explosions, etc, that for simplicity we will not consider in this thesis.

1991; Stone and Norman, 1992); and the Lagrangian approach which follow the gas as a set of particles such as Smoothed Particle Hydrodynamics (SPH) (Gingold and Monaghan, 1977; Lucy, 1977). Eulerian methods solve the fluid equations by calculating the flux of information through adjacent cells. SPH techniques calculate the gas properties on each particle by averaging over its nearest neighbours. Usually for star forming and embedded clusters simulations the SPH method is suited better because of huge variations in density that such simulations reach. The SPH method increases the number of particles in regions of high density increasing with that the resolution. A disadvantage is that in low density regions resolution is lost and they cannot not be properly modelled. Still in this work we choose this last method to perform our simulations.

There are several options in the literature that implements the SPH technique to astrophysical processes (Springel et al., 2001; Pelupessy et al., 2004; Springel, 2005; Wetzstein et al., 2009), however most of these implementations either are purely hydrodynamical or implement gravity with some approximation due to the large amount of gas particles necessary to properly resolve the gas. Such implementations may or may not also consider stars as well, but the ones that do consider them use the same approximations to calculate the gravitational forces of the stellar particles. These approximations are usually a Tree code that we will describe in detail in this chapter.

Since we work with highly collisional systems we can not use a Tree code to follow the evolution of the stars. Having that in mind we wish to use a hydrodynamical technique to treat the gas and a direct method to follow the stellar dynamics. For this reason the Astrophysical Multipurpose Software Environment (AMUSE) comes in handy. AMUSE is a PYTHON interface that allows different codes, working in different regimes to communicate with each other. Details of this interface will be discussed later.

Using AMUSE we are able to couple these different codes, however in this work stars and gas will interact just by gravity. We are aware this is not realistic since there are several physical processes that involves stars inserting energy into the surrounding gas like stellar winds, radiative feedback, jets of protostars or supernovae explosions. However in this work we are not interested into recreate all the physics behind star formation and cluster evolution. The goal of this work is to understand the effects of purely gas dynamics on the evolution and survival of the young clusters to gas expulsion, and hence other effects caused by other processes are left for a future work.

2.2 The Astrophysical Multipurpose Software Environment (AMUSE)

AMUSE (Portegies Zwart et al., 2013; Pelupessy et al., 2013) is a high level interface developed in PYTHON that provides a framework allowing the user to couple different systems evolving in different physical domains and scales.

It has implemented several codes that we refer as *community codes* written usually in FORTRAN or C/C++ that can be classified into four physical domains: N-body dynamics, stellar evolution, hydrodynamics and radiative transfer. These community codes can communicate between them using the Message Passing Protocol (MPI) which comes with two main advantages: Codes runs in parallel as two different executables ; Memory allocation is separated for the different codes which is safe.

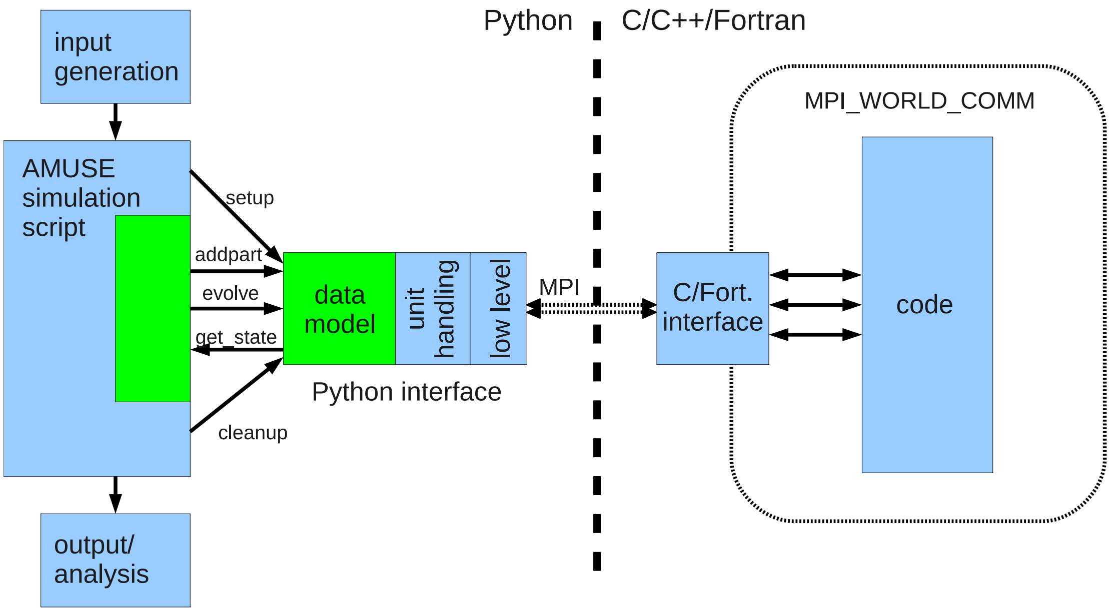

Figure 2.1: Design of the AMUSE interface. This diagram shows how a user PYTHON script interacts with the community code "code". The user only accesses to generics calls ("setup", "evolve", etc) in the high level interface. After handling unit conversions the low level interface communicate through MPI with the native language interface of the code hiding details about code implementations to the user. (Figure taken from Pelupessy et al. 2013)

The fundamental idea of AMUSE is to provide an interface where the user only needs to care about the physical experiment that he wants to explore hiding the complexity and numerical implementation inside the community codes.

Community codes are implemented creating a native language interface. This interface translates functions, variables and methods into messages that communicate through MPI with the PYTHON low level interface of AMUSE in both directions.

On the other hand the user scripts that setup initial conditions, methods, coupling, etc, only interact through generic functions like `evolve_model`, `add_particles`, etc which are translated into the low level interface, after handling units, see Fig. 2.1.

AMUSE enforces the user to use quantities (numbers with a unit) instead of raw numbers. The use of quantities facilitate the catch of errors, the data analysis of the results and an easy interaction with the community codes

2.2.1 The Bridge Integrator

The Bridge integrator (Fujii et al., 2007) is a numerical scheme originally designed to model a star cluster interacting with it parent galaxy. In this models star clusters need high accuracy while the parent galaxy needs a fast scheme because the large amount of particles needed to model it. Fujii et al. (2007) realized that such systems can be splited treating the different systems with their own dedicated method.

The idea behind this scheme is based in the Hamiltonian of the system: Let's consider a system of particles consisting of subsystems A and B, which Hamiltonian is:

$$H = \sum_{i\in A\cup B} \frac{p_{\mathrm{i}}^2}{2m_{\mathrm{i}}} + \sum_{i\neq j\in A\cup B} \frac{Gm_{\mathrm{i}}m_{\mathrm{j}}}{\|r_{\mathrm{i}} - r_{\mathrm{j}}\|} \tag{2.1}$$

such system can be divided into three parts as follows:

$$\begin{aligned} H &= \sum_{i\in A} \frac{p_{\mathrm{i}}^2}{2m_{\mathrm{i}}} + \sum_{i\neq j\in A} \frac{Gm_{\mathrm{i}}m_{\mathrm{j}}}{\|r_{\mathrm{i}} - r_{\mathrm{j}}\|} + \sum_{i\in B} \frac{p_{\mathrm{i}}^2}{2m_{\mathrm{i}}} + \sum_{i\neq j\in B} \frac{Gm_{\mathrm{i}}m_{\mathrm{j}}}{\|r_{\mathrm{i}} - r_{\mathrm{j}}\|} \\ &= + \sum_{i\in A, j\in B} \frac{Gm_{\mathrm{i}}m_{\mathrm{j}}}{\|r_{\mathrm{i}} - r_{\mathrm{j}}\|} \\ &= H_A + H_B + H_{A,B}^{int} \end{aligned} \tag{2.2}$$

with H_A and H_B the Hamiltonians of subsystems A and B respectively and the cross terms are collected in $H_{A,B}^{int}$. Notice that H_A and H_B are independent of each other and $H_{A,B}^{int}$ only depends of the positions, thus the time integration of the interaction consists in purely momentum kicks.

The time evolution of the system is then performed using a Leapfrog scheme: The evolution over a timestep τ consists on mutually kicking the systems A and B i.e. calculating the forces exerted by systems A and B and vice versa and advancing the momenta for a time $\tau/2$. Next the two systems are evolved in isolation (each with a suitable method) for a time τ, after which the timestep is finished by another mutual kick.

This scheme designed for cluster in its parent galaxy can be also applied to any system that interact gravitationally and is possible to split into two (or more). In the case of this work we can replace the host galaxy by a cloud of gas that also needs its own treatment, not only because it follows the laws of hydrodynamics, also because its gravitational forces can not be calculated using a direct integrator, because , like the host galaxy, it needs a huge amount of particles (in the SPH technique) to properly resolve the gas. Thus the Bridge scheme is perfectly applicable to the kind of simulations that we perform in this work.

2.3 The N-body Integrators

In this thesis stellar dynamics is followed usign two different N-body integrators. Simulations in Chapter 4 are performed using the code NBODY6 (Aarseth, 2003) and simulations under the AMUSE framework (Chapters 5 and 6 are performed usint the code Parallel Hermite 4 (PH4) (McMillan in prep.). Both codes have implemented the same basic principles that we will describe in this section.

NBODY6 and PH4 are fourth order Hermite integrators that calculates the forces between the particles directly with no approximations. In general NBODY6 achieves a beter performance than Ph4 because of its several regularizations for small systems (binaries, binaries of binares, close encounters, etc.) but it has not been successfully implemented inside the Amuse framework yet. However, for simulations carried out in this thesis both integrators are equally good since we are not including primordial binaries or extremes scenarios. Both codes work using two basic methods, the *Hermite* scheme and the *Block Timestep* scheme described in this section.

2.3.1 Hermite Scheme

In the Hermite scheme accelerations $\mathbf{a}_0$ amd their derivatives $\dot{\mathbf{a}}_0$ of a particle i are calculated explicitly as:

$$\mathbf{a}_0 = \sum_{\mathrm{j}\neq\mathrm{i}} G m_{\mathrm{j}} \frac{\mathbf{R}_{\mathrm{ij}}}{R_{\mathrm{ij}}^3} \quad ; \quad \dot{\mathbf{a}}_0 = \sum_{\mathrm{j}\neq\mathrm{i}} G m_{\mathrm{j}} \left[\frac{\mathbf{V}_{\mathrm{ij}}}{R_{\mathrm{ij}}^3} - \frac{3(\mathbf{V}_{\mathrm{ij}} \cdot \mathbf{R}_{\mathrm{ij}})\mathbf{R}_{\mathrm{ij}}}{R_{\mathrm{ij}}^5} \right] , \tag{2.3}$$

where G is the gravitational constant, $\mathbf{R}_{\mathrm{ij}} = \mathbf{r}_{\mathrm{i}} - \mathbf{r}_{\mathrm{j}}$, $\mathbf{V}_{\mathrm{ij}} = \mathbf{v}_{\mathrm{i}} - \mathbf{v}_{\mathrm{j}}$, $R_{\mathrm{ij}} = |\mathbf{R}_{\mathrm{ij}}|$, $V_{\mathrm{j}} = |\mathbf{V}_{\mathrm{j}}|$. Then a first (low order) prediction of the position and velocity of the particle i at $t = t_1$ is calculated (with $t_1 = t_0 + \Delta t$ and Δt as particle timestep) according to:

$$\mathbf{x}_p(t) = \frac{1}{6}(t - t_0)^3 \dot{\mathbf{a}}_0 + \frac{1}{2}(t - t_0)^2 \mathbf{a}_0 + (t - t_0)\mathbf{v} + \mathbf{x} \ , \tag{2.4}$$

$$\mathbf{v}_p(t) = \frac{1}{2}(t - t_0)^2 \dot{\mathbf{a}}_0 + (t - t_0)\mathbf{a}_0 + \mathbf{v} \ , \tag{2.5}$$

where the subscript p stands for “predicted”. This is done for all particles in the cluster. Thus, using again 2.3 with the new positions of the particles we obtain the accelerations and its derivatives at $t = t_1$ denoted $\mathbf{a}_1$ and $\dot{\mathbf{a}}_1$. However $\mathbf{a}_1$ and $\dot{\mathbf{a}}_1$ can also be obtained using Taylor series with higher derivatives of $\mathbf{a}$ at $t = t_0$:

$$\mathbf{a}_1 = \frac{1}{6}(t - t_0)^3 \mathbf{a}_0^{(3)} + \frac{1}{2}(t - t_0)^2 \mathbf{a}_0^{(2)} + (t - t_0)\dot{\mathbf{a}}_0 + \mathbf{a_0} \ , \tag{2.6}$$

$$\dot{\mathbf{a}}_1 = \frac{1}{2}(t - t_0)^2 \mathbf{a}_0^{(3)} + (t - t_0)\mathbf{a}_0^{(2)} + \dot{\mathbf{a}}_0 \ . \tag{2.7}$$

Now, since we already know $\mathbf{a}_1$ and $\dot{\mathbf{a}}_1$ from the low order prediction, we can use that result to obtain the higher derivatives of $\mathbf{a}$, at $t = t_0$, i.e. $\mathbf{a}^{(2)}$ and $\mathbf{a}^{(3)}$:

$$\frac{1}{2}\mathbf{a}^{(2)} = -3\frac{\mathbf{a}_0 - \mathbf{a}_1}{(t - t_0)^2} - \frac{2\dot{\mathbf{a}}_0 + \dot{\mathbf{a}}_1}{(t - t_0)} \tag{2.8}$$

$$\frac{1}{6}\mathbf{a}^{(3)} = 2\frac{\mathbf{a}_0 - \mathbf{a}_1}{(t - t_0)^3} - \frac{\dot{\mathbf{a}}_0 + \dot{\mathbf{a}}_1}{(t - t_0)^2} \ , \tag{2.9}$$

The Hermite interpolation then finishes the timestep correcting the low order prediction of the positions and velocities to a higher order:

$$\mathbf{x}(t) = \mathbf{x}_p(t) + \frac{1}{24}(t-t_0)^4\mathbf{a}_0^{(2)} + \frac{1}{120}(t-t_0)^5\mathbf{a}^{(3)} \;, \tag{2.10}$$

$$\mathbf{v}(t) = \mathbf{v}_p(t) + \frac{1}{6}(t-t_0)^3\mathbf{a}_0^{(2)} + \frac{1}{24}(t-t_0)^4\mathbf{a}_0^{(3)} \;. \tag{2.11}$$

2.3.2 Block Timestep Scheme

Ph4 also has individual timesteps for particles in a scheme called *Block Timestep*. In this scheme particles timesteps are sorted into a hierarchy levels starting from a maximum timestep Δt_1 according to the rule:

$$\Delta t_n = \Delta t_1 / 2^{n-1} \tag{2.12}$$

At the beginning of the calculation a reasonable timestep for each particle is specified. This reasonable timestep has been found by empirical experiments to be (see Aarseth, 2003):

$$\Delta t_{\mathrm{i}} = \sqrt{\frac{\eta |\mathbf{a}||\mathbf{a}^{(2)}| + |\dot{\mathbf{a}}|^2}{|\dot{\mathbf{a}}||\mathbf{a}^{(3)}| + |\mathbf{a}^{(2)}|^2}} \tag{2.13}$$

where η is a free parameter, by experience is usually is taken to be $\eta = 0.01 - 0.04$. Then the nearest level is chosen according to 2.12. At any general time Eq. 2.12 is evaluated and any of this three cases apply when comparing with the previous timestep Δt_p: If $\Delta t_p > \Delta t_{\mathrm{i}}$ then the timestep is reduced by factor 2; if $2\Delta t_p < \Delta t_{\mathrm{i}}$ the timestep is increased by factor 2 ; otherwise there is no change. A detailed discussion about the implementation and special situations can be found in Aarseth (2003).

2.4 The Hybrid Tree/SPH Code Fi

The gas in the cluster is modeled using the code Fi (Hernquist and Katz, 1989; Gerritsen and Icke, 1997; Pelupessy et al., 2004; Pelupessy, 2005) which treats the gas using the SPH technique (Monaghan, 1992) to solve the hydrodynamical equations. Fi also solves self gravity of the gas using a Tree algorithm developed by Barnes and Hut (1986). In this section we will quickly describe the fundamentals of the two implemented methods where further details can be found in the respective literature.

2.4.1 Barnes-Hut Tree-Code

The main force that keeps the cluster together is gravity. This force does not only affect the stellar component, it affects every component that has mass. The gaseous component of the cluster usually contains the most important fraction of the total mass in a cluster. Thus a consistent method to treat the gravity of the gas is imperative. Since the gas is modeled using finite particles it would be possible to use the Hermite integrator to calculate the accelerations, however a typical SPH simulations uses from thousands to millions of particles to properly model the gas. Thus a direct N-body integrator which needs $\mathcal{O}(N^2)$ operations per force calculation is not viable. Barnes and Hut (1986)

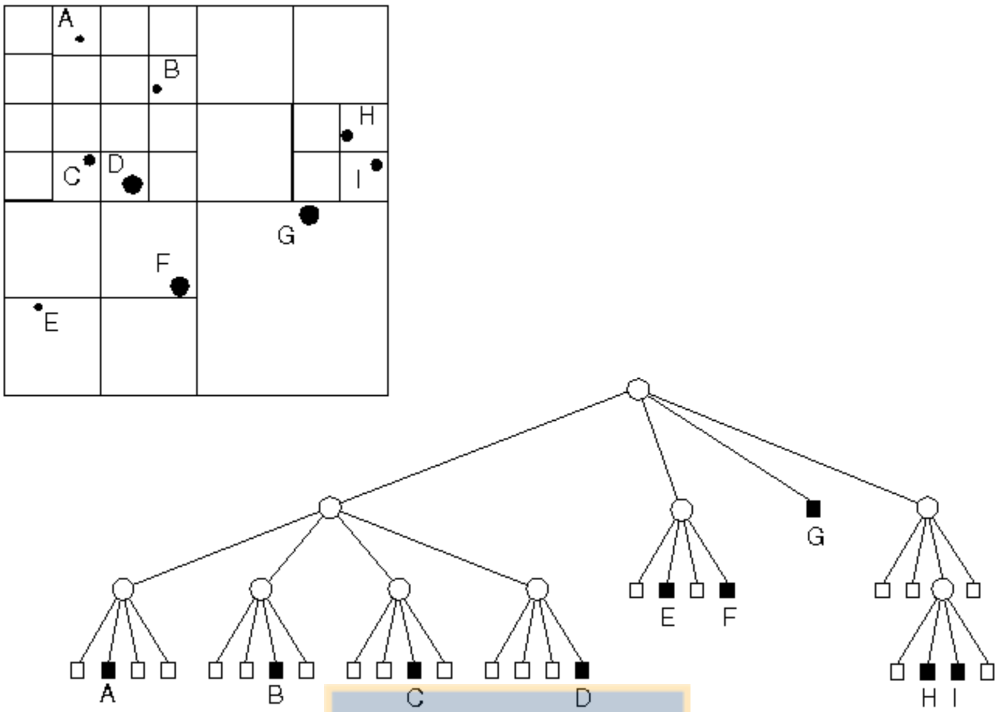

Figure 2.2: A 2D example of the construction of the hierarchical tree.

developed an algorithm that sacrifices accuracy to gain speed. The basic idea behind this method is that particles that are far away are approximated using their center of mass to get the acceleration. And accelerations by particles nearby are calculated using a direct summation.

To decide which particles are far enough to make this approximation, the particles are sorted into an octree i.e. the space is divided consecutively into eight zones called the parent nodes. If a node contains more that one particle then it is divided consecutively into eight children nodes until each children node contains only one particle. Nodes with no particles are dropped.

Thus a tree like hierarchy is constructed (hence the name). All nodes have a size l, a center of mass, and a total mass inside the node, see Fig.2.2 for a 2D example of the algorithm. The force evaluation is done by recursively opening the nodes in the tree, where a comparison of the size of the node and the distance d to the center of mass of the node:

$$\frac{l}{d} > \theta \tag{2.14}$$

where θ is a critical value that controls the accuracy of the calculated gravitational forces. In nodes that this criterion pass, forces are calculated using the center of mass of the node, if not the node is opened and Eq. 2.14 is evaluated in the children nodes recursively.

The Barnes-Hut tree method as been widely used in numerical N-Body simulations due to its $\mathcal{O}(N \log N)$ operations per force calculation and that can bee applied efficiently to any mass distribution. It has been shown by Springel et al. (2001) that the criterion 2.14 could fail and lead to large fractional when the particles are exposed to large cancelling forces from the rest of the system. In Fi an alternative criterion is implemented, suggested by Springel et al. (2001) :

$$Ml^4 > \alpha|\mathbf{a}|d^6 \tag{2.15}$$

where M is the total mass contained in the node, $\mathbf{a}$ is an estimate of the acceleration, in practice this is the acceleration of the last time step, and α the parameter controlling the accuracy of the force calculation. Pelupessy (2005) claims that after a comparison Eq. 2.15 actually gives smaller fractional force errors in the central part of galaxy simulations.

2.4.2 Smoothed Particle Hydrodynamics

Smoothed Particle Hydrodynamics (Gingold and Monaghan, 1977; Lucy, 1977; Monaghan, 1992) is a particle based method for gas hydrodynamics. It represents a continuous fluid by a set of finite smoothed particles whose densities are estimated from the surrounded neighbours using a kernel function $W(r, h)$. Thus, for a set of particles with masses m_i and smoothing lengths h_i we have

$$\rho_\mathrm{i} = \sum_{i \neq j} m_\mathrm{j} W(|\mathbf{r}_\mathrm{i} - \mathbf{r}_\mathrm{j}|, h_\mathrm{i}), \tag{2.16}$$

for the density ρ_i at particle positions $\mathbf{r}_\mathrm{i}$. Fi uses a spline kernel function as follows:

$$W(r,h) = \frac{1}{\pi h^3} \begin{cases} 1 - \frac{3}{2}\left(\frac{r}{h}\right)^2 + \frac{3}{4}\left(\frac{r}{h}\right) & 0 \leq r \leq h \\ \frac{1}{4}(2 - \frac{r}{h})^3 & h \leq r \leq 2h \\ 0 & \text{otherwise} \end{cases} \tag{2.17}$$

In the SPH scheme the equations of motion for the particles are derived from Eq. 2.16 starting from the discretized Lagrangian for a compressible non dissipative flow, with adiabatic index γ (see Rasio and Lombardi, 1999, for a complete derivation of the scheme):

$$L = \sum_\mathrm{i} m_\mathrm{i} \left(\frac{1}{2} v_\mathrm{i}^2 + \frac{1}{\gamma - 1} A_\mathrm{i} \rho^{\gamma - 1} \right), \tag{2.18}$$

where m_i is the mass of each particle, v_i the velocity, A_i is the entropic function which is defined through the pressure as $P_\mathrm{i} = A_\mathrm{i} \rho^\gamma$. For an adiabatic gas the internal energy u_i is obtained from the entropic function as:

$$u_\mathrm{i} = \frac{A_\mathrm{i}}{\gamma - 1} \rho^{\gamma - 1} \tag{2.19}$$

Usually the smoothing length h_i is chosen in order to maintain the number of neighbours inside a smoothing length (more or less) constant. However in Fi this is not done in order to avoid the inclusion of errors due to the variability of h_i. Instead they take h_i as a dynamic variable introducing constraints that determines the variable. In that way they take care of the extra ∇h introducing it implicitly into the equations of motion. Those constraints lead to a definition of h_i as follows:

$$h_\mathrm{i}^3 = \frac{3}{4\pi} \frac{N_\mathrm{nb} \bar{m}}{(\rho_\mathrm{i} + \tilde{\rho})}, \tag{2.20}$$

where $N_{\rm nb}$ is the number of neighbours that is usually between 50 and 60 particles, $\bar{m}$ is the mean mass of the particles, and $\tilde{\rho}$ is a limit density thats avoid a too large value of $h_{\rm i}$ when the density is too small.

2.5 Measuring bound fraction

In order to measure the bound mass that survives gas expulsion we developed a new method that becomes specially useful in the clumpy scenario that we are working on. The method uses the following bound criterion: *Stars that are not bound do not contribute to the potential of the cluster.* Is an iterative method that starts with a cluster core (chosen by some radius) and then starts to grow up trapping the stars that are bound to this core and adding their masses and positions to the potential of this core. This process is repeated until there are no more changes, obtaining the total bound mass of the cluster. The method, that we call *Smowballing*, will be described and discussed in detail in the following chapter.

Chapter 3

Measuring Bound Fraction: The Snowballing Method

3.1 Introduction

The bound mass of a system is an important quantity as it controls their gravity, but is usually not an easy quantity to measure. On simple systems like isolated clusters it is easy to calculate. But when we are facing a “real life” scenario this is not an easy task.

In this study we feel the need of developing some reliable method to measure the bound mass of a cluster. This comes from the need to distinguish between bound stars and unbound stars since in our simulations, after gas expulsion, a cluster is not always alone. Usually a surviving cluster is surrounded by one or more clumps. It is difficult to say if a star is bound to the specific cluster that we are focusing on, or it is bound to the whole system with all the clumps in it.

With that motivation, we developed a simple and reliable method to measure bound masses, we call it *The Snowballing Method* (SBM). An important reason that we believe that the SBM is quite reliable, is the measurement of the velocity of the system. In an scenario where there is a lot of unbound particles mixed with the bound system a simple measurement of the average velocity will give us a wrong estimation of the velocity of the system. To know the velocity of the system we need to measure the average velocity of the bound mass, but to calculate the bound mass we already need the velocity of the system, so it is a circular problem. The SBM deals with this problem starting with a bound core and fixing the average velocity at the same time that the system is growing.

In this chapter we expose the method and its limitations. We also discuss its possible applications to another physical problems that need to differentiate bound mass from unbound mass.

3.2 The method

3.2.1 Description

The SBM is based on a simple criterion, *unbound particles don't contribute to the potential of the cluster*. We make this approximation because unbound particles will not be in or around the cluster long enough to change the cluster potential. Therefore, adding those particles to the cluster potential will overestimate its strength and at the same time will overestimate the number of cluster members.

In order to determine the true members of the cluster we start with a core radius R_c, were every particle inside of R_c is considered bound at the beginning. Let's call N_in number of particles inside R_c. A study of this choice is discussed later in the next section. After this choice we can separate the following in two iterative steps: The elimination step and the snowballing step. The objective of the elimination step is to determine a true bound core before getting into the snowballing step. The particles we leave behind may be bound or not to the final cluster, but that decision is a task for the snowballing step.

In the *elimination step* we check that every particle inside R_c is bound to the $N_\mathrm{in} - 1$ particles remaining. The average velocity of the $N_\mathrm{in} - 1$ is calculated in order to be subtracted from the cluster, then we decide if this particle is bound or not to the others using the bound condition:

$$KE \leq PE \tag{3.1}$$

with KE and PE the kinetic and potential energy respectively. Every particle unbound is then excluded, and then we repeat the process until we get no more changes.

This bound core is the starting point of the *snowballing step*. It starts calculating the average velocity of the cluster $\bar{V}_\mathrm{c}$ of the core to been temporally subtracted from the system. Then every particle in the system under Eq. 3.1 is now added to the cluster potential. Notice that at the end of this step the potential could be very different to the one before, so it is necessary to redo this step over and over until we get no more changes in the number of members or, in the worst case, until we get a difference below a certain tolerance, and the method can be stopped.

Notice that the average velocity has to be calculated in every iteration, because every particle that we include will change it and it is possible that because of a wrong estimation of the velocity of the cluster we are getting particles bound that in reality are not. That's an important reason of why the elimination step is needed, any extra unbound particle inside R_c will not affect just the main potential making us overestimate it, the other reason, and perhaps more important, is that these unbound particles will have a great velocity considerably affecting the average velocity even more than the bound ones.

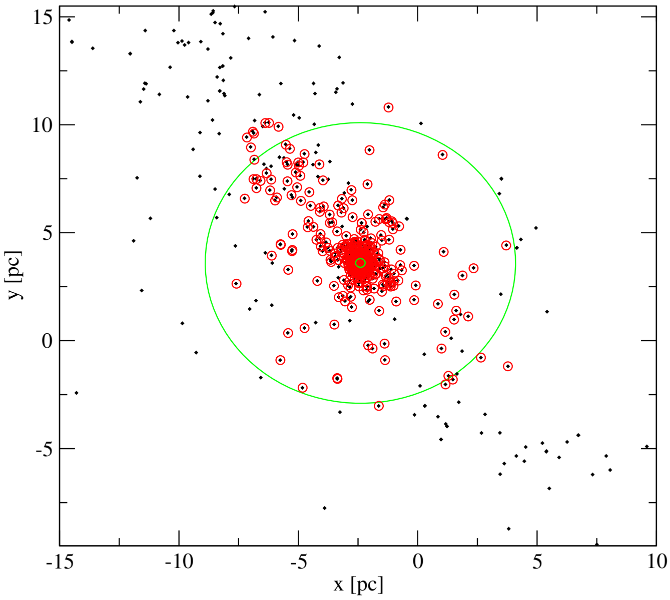

Figure 3.1: An x-y projection of a infant mortality surviver. Dots marked with red circles show the bound stars, green circles show the range which R_c can be selected to get the same answer. This area varies case by case, but the usual best choice, to get an accurate answer, is a small R_c just above getting zero particles bound.

Therefore, there are three important things that change after every iteration: The potential of the cluster, the average velocity and the bound mass.

3.2.2 The election of R_c and convergence

The initial core radius R_c is the only parameter that has to be chosen *by eye*. There are better choices for this but in general the elimination step is responsible in improving our choice. In general if we take an excessive short R_c we don't get enough particles to create a bound core, on the other hand if we take an excessive large R_c the elimination step will try to eliminate unbound particles but it is possible that there is a large number of unbound particles inside the initial sphere and the excessive potential added will make the method believe that these particles are all bound.

The limits of the smallest and biggest R_c that we can choose and obtain the same answer is shown in Fig. 3.1. Using one of our gas expulsion simulations (see 4) we test the limits of this initial choice. These limits vary depending on the velocities and spatial distributions, but in general this is a good example. We also made a simple test to study the convergence of the method. To a Plummer distribution of 1000 particles with a cutoff radius of 10 pc, we add an extra particle on the edge with a velocity just above the escape velocity, Figure 3.2 shows the results of taking different R_c.

As we can see we have a large range of safety and it is possible make a decision by eye without making mistakes. If we are working with a large number of particles this election will be very important to get as less iterations as possible and save time, the best choice in that case is just matter of experience, but in general a good decision could be to take a large number of particles but not more or too close to the final answer i. e. checking if the code uses the snowballing step at least once. If we just get the elimination step we should decrease R_c. If we don't care about the number of iterations and we want to apply the method to a large number of distributions, we should get a medium R_c that enclose the mayor concentration of particles.

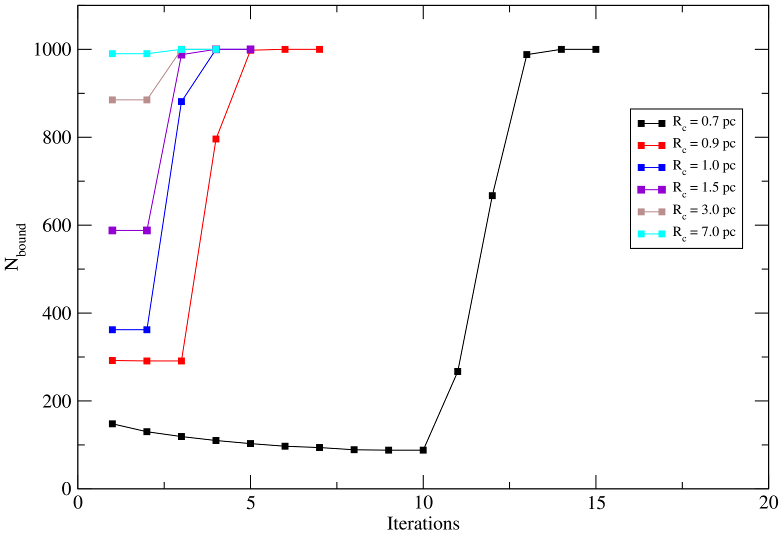

Figure 3.2: Convergence test of the Snowballing method when using different initial core radius. We take different R_c for a sample of 1000 bound particles on a Plummer distribution and the consequences on the number of iterations.

3.3 Working on a Clumpy Scenario

3.3.1 External Clusters and Potentials.

Some times we could have more than one clump or cluster near to the one that we are studying, if we just apply the SBM as we describe it, we could get some strange answers. The problem is that if we have two cluster near to each other there is two possibilities: they are bound to each other or they are not. If they are bound it will be no problem and the SBM will take everything and we will get all stars belonging to both clusters as output plus the stars that are gravitationally bound to this system. But if the external cluster is not bound and has a relative velocity just over the escape velocity the SBM will still give us the whole system as one. The reason of this is because the method just sees the velocities and his own potential but don't consider the potential of the external cluster. This external potential will make the bound potential weaker and the escape speed will be lower. So we are again overestimating the main potential because there is a group of stars bound to the external cluster and not to the one that we are studding.

There are two ways to correct this problem: The simple one is to make a number of star vs radius plot of the cluster, if we make this we can clearly see at which radius the external cluster is adding to the number of bound particles, and we can arbitrary cut off the number of members at this radius. That estimation could be seen as a simplistic way to do it but the error of doing that will be not that much compared with trusting on the method blindly in this particular case. A better way to do it is to consider this external potential on the method, a way to do that is taking the elimination step for this external cluster and save this potential, then for a single particle we can compare both and decide if this particle is bound to the external cluster or not. Details of this technique are explained in Sec. 3.3.2.

Furthermore the SBM, as we have described it, does not consider external potentials that could affect the bound particles, the method only show if a system of particles is gravitationally bound or not under the potential of its members. An external potential like a near galaxy that is dissolving our cluster could be considered, but the question is, what do we want to know. If we want to see how a galaxy destroys an orbiting star cluster we probably want to know which stars are bound under his own potential. Giving

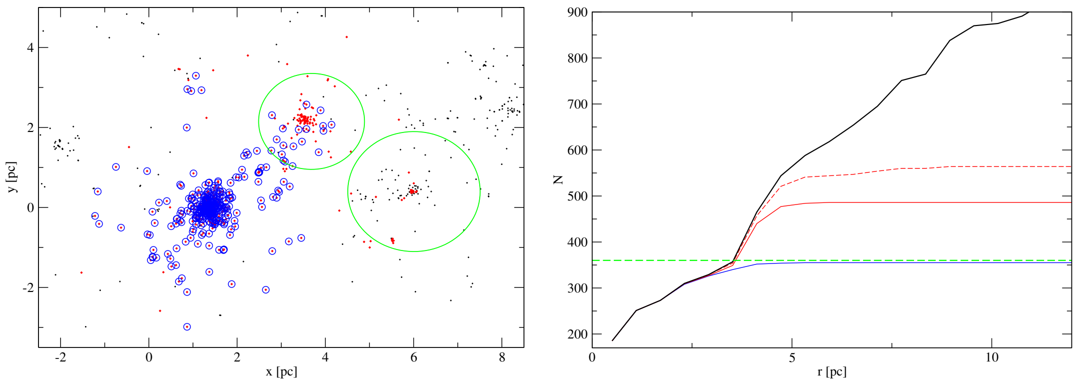

Figure 3.3: A comparisson between the Snowballing method and the enhanced Snowballing method applied to an infant mortality surviver. **Left**: An x-y projection of a infant mortality surviver. We see two small clusters near to the one that we are studying, an enhanced SBM is applied and we can see the difference between the SBM with and without the improvement. Red dots are stars bound with the standard SBM, and blue circles marks stars bound using the enhanced SBM. Green circles show the clusters considered and the $R_{\rm c}$ used to apply the elimination step for saving the potential of each cluster. **Right**: Radius plot of the two methods mentioned. We show the total of stars inside a certain radius $N_{\rm total}$ (black line), the simple SBM (red line), the SM (red dashed line), the enhanced SBM (blue line), and a *by eye* cut off that is possible to do without having a considerable scatter (green dashed line).

the external potential too much importance is the same than trying to know the answer before using a simulation to see the future evolution, external potentials could be useful and the method is compatible with that, but again we have to be careful in what do we want to know.

The important thing is that we present a method that tells us a reliable answer for the number of instantaneous bound particles, if we want to know what will happen in the future, we must make a simulation.

3.3.2 The Snowballing Method Enhanced

To deal with external clusters and, if we want, external potentials we modify the SBM and create the enhanced SBM. In the present section we describe the considerations, details and problems that appear when we consider an external potential.

We start the method choosing different $R_{\rm c}$ and applying the elimination step to every external cluster and saving its members, then we apply the elimination step to the cluster that we are studying, let's call it the main cluster. Now the snowballing step begins with a couple of modifications:

We start making the external potential $PE_{\rm e}$, but every particle that belong to the main cluster, at the beginning just a core, is included in the main potential $PE_{\rm c}$ but not included in $PE_{\rm e}$, having that in mind the bound condition (3.1) changes to:

$$PE = PE_{\rm e} + PE_{\rm c} \leq 0 \quad \wedge \quad KE \leq |PE| \tag{3.2}$$

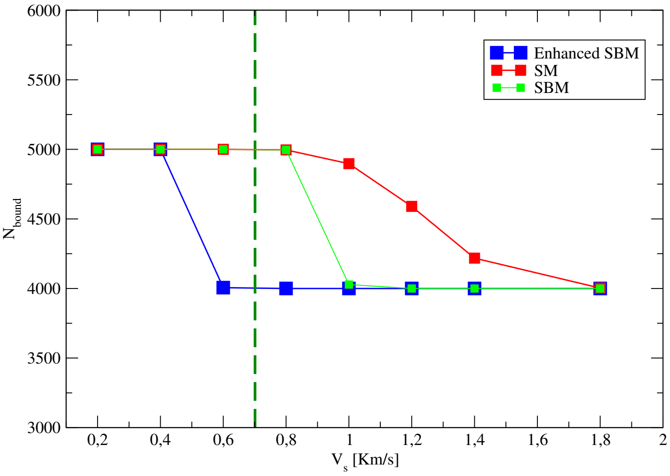

Figure 3.4: A test showing how the Snowballing method and the enhanced Snowballing method can distinguish between two near Plummer spheres with a varying relative velocity. We add different velocities to a small Plummer sphere distribution ($N = 1000$) next to a big Plummer sphere distribution ($N = 4000$), dark green dashed line shows the V_{esc} of the small sphere. We can see how sensitive are the three methods to an external cluster, the SBM and SM need a great velocity to distinguish both clusters, on the other hand the enhanced SBM can distinguish both clusters just before there are unbound.

Notice that PE_{c} is a bound energy so is negative, but PE_{e} is an unbind energy so it must be positive, thats why if the addition of both is positive that means that our particle is unbound. But if $PE_{\text{e}} + PE_{\text{c}}$ is negative we need to compare with the kinetic energy.

Is important to notice that the last method is still just an estimation, because the elimination step by itself is not a good method to calculate bound fraction, so we don't know the real potential of near clusters.

3.3.3 A Simple Test: Two Plummer Spheres

In order to test the exact behavior of both the SBM and the enhanced SBM to an external near cluster, we perform a simple test using two virialised Plummer distribution right next to each other. We use a big Plummer distribution as the main cluster and a small Plummer distribution as an external cluster.

The big Plummer sphere has 4000 particles a cut off radius of 20 pc and a Plummer radius $R_{\text{pl}} = 15$ pc. The small one has 1000 particles a cut off radius of 10 pc and $R_{\text{pl}} = 15$ pc. The center of the spheres are separated a distance of 35 pc in that way they don't touch each other and we can treat them like two single particles in order to easily know the escape velocity V_{esc} . Both Plummer spheres have no starting velocity, i.e. they have no relative velocity. We test this system increasing the radial velocity between the spheres V_{s} i. e. adding the velocity V_{s} to all the particles of the small Plummer sphere. Then we measure the number of particles bound to the big Plummer sphere. In that way we should obtain all the particles of both spheres bound when $V_{\text{s}} < V_{\text{esc}}$ and just the particles of the big sphere as bound when $V_{\text{s}} > V_{\text{esc}}$. We can see the results in Fig. 3.4

We can clearly see that the SBM is less sensitive than the SM but still gives us a wrong answer. When the small sphere exceeds the escape velocity we should get just the big Plummer sphere's particles as bound, but we are don't. On the other hand the enhanced SBM distinguishes both cluster too soon, so the SBM and the enhanced SBM can't tell us accurately if both clusters are bound or not, they just give us an estimation. But note that if we get two bound clusters with the enhanced SBM there is a big probability that both cluster are really bound. On the other hand if the SBM tells us that a near cluster is not bound, there is a big chance that it is true.

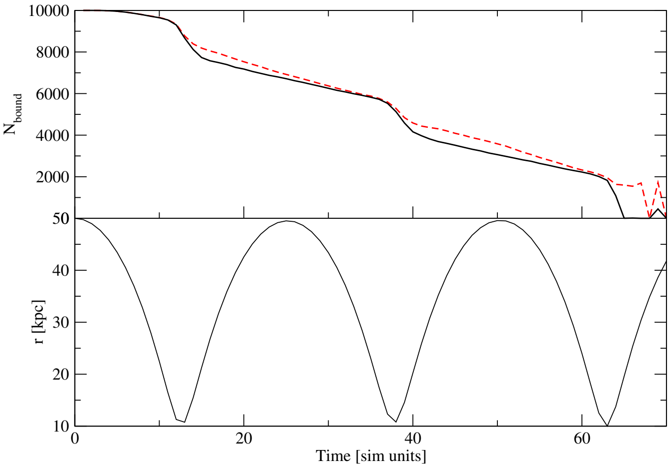

Figure 3.5: A Plummer sphere distribution ($N = 10000$) that is orbiting a galaxy potential. Top graph shows the number of cluster members, calculated with the SM (red dashed line) and with the SBM (black line), vs time. Bottom shows the distance from the cluster to the center of the galaxy potential. We can see how the galaxy destroys the cluster and the difference between the two methods becomes bigger when the cluster just left its pericentre, at that point the mixture of unbound and bound particles becomes biggest.

3.4 Recognizing Bound Members: An Orbiting Cluster

Another problem in which the SBM could be very useful is an orbiting cluster that's been destroyed by a galaxy. There are some problems where the SM and also a structure code like the minimum spanning tree (MST) could fail; e. g. knowing the real members of the cluster at any time. The main reason is that if a cluster gets destroyed it is also *stretched* and it develops tidal tails. When the cluster is at its pericentre its tails get mixed with the cluster itself. In that particular stage a SM confuses unbound particles with particles that are just passing the cluster. The average velocity and the real cluster members become difficult to calculate because this mixture of stars and velocities. But here the SBM becomes useful, because the SBM ignores the stars with a large velocity and can differentiate the cluster even at pericentre.

We make a simple test to check if this is actually true. We set a Plummer sphere of $N = 10000$ particles orbiting a galaxy at initially 50 Kpc from the galactic center. It initial radial velocity is 220 km/s with an pericentre and apocentre of 10 and 50 kpc respectively. We can see the difference between the SM and the SBM measuring the members in Fig. 3.5. The difference between both methods become bigger after the pericentre. At that point the mixture of unbound and bound particles becomes extreme. However, the SBM ignore these particles giving an more accurate answer. At the end of the simulation the SM shows some noise because the cluster get completely destroyed. The SBM can tell exactly when the cluster gets destroyed with no extra noise.

In summary, in this kind of scenario with a high mixture of bound a unbound particles the SBM becomes very useful in order to recognize the cluster members at any instant of the cluster evolution.

3.5 Conclusion

We have introduced a simple method to measure the bound mass. The method become very useful in clumpy scenarios and in systems where bound particles are highly mixed with unbound particles, like near field tidal tails. The method needs a reliable measure of individual velocities and masses that are not available observationally. However, in theoretical simulations the standard criterion sometimes is not enough and this method proves to be reliable and fast in different kind of scenarios. It is possible to extend the method to others kind of particles like gas particles on an SPH simulation just adding the corresponding bound criterion to the particles, however this method has not been tested with SPH particles yet. At least we have a reliable method that can distinguish a self consistent bound system at any time in clumpy scenarios, affected or not by external forces.

Chapter 4

The Relevance of the Pre-Gas Expulsion Virial Ratio

Abstract

We examine the effects of gas-expulsion on initially substructured distributions of stars. We perform N-body simulations of the evolution of these distributions in a static background potential to mimic the gas. We remove the static potential instantaneously to model gas-expulsion. We find that the exact dynamical state of the cluster plays a very strong role in affecting a cluster's survival, especially at early times: they may be entirely destroyed or only weakly affected. We show that knowing both detailed dynamics and relative star-gas distributions can provide a good estimate of the post-gas expulsion state of the cluster, but even knowing these is not an absolute way of determining the survival or otherwise of the cluster.

4.1 Introduction

In this is Chapter we show the continuation of the work done by Smith et al. (2011) and Smith et al. (2013) on the response of complex, hierarchical systems to gas expulsion. We have published this work in Farias et al. (2015). First we will summarize findings of Smith et al. (2011) and Smith et al. (2013) on Sec. 4.2, explain our initial conditions and motivation on Sec. 4.3, present our results in Sec: 4.4 to finally discuss our findings in Sec. 4.5.

4.2 Previous Studies

Numerical models of gas expulsion from initially virialised gas-star Plummer spheres have shown that a small fraction of stars can remain bound if the stars make-up more than about 30 per cent of the initial system (in this case what is often assumed to be a direct measure of the star formation efficiency), and the majority of the stars will remain bound if the fraction is greater than 50 per cent (see e.g. Goodwin and Bastian 2006; Baumgardt and Kroupa 2007). The speed of gas expulsion is important with fast (instantaneous) gas expulsion being significantly more disruptive than slow (adiabatic) gas expulsion (see Baumgardt and Kroupa 2007 and Lada et al. 1984).

Initial conditions of Smith et al. (2011), Smith et al. (2013) and the ones we will use here, are highly simplified, but hopefully realistic at a fundamental level, model of a fractal stellar distribution relaxing in a global gas potential before the removal of that gas potential. This is very different from the initially star-gas equilibrium distributions assumed in the classical picture.

Because the stellar distribution is highly out-of-equilibrium and also different from the gas potential, this means that the stellar distribution will violently relax. The initial fractal substructures will be erased and the stellar distribution will become smooth, whilst at the same time relaxing to fit the underlying static (gas) potential (see also Allison et al. 2009; Parker et al. 2014). This means that the stellar distribution will become more concentrated relative to the static gas potential as potential energy stored in substructure is distributed more smoothly (see e.g. Allison et al. 2009).

Smith et al. (2011) identify an important parameter in determining the remaining bound fraction as the local stellar fraction (LSF). The LSF is a measure of the gas mass within the *stellar* half-mass radius; i.e. a measure of the relative importance of the gas to the stars. The LSF is defined inside the half mass radius $r_{\rm h}$ of the stellar component.

The LSF is analogous to the star formation efficiency (SFE) quoted in many previous studies (although as noted by Verschueren and David (1989) and Goodwin (2009) this should really be called the effective SFE as its relationship to the true SFE is uncertain). Smith et al. (2011) show that the LSF will depend on the initial distribution of stars, the initial gas-to-star mass, and the initial energy of the stellar distribution (also see Kruijssen, 2012; Parmentier and Pfalzner, 2013; Parmentier, 2014).

Smith et al. (2011) find that there is a reasonably good relationship between the final bound fraction and the LSF at the point of gas expulsion for systems which have relaxed for more than two initial crossing times. However, Smith et al. (2013) show that if gas expulsion occurs earlier, it is rather more complex than this suggests.

The longer the stars have to relax, the closer to a virialised, smooth distribution in equilibrium with the static gas potential they will become. Smith et al. (2013) show two important consequences of this relaxation processes. Firstly, the LSF changes with time and so the exact time of gas expulsion is very important. Secondly, the violent relaxation of the initially clumpy stellar distributions is stochastic and initial distributions that are initially 'the same' (i.e. drawn from the same generating functions) can evolve very differently, and at any particular point in time (i.e. at gas expulsion) can have quite different dynamics and be at different 'stages' in their relaxation. If gas expulsion occurs at early times (typically less than one crossing time, or around 1 Myr) then the LSF ceases to be a good predictor of the final bound fraction.

Smith et al. (2013) attempted to quantify these effects and found that the virial ratio of the stars at the time of gas expulsion is *also* very important to the final bound fraction (as suggested by Goodwin 2009). In this study we concentrate on examining the effects of the stellar virial ratio at the time of gas expulsion.

4.3 Simulations

Since we wish to continue the work of Smith et al. (2011, 2013), we use similar, simplified initial conditions for our simulations. We perform N-body simulations using the Nbody6 code (Aarseth, 2003).

As we describe in more detail below, equal-mass stars are distributed in a fractal distribution in a smooth and static background potential to mimic the potential of the gas in which they are embedded. Given that we use a static potential for the gas, we are unable to include active star formation in our models. However we do not expect this to change the key conclusions of this study. The potential is then removed instantaneously to simulate gas-expulsion.

This is clearly an extreme over-simplification in many ways. In reality, the gas is not distributed in a smooth spherical distribution, and both the gas and stars will move in response to changes in the global potential. The gas will also react to hydrodynamic forces and feedback (which is what eventually expel any remaining gas). Gas expulsion is unlikely to be instantaneous, rather gas will be lost at different rates in different regions, and dynamics can cause the stars and gas to decouple without any feedback.

We take this simplified approach rather than attempt to deal with the gas dynamics with a hydrodynamic method for two reasons. Firstly, the practical issue of performing large ensembles of simulations – this is much quicker and easier with pure N-body simulations. Secondly, the complexity of the gas distribution would add large numbers of (largely unknown) parameters to our possible parameter space. We will return to discuss this issue later.

We choose equal mass particles in order to avoid complex two body interactions and mass segregation (see e.g. Allison et al. 2009 for the complications a realistic mass spectrum can add to an already complex problem). This will be addressed in more detail in a future work (Dominguez et al., in prep.).

4.3.1 Initial Distributions

In all cases we model the stellar distribution using $N = 1000$ particles with equal masses of 0.5 $M_\odot$.

Using the box fractal method described by Goodwin and Whitworth (2004), we create 20 random realisations of fractal distributions, each with a fractal dimensions of $D = 1.6$, corresponding to a highly clumpy initial distribution within a radius of 1.5 pc. We use the same 20 stellar distributions for each background potential.

We start our simulations with two energies: initial virial ratios of $Q_{\rm i} = 0.5$ (warm), and $Q_{\rm i} = 0$ (cold). As we will show, even our $Q_{\rm i=0.5}$ simulations are not in equilibrium. Fractal clusters will then attempt to relax in persuit of equilibrium and subsequently there are large variations in their virial ratio parameter. Thus, we measure Q instantaneously at two important epochs: the beginning of the simulation ($Q_{\rm i}$ where 'i' donates 'initial'), and the moment when gas expulsion begins ($Q_{\rm f}$ where 'f' donates 'final'). The cold systems start with the stars initially at rest relative to each-other, this is unrealistic, but is the case where we expect the most rapid collapse and erasure of substructure.

4.3.2 The Background Potential and SFE

We work with three different static background potentials: (i) a Plummer sphere with $R_{\rm pl} = 1.0$ pc and $M_{\rm gas,tot} = 3472$ M$_\odot$, (ii) a uniform sphere of gas with a maximum radius of $R = 1.8$ pc and $M_{\rm gas,tot} = 3455$ M$_\odot$ (equivalent to a Plummer sphere with $R_{\rm pl} = \infty$), and finally (iii) a highly concentrated Plummer sphere with $R_{\rm pl} = 0.2$ and $M_{\rm gas,tot} = 2053$ M$_\odot$. This choice of parameters ensures that we obtain a SFE = 0.2 for all three background potentials (i.e. we always have exactly 2500 M$_\odot$ total mass within 1.5 pc, of which 2000 M$_\odot$ is gas, and 500 M$_\odot$ is stars).

In this work we expel the gas instantaneously at early times in the evolution of the cluster i.e. within a few crossing times ($1t_{\rm cr} \approx 1.4$ Myr), and compare to clusters with a later gas expulsion ($\sim 7.5t_{\rm cr}$).

4.3.3 Gas Expulsion Time

We simulate rapid gas expulsion by removing the background potential instantaneously. This is the most potentially destructive gas expulsion (see Baumgardt and Kroupa 2007).

As we wish to model the effects of early gas expulsion, we usually remove the gas potential instantaneously within two *initial* crossing times ($1t_{\rm cr} \approx 1.4$ Myr). During this time, the initial distributions relax violently and $t_{\rm cr}$ may no longer be a representative timescale (see section 4.3.4)

We first summarise the results from our previous studies before describing and explaining our new results.

4.3.4 Motivation

In this Chapter we extend the work of Smith et al. (2011, 2013). We have two related questions that we wish to consider.

Firstly, to what extent is it possible to predict the final bound fraction of the system? Secondly, is it ever practically possible (either observationally or theoretically) to predict the final bound fraction of a particular system?

In this Chapter we concentrate mainly on the effects of the dynamical state of the stars at the time of gas expulsion (as measured by the stellar virial ratio).

We concentrate on systems which have not had many crossing times to relax. For the systems we simulate here the instant of gas expulsion are typically 1–3 Myr, or less than 2 initial crossing times. This means that the initial substructured distributions have not had time to relax and are in the process of violent relaxation. It is worth noting that this corresponds to the age of the gas-free Orion Nebula Cluster (Jeffries et al., 2011).

We will refer to the virial ratios of the systems, $Q = T/|\Omega|$ where T is the kinetic energy, and Ω the potential energy. $Q = 0.5$ corresponds to virial equilibrium, but we note that our systems (especially initially) are often *not* in any true equilibrium, even if $Q = 0.5$ (they might be formally virialised, but may not have equilibrium spacial or velocity distributions). Nevertheless as we shall describe below Q is a very useful measure.

4.3.4.1 The Evolving Dynamical State of the Cluster

At the start of the simulation we have a very out-of-equilibrium distribution with a $Q_{\mathrm{i}} = 0$ or 0.5. The stars will immediately start to violently relax and erase the substructure present in the system (see also Allison et al. 2009; Parker et al. 2014). With our initial conditions there will always be an initial collapse of most of the stars. Violent relaxation rapidly, but very roughly, attempts to bring the system to a rough dynamical equilibrium (both virial equilibrium of the energies, and a smooth density field).

Therefore the stellar component of the system rapidly changes its density distribution, size, and the way that energy is distributed. This means that any *initial* measures of size, energy etc. rapidly change, meaning that any useful timescale such as crossing time also change.

We take as a measure of the state of the cluster the value of the virial ratio, Q, at any time as well as the rate at which the virial ratio is changing, $\dot{Q}$.

In Fig. 4.1 we show the evolution of the virial ratio with time for a typical system starting with $Q_i = 0.5$. Even though this system starts in ‘virial equilibrium’ it immediately increases its Q, and then oscillates around $Q = 0.5$ with decreasing amplitude.

What happens is that the cluster immediately starts to violently relax and attempts to collapse into the gas potential (thus Q rises as potential energy is converted into kinetic energy in the initial collapse). But the initial collapse is soon halted and the stellar distribution expands causing Q to fall, as the stars oscillate within the potential well of the cluster. Whilst this is happening substructure is also being disrupted, and within a few oscillations the system smooths out and the oscillations represent a ‘pulsation’ of a smooth cluster as it attempts to fully virialise. Therefore the oscillations in Q with time provide an internal measure of the level to which the system has relaxed.

4.3.4.2 Gas Expulsion Times

When gas expulsion occurs is (yet another) key parameter in setting the final state of the system as quantified by the final bound fraction (see Goodwin 2009; Smith et al. 2011, 2013). In our simulations this is modelled by the time at which we remove the static

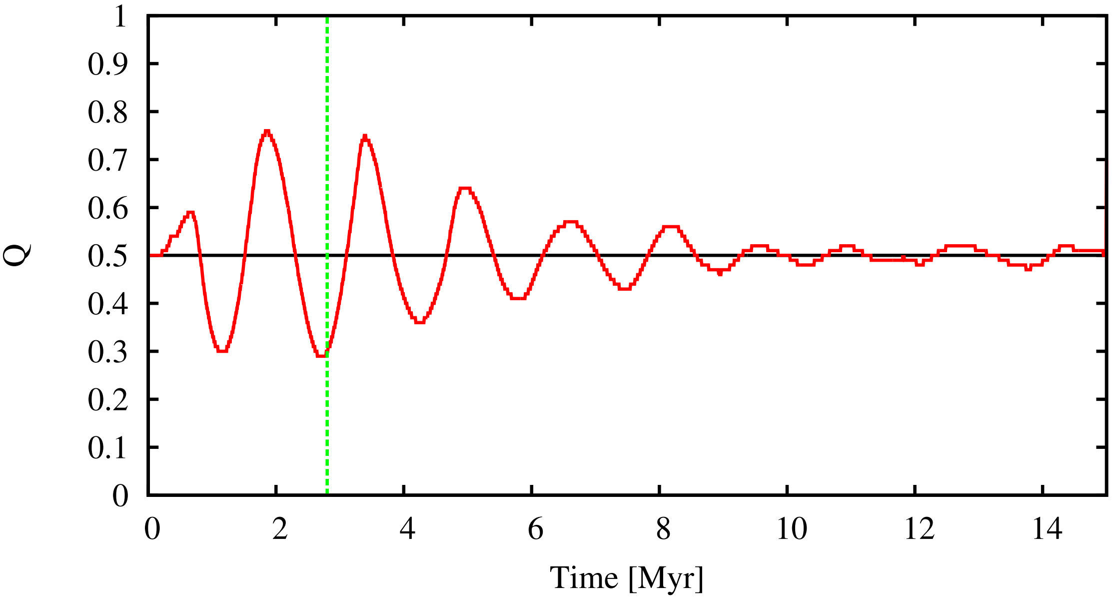

Figure 4.1: A representative example of the virial ratio variations with time of an out-of-equilibrium distribution of stars (a fractal in this case) inside a smooth background potential. As we study early gas expulsion, the smooth background potential is instantaneously removed before two crossing times occur (i.e. to the left of the vertical green dashed line).

background gas potential to represent instantaneous gas expulsion. (Obviously this is a huge over-simplification which we return to in the discussion.)

In Smith et al. (2013) we showed that the value of the virial ratio at the start of gas expulsion, Q_f, is important – is the system in an expanding or contracting part of its relaxation process? However in Smith et al. (2013), we chose a fixed instant in time for gas expulsion for all fractals. As each random realisation of a fractal evolves differently, the exact virial ratio at the moment of gas expulsion was very varied, and uncontrolled.

In order to better control the dynamical state of the cluster at the point of gas expulsion, we artificially vary the instant at which gas expulsion occurs (between 0–2 crossing times) so as we can choose the virial ratio of the cluster. The upper limit for the time of gas expulsion is marked by the green dashed vertical line in Fig. 4.1. For example, in one series of ensembles we ensure that $Q_\mathrm{f} = 0.5$ by forcing gas expulsion to occur whenever the virial ratio happens to be at $Q = 0.5$.

Obviously real systems will not always expel gas at a pre-determined value of $Q_\mathrm{f} = 0.5$, so we also expel the gas at other times as Q_f varies from subvirial ($Q_\mathrm{f} \sim 0.2$) to supervirial ($Q_\mathrm{f} \sim 0.7$).

4.3.5 The Full Set of Initial Conditions

To summarise our set of initial conditions:

We take ensembles of 10 or 20 statistically identical systems (all parameters from the same generating functions) with $N = 1000$ equal-mass stars with $M = 0.5\mathrm{M}_\odot$ distributed as a $D = 1.6$ fractal with radius 1.5 pc. The velocities of the stars are scaled to give initial virial ratios for the stellar system in the background potential of $Q_\mathrm{i} = 0$ or $Q_\mathrm{i} = 0.5$.

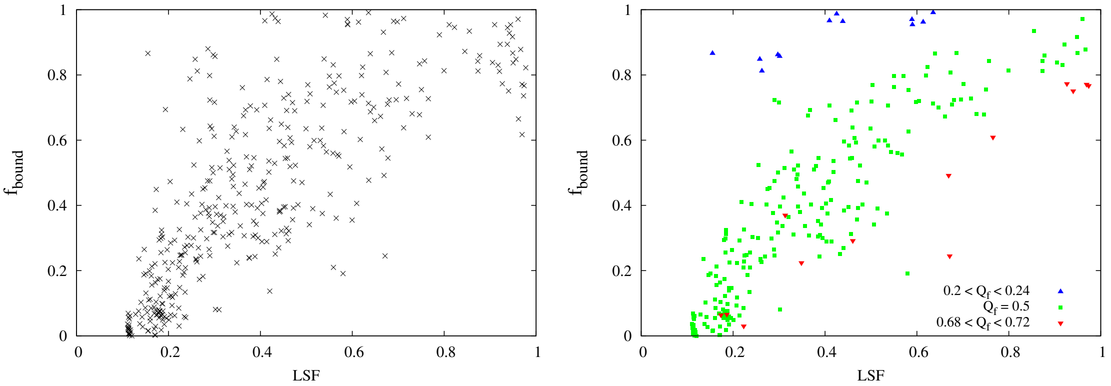

Figure 4.2: The relevance of the pre-gas-expulsion virial ratio.**Left**: Crosses show $f_{\rm bound}$ against LSF at the time of gas expulsion for all the simulations carried out in this study (see text for details). **Right**: Simulations that are highly sub-virial ($Q_{\rm f}$ = 0.22 − −0.24; blue triangles), $Q_{\rm f}$ = exactly 0.5 (green squares), or highly super-virial ($Q_{\rm f}$ = 0.68–0.72; red inverted triangles) at the instant of gas expulsion

These stellar distributions sit in a three different static background potentials. A Plummer sphere with $R_{\rm pl} = 1$ pc, a highly concentrated Plummer sphere with $R_{\rm pl} = 0.2$ pc, and a uniform sphere. All of them ith a total mass of 2500 $M_\odot$ within 1.5 pc that ensures an effective SFE = 0.2.

The systems are evolved and their time-evolving virial ratios are tracked. The instant of gas expulsion is varied in order to have gas expulsion ocur when the final stellar virial ratio has a wide range of stellar virial ratios from subvirial ($Q_{\rm f} \sim 0.2$) to supervirial ($Q_{\rm f} \sim 0.7$). At the moment of gas expulsion the local star fraction (LSF) can be calculated.

They are then evolved until the simulation reaches 15 Myr (∼10.7 initial $t_{\rm cr}$) at which the number of stars still bound in a remaining cluster can be found to give the final bound fraction, $f_{\rm bound}$.

We reiterate that these are not very ‘realistic’ initial conditions, and there is much about them that is clearly artificial. However, even as artificially simplified as they are, they are still extremely messy and complicated. Their use is not to model reality directly, but rather to allow us to probe the physics behind relaxation and recovery after gas expulsion.

4.4 Results

The key parameter that we wish to investigate is the fraction of stars that remain in a bound cluster after gas expulsion and the post-gas expulsion relaxation of the system. This ‘bound fraction’ ($f_{\rm bound}$) is the size of the naked cluster that remains. To measure the bound fraction we use the “Snowballing Method” described in Chapter 3.

4.4.1 Final Bound Fractions

In the left panel of Figure 4.2 we show the final bound fraction, $f_{\rm bound}$, against the local star fraction, LSF, for *all* the simulations we have run in this study.

There is a vague trend that a high-LSF results in a high-$f_{\rm bound}$ (i.e. the bottom right corner of the left panel of Figure 4.2 is empty). But there is a huge amount of scatter in this figure, in particular around LSF of 0.2 can result in clusters with an $f_{\rm bound}$ between zero and almost unity. For any particular value of LSF there is a scatter of at least 0.5 in $f_{\rm bound}$.

This might suggest that there is no way of estimating the final bound fractions of star clusters after gas expulsion. We show below that it is possible to understand the system and fairly accurately predict the final bound fractions if one knows both the LSF and stellar virial ratios at the time of gas expulsion.

Because of how we have (rather artificially) chosen our gas expulsion times we can split the simulations shown in the left panel of Figure 4.2 into groups depending on their final virial ratios. In the right panel of Figure 4.2 we only plot the simulations with $0.22 < Q_{\rm f} < 0.24$ (blue), $Q_{\rm f} \sim 0.5$ (green), and $0.68 < Q_{\rm f} < 0.72$ (red).

It is clear from the right panel of Figure 4.2 that a significant amount of the scatter is due to the value of $Q_{\rm f}$ at the time of gas expulsion. The $0.22 < Q_{\rm f} < 0.24$ simulations all have $f_{\rm bound} \sim 1$. The $Q_{\rm f} \sim 0.5$ simulations show a rapid increase in $f_{\rm bound}$ with LSF for low-LSF, then a very roughly linear increase. And the $0.68 < Q_{\rm f} < 0.72$ simulations show a roughly linear increase in $f_{\rm bound}$ with increasing LSF.

4.4.2 A Simple Physical Model

In Fig. 4.3 we plot $f_{\rm bound}$ against LSF for bins of different $Q_{\rm f}$ increasing from low-$Q_{\rm f}$ in the top left to high-$Q_{\rm f}$ in the bottom right. Systems with initial virial ratios of $Q_{\rm i} = 0.5$ are marked by filled circles, those with $Q_{\rm i} = 0$ by open circles.

The black solid lines and blue dashed lines are a simple model fit to the data which we describe in this section. Note that the colours show the form of the gas potential which we will describe in the next subsection. For now we will concentrate on building a simple model to fit the $f_{\rm bound}$ against LSF trends with different $Q_{\rm f}$.

We can construct a very simple analytical model that fits the results of our simulations surprisingly well (see Boily and Kroupa 2003 for a similar, but rather more detailed derivation).

As described above and in Smith et al. (2011), the initial fractal stellar distribution will attempt to relax and virialise within the gas potential. What are important for the impact of gas expulsion are two quantities *at the time of gas expulsion*: the virial ratio $Q_{\rm f}$ of the stars relative to the gas and the local stellar fraction LSF. The LSF measures the relative masses of the gas and the stars within the stellar half-mass radius (see above). Therefore the total mass (stars plus gas) $M_{\rm tot}$ in the region in which the stars are present is $M_{\rm tot} \sim M_*/{\rm LSF}$.

Let us denote quantities just before the gas expulsion with index 1 and just after the gas expulsion with 2.

One quantity of interest is the kinetic energy T_* of the stars, set by their velocity dispersion σ_*. If we assume a Maxwellian velocity distribution, the kinetic energy is given by:

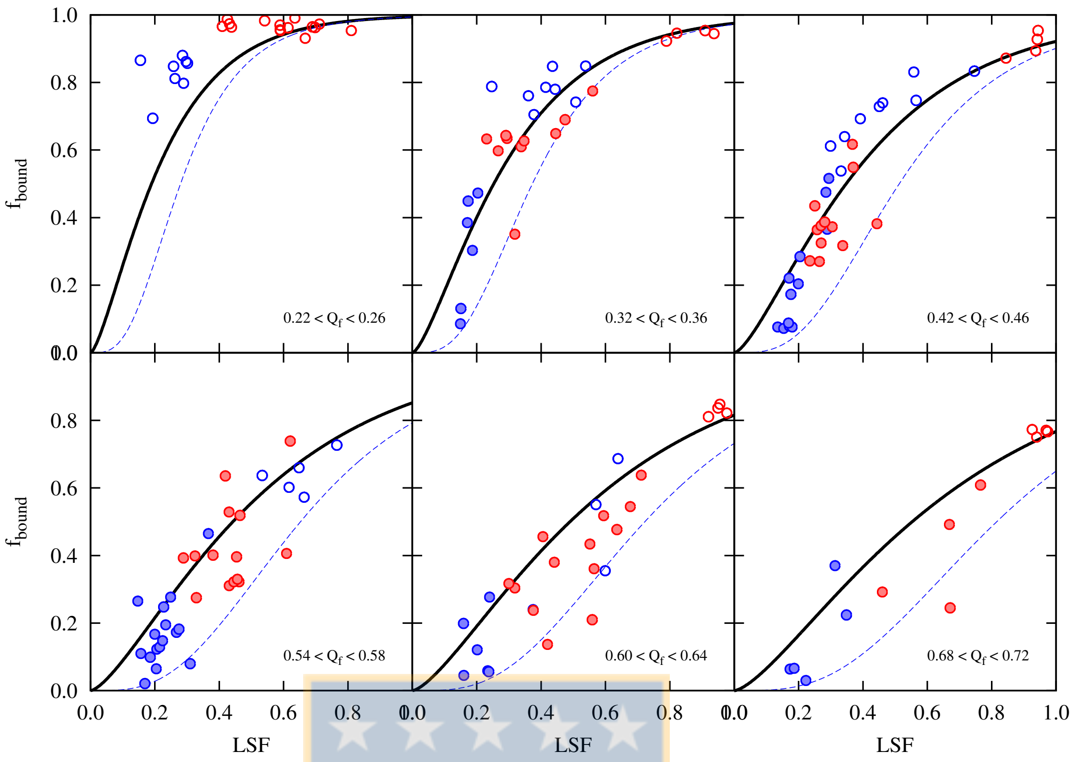

Figure 4.3: The $f_{\rm bound}$-LSF trend for different virial ratios. Colors represent the shape of the background gas, a Plummer sphere (blue) and a uniform sphere (red), filled circles are simulations with $Q_{\rm i} = 0.5$ and open circles are distributions with $Q_{\rm i} = 0.0$. The black solid lines and blue dashed lines are the fits from the model described in sec. 4.4.2.

$$T_{*,1} \quad = \quad \frac{3}{2} M_* a^2 \tag{4.1}$$

where a is the scale factor of the Maxwellian velocity distribution. a is related to the velocity dispersion as $a^2 = \sigma_*^2 \pi/(3\pi - 8)$. Therefore,

$$T_{*,1} \quad = \quad \frac{3\kappa}{2} M_* \sigma_*^2 \tag{4.2}$$

where $\kappa = \pi/(3\pi + 8)$. After gas expulsion the stars have not had time to change their kinetic energy (since the gas is expelled instantaneously) and so we can assume $T_{*,2} = T_{*,1}$.

The potential energy of the stars before gas expulsion can be approximated by

$$\Omega_{*,1} \quad \sim \quad -M_* \frac{GM_{\rm tot}}{r_{\rm h}} \tag{4.3}$$

were G is Newton's gravitational constant, while the potential energy after the gas is lost is only due to the potential made by the stars alone

$$\Omega_{*,2} \quad \sim \quad -M_* \frac{GM_*}{r_{\rm h}} \quad = \quad \mathrm{LSF}\ \Omega_{*,1}. \tag{4.4}$$

Now we calculate the escape velocity of the system after the gas is gone as

$$v_{\rm esc} \sim \sqrt{-\frac{2}{M_*}\Omega_{*,2}}. \tag{4.5}$$

If we now replace $\Omega_{*,2}$ by LSF times $\Omega_{*,1} = -T_{*,1}/Q_{\rm f}$ we have

$$v_{\rm esc} = \sqrt{3\kappa}\sqrt{\frac{\rm LSF}{Q_{\rm f}}}\sigma_*. \tag{4.6}$$

A reasonably first guess of $f_{\rm bound}$ would be the fraction of stars with velocities below the escape velocity. If we assume a Maxwellian velocity distribution, then $f_{\rm bound}$ is given by its cumulative probability distribution with the form:

$$F(<X) = {\rm erf}\left(\frac{1}{\sqrt{2}}X\right) - \sqrt{\frac{2}{\pi}}X\exp\left(-\frac{X^2}{2}\right) \tag{4.7}$$

where $X = v_{\rm esc}/a$. Since $a^2 = \kappa\sigma_*^2$ then $X = v_{\rm esc}/\sqrt{\kappa}\sigma_*$ and finally:

$$f_{\rm bound} = {\rm erf}\left(\sqrt{\frac{3}{2}\frac{\rm LSF}{Q_{\rm f}}}\right) - \sqrt{\frac{6}{\pi}\frac{\rm LSF}{Q_{\rm f}}}\exp\left(-\frac{3{\rm LSF}}{2Q_{\rm f}}\right). \tag{4.8}$$

In Fig. 4.3 we show $f_{\rm bound}$ against LSF for various values of $Q_{\rm f}$. The solid black line is the fit from above which has no free parameters. This simple model describes the data points of our simulations very well, especially if we look at high LSF and low $Q_{\rm f}$ values, i.e. when we do not lose many unbound stars (upper panels).

When we have high $Q_{\rm f}$ values as in the lower panels of Fig. 4.3 the simple model (solid black line) tends to over-estimate the final bound fraction. We can apply a simple correction. Following the first estimate of $f_{\rm bound}$ a fraction of stars is lost very rapidly after gas expulsion, and so the escape velocity falls by a further factor $\sqrt{f_{\rm bound}}$ in Eq. 4.6. We then have to solve Eqs. 4.6 and 4.7 iteratively which gives the blue dashed-lines in Fig. 4.3. In most cases the true values of $f_{\rm bound}$ are enclosed between the solid black and blue dashed-lines suggesting that reality is somewhere inbetween.

We have constructed a simple analytic approximation with no free parameters that estimates the final bound fraction from the values of the stellar virial ratio and LSF at the moment of gas expulsion. Given the simplifying assumptions we have made it is very gratifying that this seems to explain the results so well.

4.4.3 The effect of the gas potential

In Fig. 4.3 points are coloured according to the form of the gas potential: blue is a Plummer potential, and red a uniform sphere. There appears to be a very strong dependency on the form of the gas potential. In Fig. 3 systems with concentrated gas potentials ($R_{\rm pl} = 1$ pc) shown by the blue markers are concentrated to the left of each panel with low LSF and low $f_{\rm bound}$. Systems with extended gas potentials ($R_{\rm pl} = \infty$) shown by the red markers are towards the right with higher LSF and $f_{\rm bound}$.

Taken at face value this suggests that the form of the gas potential is crucial in determining the fate of a system. However, this is not the case. Rather it is due to a link between the form of the gas potential and the possible values of the LSF. The LSF measures the relative masses of gas and stars within the half-mass radius of the stars. Gas outside this radius is not taken into account. Even though the total mass in gas in the whole star forming region stays constant, the LSF fluctuates as the half-mass radius of the stars fluctuates (this is the motivation for the introduction of the LSF by Smith et al. (2011).

In a bound, fractal distribution the stars can do nothing except collapse to a denser (and smoother) configuration. Much of the initial potential energy in a fractal distribution is localised in substructure and is redistributed during violent relaxation. The potential energy, Ω, of a system is

$$\Omega \sim -A\frac{GM^2}{R} \tag{4.9}$$

where M is the mass of the system and R some characteristic radius (and G the gravitational constant). A is a measure of the mass distribution of the system. For a Plummer sphere, if R is the Plummer radius then $A \sim 0.3$. But for a $D = 1.6$ fractal, when R is the initial size of the system, $A \sim 1.5$. Therefore, the violent relaxation of a fractal causes a significant decrease in the size of the system (see Allison et al. 2009 for details).

Exactly how such a system will contract depends on the exact details of the initial fractal distribution, the initial virial ratio ($Q_{\rm i} = 0$ systems will contract more than $Q_{\rm i} = 0.5$ systems) and how relaxed the system has become. However, we find it does not depend on the shape of the background gas potential, as shown in Fig. 4.4. In the upper panel, symbols with error bars are the average LSF of simulations at the moment of gas expulsion. We include data points for (from left to right) $R_{\rm pl} = \infty$ (uniform gas), $R_{\rm pl} = 1$ pc, and also $R_{\rm pl} = 0.2$ pc (a very concentrated gas distribution). On the x-axis, we plot $1/R_{\rm pl}$ in order to place all simulations on the same plot. There are two curves for the two different initial virial ratios ($Q_{\rm i} = 0.0$ and 0.5). There is a clear trend for the LSF to be lower as the gas becomes increasingly concentrated. To understand this, we must bear in mind that the LSF is a function of the total gas mass within the half mass radius of the stars. Therefore a change in LSF could arise from either a change in the amount of gas surrounding the stars, and/or a change in the half-mass radius of the stars as the gas scale length is varied. We find that the half-mass radius is only a very weak function of the gas scalelength as shown in the lower panel of Fig. 4.4. Here symbols with error bars are the average half-mass radius $R_{\rm h}$ of the stars. This weak dependency demonstrates that the strong dependency of the LSF on gas scalelength arises mainly for the following reason – by making the gas more concentrated, more gas is being placed about the stars, and the LSF is lowered.

To confirm that the small variation in $R_{\rm h}$ with gas scalelength does not play a strong role, we calculate the average $R_{\rm h}$ for each set (see horizontal dashed lines in the bottom panel of Fig. 4.4). Now we fix $R_{\rm h}$ to have the average value (i.e a constant value for all gas scalelengths) and recalculate the LSF values at their new half-mass radius. The results are indicated by the brown dashed lines in the upper panel. The trend of LSF with gas scalelength is very similar, even when the stellar half-mass radius is fixed to be constant. This confirms that the strong dependency of the LSF on gas scalelength arises almost entirely for the following reason. Increasing the gas concentration places more gas about the stars, and does not change the stellar distribution significantly.

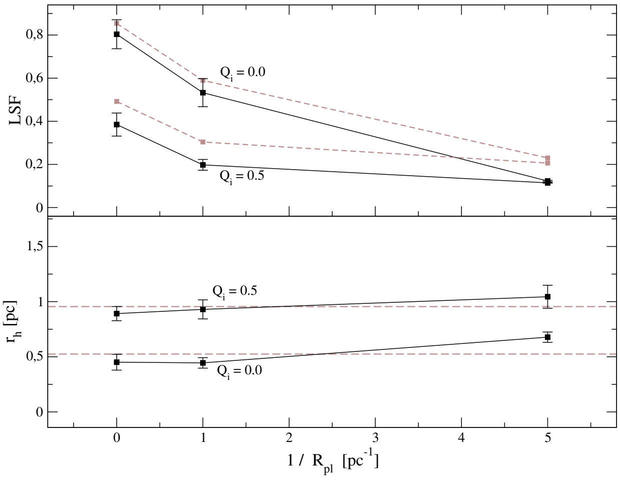

Figure 4.4: The variation of the LSF of the clusters due to the change in the concentration of the background gas. Top panel: The average of the LSF of the simulations against the inverse of their scale lengths. A black solid line connects simulations with the same initial virial ratio as labelled. Bottom panel: The half mass radius is only weakly dependent on the gas scale length. The average is shown by the horizontal dashed line. The brown dashed line in the upper panel is the recalculated LSF using a fixed half-mass radius with the average value.

4.5 Discussion and Conclusions

Initially clumpy and irregular distributions of stars cannot be in dynamical equilibrium. As a result, they undergo violent relaxation with initially significant changes in their virial ratio as they expand and collapse, attempting to approach equilibrium. This occurs even when the clusters are initially 'virialised' (ie. $Q_\mathrm{i} = 0.5$). These deviations are largest for very young star clusters, and decrease as the cluster settles down, as substructure is erased. As a result, the effects of gas expulsion at early times, before the system has relaxed, depend strongly on the instantaneous value of the virial ratio as well as the Local Star Fraction (LSF, relative distribution of stars in the gas potential).

At later stages (>2 crossing-times), it is known that the LSF becomes the key predictor of cluster survival from gas expulsion, with second-order modifications due to the cluster's dynamical state (Smith et al., 2013). However at these early stages when oscillations in the virial ratio are so large, we have shown that the dynamical state of the cluster may actually be equally influential (if not more influential) than the LSF.

A primary goal of studying the response of young, embedded star clusters to gas expulsion is to predict how well a cluster survives gas expulsion, based on its pre-gas expulsion properties. This study reveals that both the LSF, and the dynamical state can be important parameters dictating cluster survival to gas expulsion. Fortunately in our numerical studies, we can ascertain the exact value of the LSF and virial state. However, observationally, it may be incredibly challenging to measure either of these properties accurately. It is not inconceivable that the LSF might be calculated approximately by deprojection, although it would need to be a cluster caught very close to the instant of gas expulsion, or the LSF may later change. However, measuring the virial ratio of a real cluster is a huge challenge.

To worsen matters, our study reveals that in certain circumstances, even with a knowledge of both the LSF and virial ratio, the cluster survival maybe poorly constrained. For example, take a cluster with a low virial ratio (e.g Q_f=0.34 at gas expulsion; upper-left panel of Fig. 4.3). If the cluster has an LSF∼0.2 (a reasonable physical value), the f_bound-LSF trend rises very steeply. Such a cluster is equally likely to be near destroyed (have $\sim 90\%$ of its stars unbound), as only weakly affected (losing $\sim 30\%$ of its bound stars). Thus it is possible that, even if the virial ratio were measured, the result could place the cluster in a region of parameter space where the cluster survival could be anything from weak mass loss to near total destruction.

Comparing the panels of Fig. 4.3, we can see that clusters with LSF$\sim$0.2-0.4 are the most sensitive to their dynamical state. In comparison clusters with high LSF vary their resulting bound fractions very little, even for large changes in dynamical state. If LSF$\sim$0.2 is a typical value, then these results suggest that clusters which are observed post-gas expulsion, must have been sub-virial to avoid losing a large fraction of their stellar mass during the process.

Clearly our models are extremely simple conceptionally. They lack a large number of physical processes that are also highly important in young star clusters. For example, our cluster stars have no initial mass function, we start our simulations with no binaries, we do not consider stellar evolution, and our treatment of the gas is highly simplified. Nevertheless, the use of such simple idealised models has enabled us to clearly determine the significant role of clumpy substructure and the dynamical state of the clusters on cluster survival following gas expulsion, through the use of controlled numerical experiments. This approach has revealed just how sensitive star clusters are to their dynamical state when gas expulsion occurs. We therefore suggest that real star clusters will be very sensitive, perhaps as sensitive as our model star clusters, to their dynamical state when the gas is expelled at early times.

Our key results may be summarised in the following:

1. For early gas expulsion (before 2 crossing-times) we find the dynamical state of our model star clusters, measured at the time of gas expulsion, plays a key role in influencing cluster survival following gas expulsion. Star clusters may be highly super- or sub-virial in these early phases.
2. We show how the f_{bound}-LSF trend can be well approximated with a very simple analytical model. The model matches the simulations best when the dynamical state is not extreme (i.e highly super- or sub-virial).
3. Clusters which have LSFs in the range 0.2-0.4 (physically reasonable values) are most sensitive to the virial ratio at the instant of gas expulsion.
4. Clusters with low virial ratio have a very steep rise in the f_{bound}-LSF trend. For such a cluster with an LSF~ 0.2, it is therefore not possible to predict if the cluster will be heavily destroyed or only mildly affected – even knowing both the LSF and the virial ratio.

This study highlights the difficulties faced in trying to determine the survival rate(s) of real star clusters due to gas expulsion. At early times, the dynamical state of a cluster may be far from dynamical equilibrium, and this can significantly affect the clusters survival to gas expulsion. Thus a best estimate of a cluster's survival is found measuring both the LSF and virial ratio. Accurately measuring these two parameters for a real cluster represents a huge observational challenge, in particular the dynamical state. Furthermore, some clusters may be situated in regions of parameter space where their survival to gas expulsion remains highly uncertain, even knowing both the LSF and virial ratio.

Chapter 5

Fractal Clusters Embedded in an Adiabatic Gas

As a first step in the complexity of embedded clusters, we evolve the same systems used in Chapter 4, i.e., fractal distributions under the influence of a static Plummer background potential, but now we advance one step further utilizing dynamically live Plummer spheres in hydrostatic equilibrium instead of a static background gas.

5.1 Setup

We evolve exactly the same systems used in Chapter 4, i.e., fractal distributions (see Goodwin and Whitworth, 2004) of $N = 1000$ star particles inside a radius of $R = 1.5$ parsec. This stellar cluster is embedded in a Plummer sphere of gas with a mass of $M_{\mathrm{pl}} = 3472.0\ \mathrm{M}_{\odot}$ and Plummer radius of $R_{\mathrm{pl}} = 1$ parsec. This setup ensures a global SFE = 0.2 inside the radius of the stellar distribution.

We model the gas using the SPH scheme described in Sec.2.4 using $N_{\mathrm{gas}} = 100K$ SPH particles with an adiabatic equation of state with adiabatic index of $\gamma = 5/3$. Initially the gas cloud is in hydrostatic equilibrium, however the inclusion of an external system, such as the stellar cluster, removes the gas from equilibrium. In order to avoid the initial contraction of the we gas set the specific internal energy of each SPH particle to:

$$u_{\mathrm{i}} = -\frac{\phi_{\mathrm{i}}}{6(\gamma - 1)}, \tag{5.1}$$

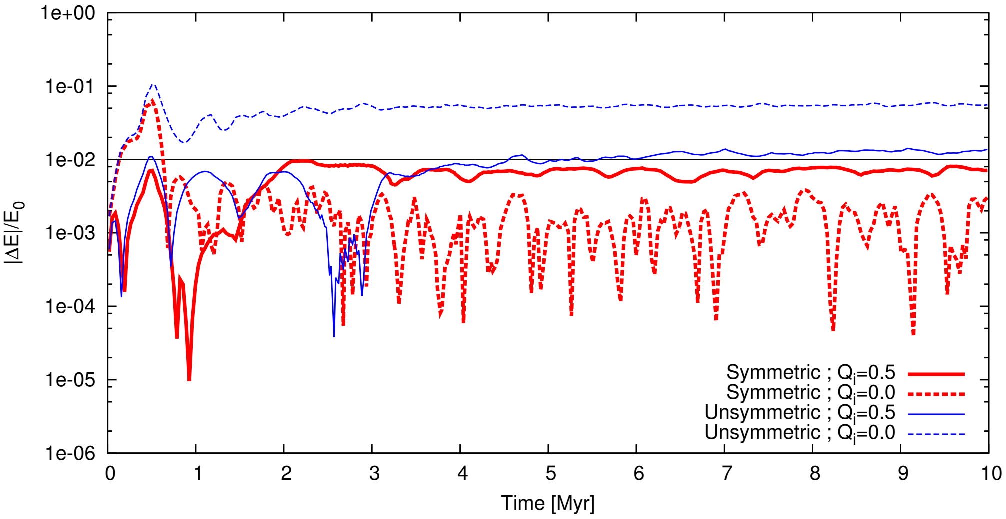

Figure 5.1: Energy conservation when using symmetrical and unsymmetrical interactions. Symmetrical interactions (red thick lines) show energy conservations below 1% at all times. Instead errors are around ∼ 1 to 7% when using unsymmetrical interactions (blue thin lines). In both cases error peaks occur when $Q_{\rm i} = 0.0$ where the initial relaxation is the hardest to follow due to massive amount of close encounters.

where $\phi_{\rm i}$ is the gravitational potential at the position of the SPH particle .

In the same way the inclusion of an external potential like the gas removes the fractal distribution from virial equilibrium, thus stellar velocities are scaled by a factor (see Aarseth, 2003):

$$Q = \sqrt{\frac{Q_{\rm vir}|V|}{K_{\rm star}}} \tag{5.2}$$

where $Q_{\rm vir}$ is the desired Virial ratio of the stellar distribution, $K_{\rm star}$ is the kinetic energy of the stars, and V is the virial energy calculated as:

$$V = -\sum_{i}^{N} m_i \mathbf{r}_i \cdot \mathbf{a}_i \tag{5.3}$$

We follow simulations with two initial virial ratios as in Chapter 4, i.e., initially cold with $Q_{\rm i} = 0.0$ and initially warm with $Q_{\rm i} = 0.5$

We follow the evolution of the embedded cluster for $t_{\rm max} = 15$ Myr which is $\sim 10 t_{\rm cross}$ with an initial crossing time of about $t_{\rm cross} \approx 1.5$ Myr.

5.2 Energy Tests

With the freedom that AMUSE gives us to set up our simulations, special care must be taken in order to obtain valid results. We perform several energy tests with our simulations. This is most important for the setup of the Bridge integrator (see Sec. 2.2.1).

As discussed in Chapter 2, stars are simulated using the direct N-body code Ph4 and gas is modelled using the Hybrid Tree/SPH code Fi. Interactions are done using the Bridge scheme mutually kicking both systems using their own internal scheme to calculate the gravity that the other system will feel from it i.e. kicking from gas to stars would be using a Tree code (from FI) and kicking from stars to gas would be done utilising a direct method (from PH4). To this setup we refer as an *unsymmetrical* interaction.

It is also possible to use a different implementation of the Barnes and Hut (1986) Tree scheme in order to kick the systems using the same numerical method. We refer to this setup as a *symmetrical* interaction.

Symmetrical interactions are proven to better conserve energy as we show in Fig. 5.1. With this setup we achieve energy conservations below 1% even at initially cold simulations where close encounters make the conservation of energy even more difficult in the system. For this reason we perform all simulations in this work using symmetrical interactions.

Energy errors of 1% are the typical errors of a second order integrator as the Leapfrog scheme. PH4 by itself for example, can achieve energy errors of the order of $\Delta E/E_0 \sim 10^{-4}$. However it doesn't matter how good individual integrators are, it is not possible to decrease errors more than that, because we are limited by the interaction scheme.

This is a particular problem when comparing with simulations of Chapter 4 since we used a fourth order direct integrator in NBODY6. Any physical process that we add to the cluster, e.g., feedback from stars, stellar evolution, stellar winds and in this case hydrodynamics, will come with their own numerical errors. However, this is the price we have to pay if we want to advance further in the complexity of modelling embedded star clusters.

5.3 Evolution of Clusters Without Gas Expulsion

We follow the evolution of the embedded clusters for 15 Myr. In this section we examine the simulations observing the time evolution of several parameters of the clusters that we believe are critical to consider when trying to predict if a cluster would survive gas expulsion or not.

5.3.1 Influence of the Global SFE

We take one fractal distribution and analyse how it affects the surrounding gas via gravity. As described in Sec. 5.1 we setup our initial conditions in order to have an initial cluster in thermal and virial equilibrium. However, stars may match virial equilibrium velocities but they are not in dynamical equilibrium. Since the distribution is substructured, the stellar cluster will relax and rearrange in order to pursuit a spherical and equilibrium state. This means, that the cluster will contract into a denser distribution which is not the distribution that the gas was setted in equilibrium at the beginning of the simulation.

In order to compare with static simulations we want to be sure that the gas distribution will remain as a Plummer sphere all over the simulation. To test what would be needed to change the gas distribution we perform simulations using different SFE for the same fractal. We setup the different SFE changing the total mass of the gas from a maximum mass of $M_{\rm pl} = 7812.02$ $M_\odot$ to a minimum mass of $M_{\rm pl} = 96.5$ $M_\odot$ ensuring the desired

SFE inside the $R = 1.5$ pc of the stellar distribution. We perform simulations using SFE of 10%, 20%, 40%, 60% , 80% and 90%.

We analyse the evolution of the radial distribution of the stars and the gas with a initially cold cluster ($Q_{\rm i} = 0.0$) and a warm one ($Q_{\rm i} = 0.5$).

Fig. 5.2 shows the evolution of several Lagrangian radii for the stars (black lines) and for the gas (shaded areas) for the different SFE tested in this thesis. Panel (a) shows simulations started with $Q_{\rm i} = 0.5$ where we can see how the gaseous component does not considerably react to the initial relaxation of the stars. Only when the SFE is higher than 60% the gas shows a slight relaxation. The stellar component seems to rearrange into a similar distribution no matter the SFE, however it is possible to see by eye that the outer Lagrangian radii of the cluster (the 99% and 100% mass radius) expand with the SFE and the core radius (1% to 10% mass radius) seems to decrease, suggesting a change in the radial distribution of the stars. Panel (b) of Fig. 5.2 shows simulations with $Q_{\rm f} = 0.0$ where the extreme contraction of the stellar distribution is not enough to cause a significant change in the gas distribution.

To show how the final density distribution of both, the gas and stars, changes with the SFE we measure the time average density profile of the cluster for $t > 2\ t_{\rm cross}$ to avoid the initial relaxation phase. Fig. 5.3 shows the resulting profiles for the gas (blue circles) and the stars (red crosses). To measure how much the cluster contracts we fit Plummer density profiles to both distributions using $R_{\rm pl}$ as a free parameter. Fig: 5.4 shows the values of $R_{\rm pl}$ for the stellar component for each panel of Fig. 5.3. Simulations with $Q_{\rm i} = 0.5$ are represented by filled circles connected by a solid line, and simulations with $Q_{\rm i} = 0.0$ are represented by open circles connected by a dashed line. We can see a decrease of $R_{\rm pl}$ with SFE for the warm simulations. We can see that with $Q_{\rm i} = 0.5$ stars contract more and more when the gas mass is less important. In contrast when $Q_{\rm i} = 0.0$ the stellar distribution rearrange into the same distribution no matter the SFE, with the exception of the highest SFE where the density profile is more irregular.

The decrease of $R_{\rm pl}$ is explained by the decrease in the contribution of the gas component to the cluster potential. With a lower potential energy stars feel less acceleration and stellar velocities are lower. Thus, stars are allowed to fall more into the cluster's center. However, this also increases the chance of a particle to be kicked by close encounters, allowing them to escape from the center to end up orbiting in the outer layers of the cluster. How large these orbits are also depends of the cluster potential. With a weaker cluster potential the escape velocity is lower and stars affected by close encounters get velocities closer to the escape velocity so they travel further than in the presence of a stronger potential.

However, this is not the case for clusters with cold initial conditions. In this case stars have the same chances to suffer two body encounters no matter the SFE because in all cases they start falling straight to the center but stars that are affected will still travel further with a less massive gas background but there are not enough encounters to change the density profile of the density distribution.

The collapse of the gaseous component is inhibited by thermal pressure. A change in the distribution of the stars into a denser state increases the potential felt by the gas making the gas sphere collapse raising the temperature at the center because of the compression. However, the change in the potential due to the rearrangement of the stars alone is not enough to compress the gas sphere considerably, no matter how high the SFE is.

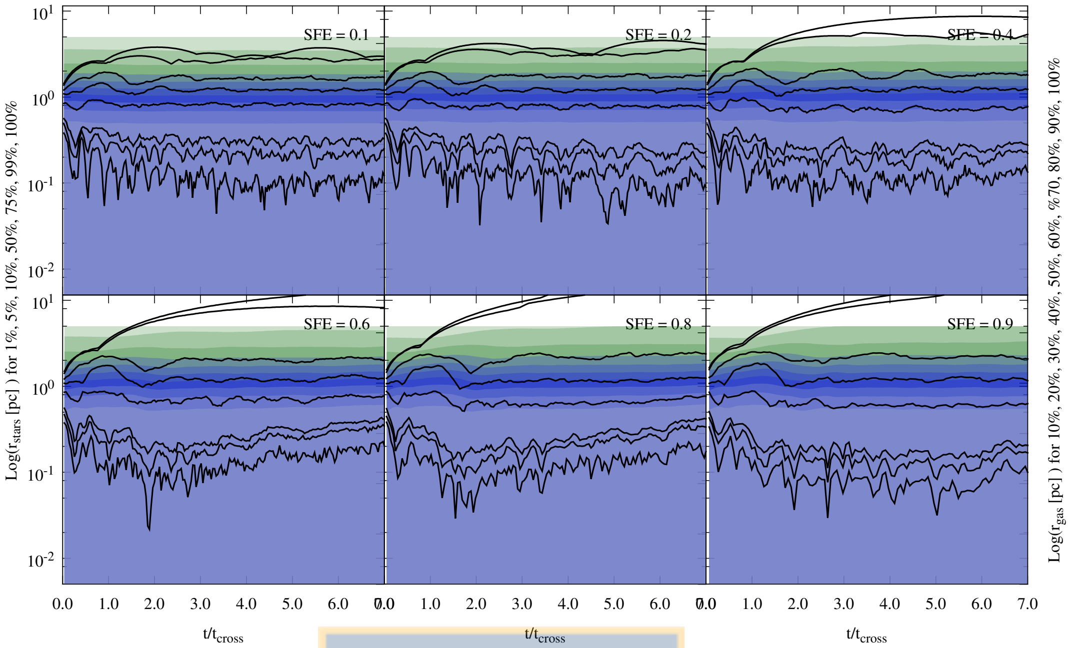

(a) $Q_{\rm i} = 0.5$

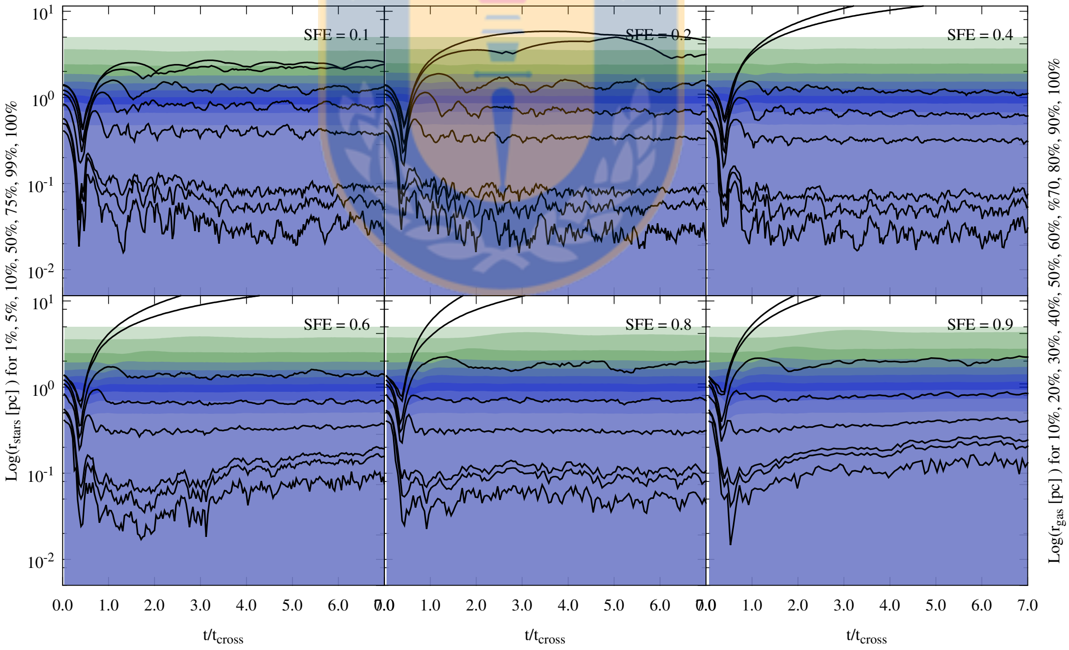

(b) $Q_{\rm i} = 0.0$

Figure 5.2: Evolution of the same fractal distribution under different SFE. Lagrangian radii for stars (black lines) and gas (green and blue shaded areas) are displayed. We see that stars do not affect notably the background gas even with high SFE even if they extremely contract. The stellar component is not considerably affected, only the outer layers are able to escape further because a in the initial contraction some stars get high velocities that at low SFE the strong gas potential is able to retain, however the rest of the cluster behaves similarly no matter the SFE.

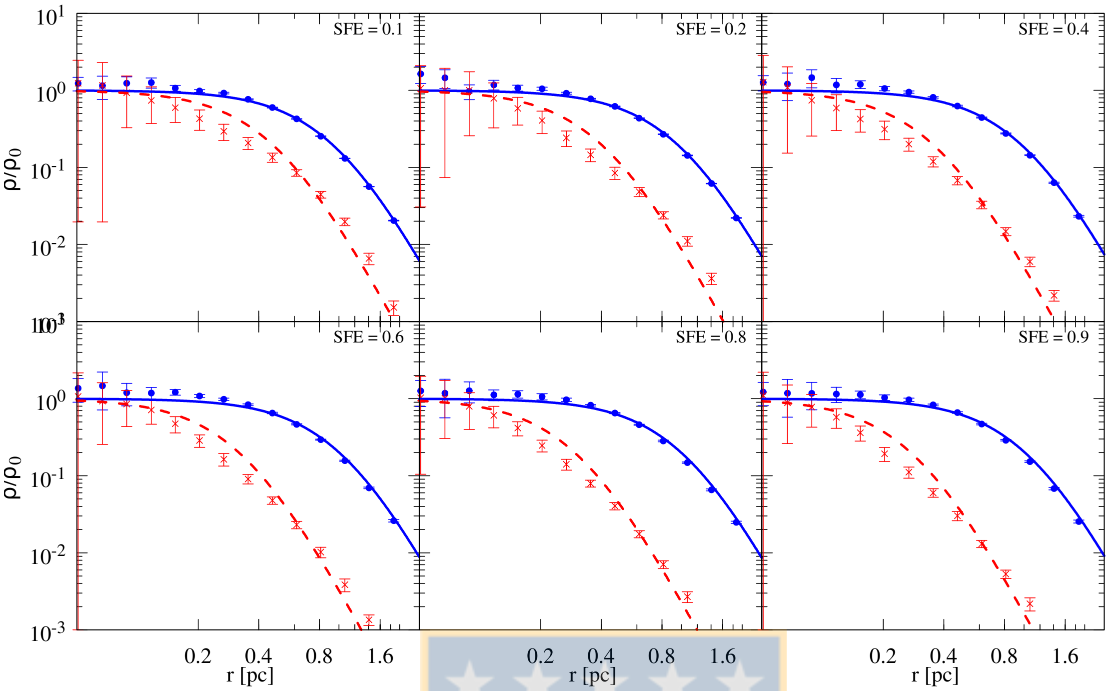

(a) $Q_{\mathrm{i}} = 0.5$

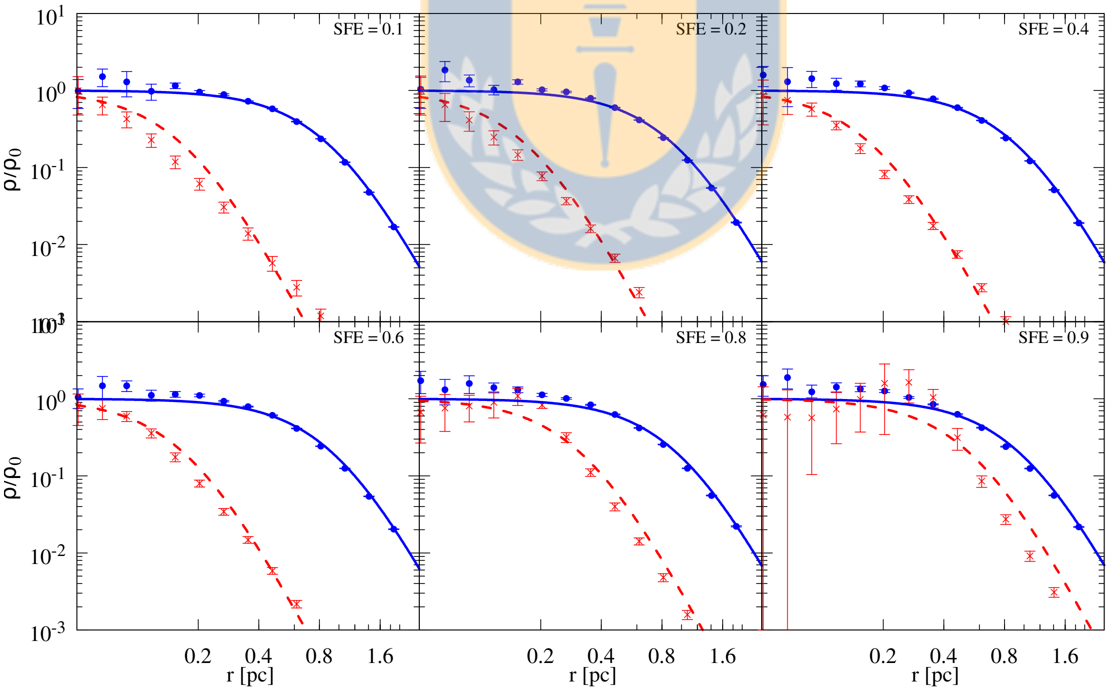

(b) $Q_{\mathrm{i}} = 0.0$

Figure 5.3: Mean density profiles of the gaseous and stellar distributions. Stellar profiles are shown in red crosses and gaseous profiles are shown in blue circles. Means are measured during the evolution of clusters after 2 t_{cross} to avoid the relaxation phase. Density distributions are fitted with Plummer profiles with R_{pl} as a free parameter.

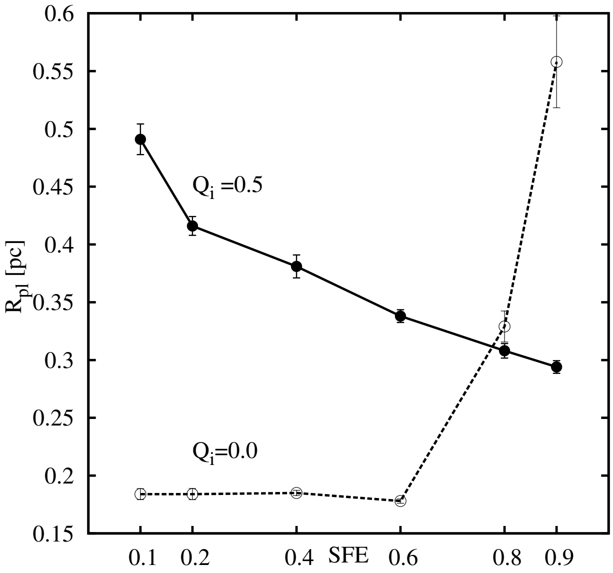

Figure 5.4: The change of $R_{\rm pl}$ as a function of the SFE. We see that fractal distributions with $Q_{\rm i} = 0.5$ (filled circles and solid line) collapse into denser distributions depending of the SFE while the same distributions starting with no velocities ($Q_{\rm i} = 0.0$, open circles and dashed line) collapse into same spherical distribution except when SFE ≥ 0.8.

5.3.2 Evolution of Q and the LSF

As we show in Chapter 4, the critical parameters that determines if a cluster survives explosive gas expulsion or not are the dynamical state of the cluster at the moment of gas expulsion represented by $Q_{\rm f}$ and the relative amount of stellar mass with respect to the total mass of the cluster when gas expulsion begins, the final LSF. Naturally, we wonder, if the inclusion of gas, that is able to evolve, would affect any of this parameters.

First, we compare the amplitude of the Q oscillation measured by $|Q-0.5|$. How quickly this quantity drops to zero means how quickly the cluster can reach equilibrium and erase primordial substructure. We measure the mean value of $|Q-0.5|$ for the 20 fractal clusters used in this work and show the results in Fig. 5.5 where the blue lines are the means with blue shaded areas as the standard deviation. Black dashed lines represent the same quantities measured in the simulations from Chapter 4 with the central line as the mean and the two other lines as the standard deviation.

We notice that there is no significant difference between the static and the live gas case. Neither with initially cold (bottom panel) or initially warm cluster a significant difference can be found. Still, in both panels the amplitude of the live gas case seems to remain slightly above the static potential case with standard deviation quite higher in the initially warm case. However, the difference is smaller than one sigma and could be explained by the difference in the numerical integrators used in the static and the live gas case.

With the same method we obtain the time averages of the LSF. The resulting LSF evolution is shown in Fig. 5.6. Simulations with a live gas background show a higher LSF than in the static case, but still within the one σ deviation, so the difference is not significant. However, if we assume that the gas background remains as a Plummer sphere of $R_{\rm pl} = 1.0$ pc, which is not a bad assumption if you check Fig. 5.2 and 5.3, then the only possibility to raise the LSF is a decrease of the half mass radius of the stars. The main reason for the half mass radius to decrease is the interchange of angular momentum between the stars and the gas. Fig. 5.7 shows the evolution of the angular momentum for the stars (dashed lines) and the gas (dotted lines). The top panel shows the mean angular momentum L relative to the total initial momentum $L_{\rm tot,i}$ for fractals with

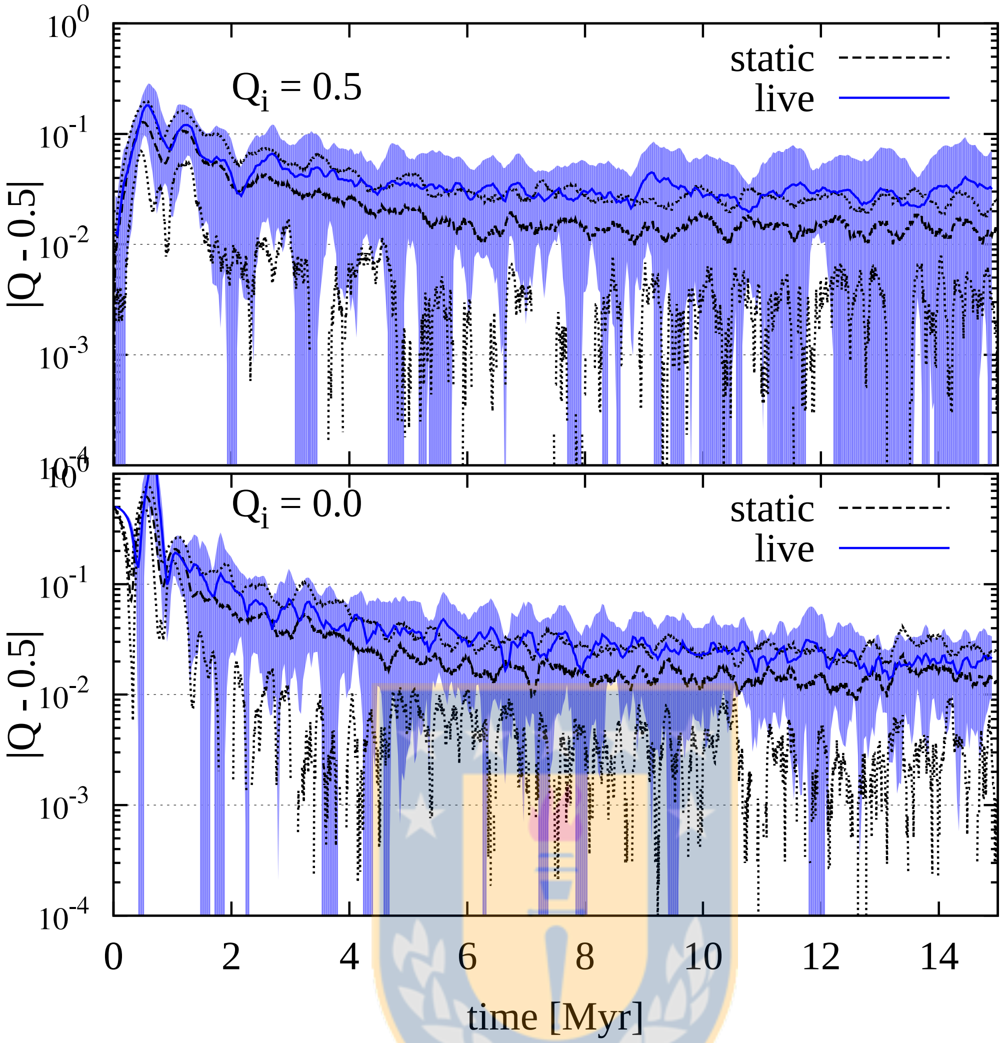

Figure 5.5: The evolution of the amplitude of Q. Blue solid lines with blue shadow areas show the mean amplitude of Q for the live gas simulations carried out in this work with its standard deviation. Black line with dashed lines represent the mean amplitude of simulations carried out in Chapter 4.

$Q_\mathrm{i} = 0.5$ shadows represent the standard deviation. The bottom panel shows fractals with $Q_\mathrm{i} = 0.0$. Since the clusters start with no initial velocities, hence no initial angular momentum, values are measured with respect to the final total angular momentum of the cluster $L_\mathrm{tot,f}$.

For the initially warm case, we see that while the total angular momentum is more or less conserved, the gas obtains angular momentum from the stars, fast in the relaxation phase and slowly after the clusters rearrange causing a decrease in the velocities of the stars and thus a decrease in the half mass radius. As we can see from the standard deviation gas can gain up to $\sim 20\%$ of the initial angular momentum in the warm case.

While in the initially cold case this interchange seems to be more important, this is only because the value of the initial angular momentum is lower. In this case stars start with no velocities and $L_\mathrm{tot,i}$ is zero so all the angular momentum that the cluster reaches comes from the violent initial relaxation and does not increase too much. In fact the maximum angular momentum for the gas is quite similar in both cases with 17.3 ± 0.7 M$_\odot$pc km/s for the initially warm case and only a 20% lower in the cold case with 14.1 ± 0.5 M$_\odot$pc

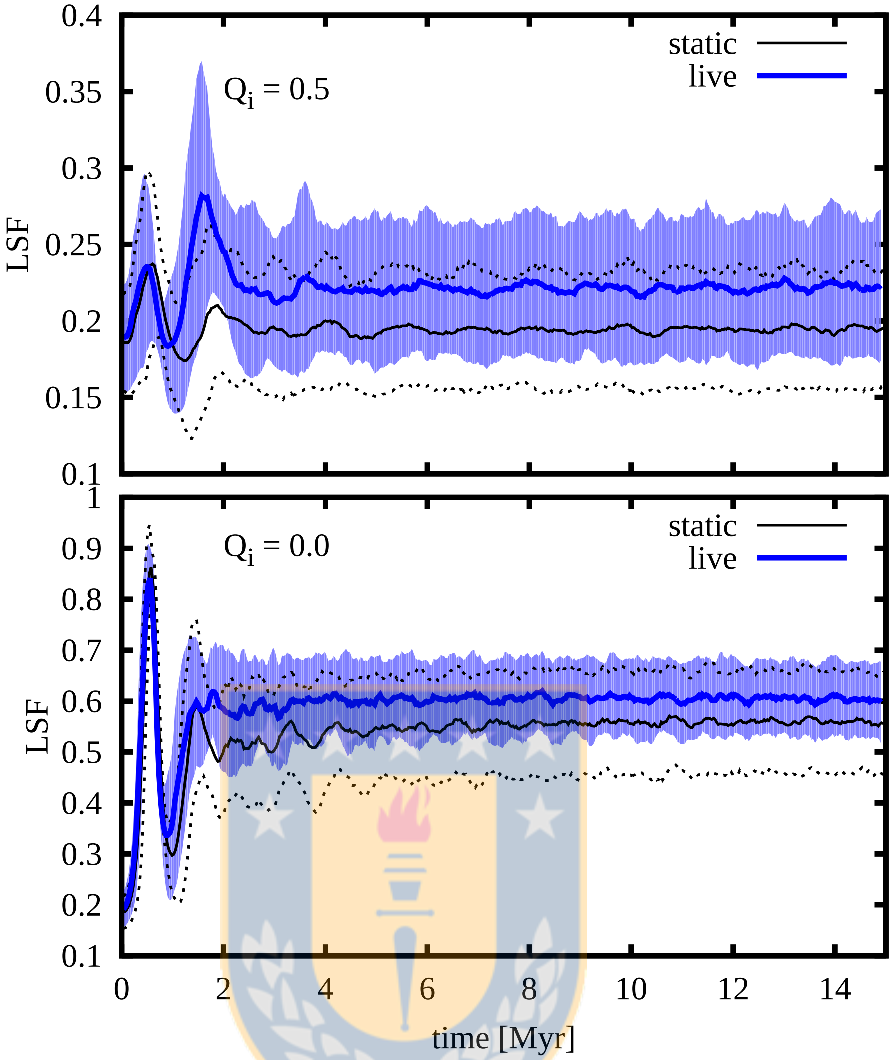

Figure 5.6: The evolution of the LSF. Blue solid lines with blue shadow areas show the mean amplitude of the LSF for the live gas simulations carried on this work with it standard deviation. Black line with dashed lines represent the mean amplitude the simulations utilizing a static background potential. As for all equal-mass particle simulations the LSF tends to a constant value which means there are no two-body relaxation effects.

km/s. Thus the interchange of momentum does not depend on the initial total angular momentum budget. No matter the initial conditions the gas will obtain more or less the same increase of angular momentum, most of it will come from the energy of the stars.

A big difference between simulations with live gas background and the static case comes from the interchange of energy between the stars and the gas. While in the static case stellar angular momentum is conserved, we have shown that the inclusion of a gas background is able to evolve results in a reduction of angular momentum of the same order no matter the initial conditions of the stars. This decrease of energy of the stars results in a decrease of the half mass radius of the stars. Since we have shown that the gaseous distribution remains quite stable especially with a low SFE, we conclude that the observed decrease in the half mass radius and therefore raise of the LSF originates only from the interchange of energy between the gaseous and stellar component.

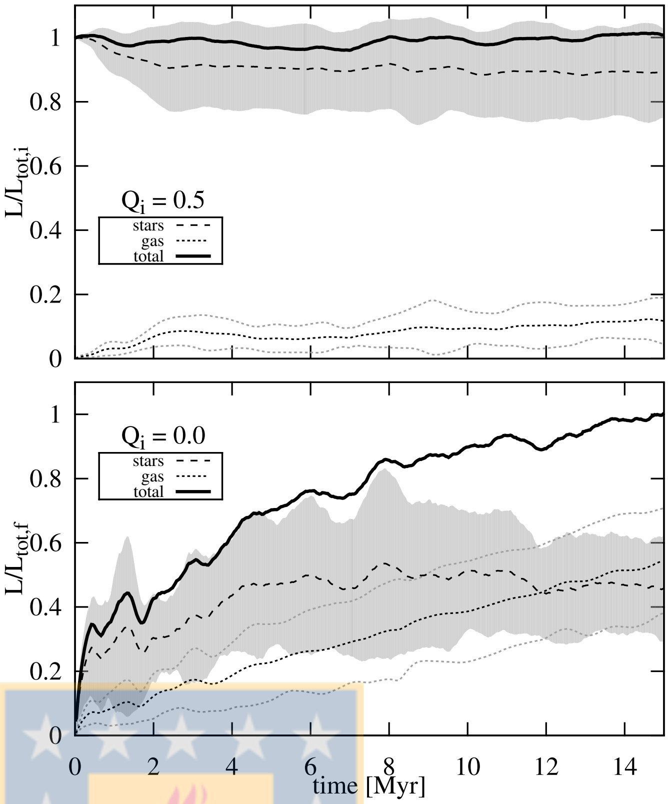

Figure 5.7: The angular momentum interchange between stars and gas. We measure the average evolution of the total angular momentum (solid line) and the contribution from the stars (dashed lines) and the gas (dotted lines) with gray shadows and dotted lines as the standard deviation for 20 fractals. Standard deviation for the total angular momentum is omitted for clarity. Top panel shows simulations with $Q_{\rm i} = 0.5$ with angular momentum values with respect to the initial total angular momentum. Bottom panel shows simulations with $Q_{\rm i} = 0.0$ and so, no initial angular momentum. Values are measured with respect to the final angular momentum instead.

5.4 Instantaneous Gas Expulsion

In this section we show the results of expelling the gas for the 20 previous fractals with the same initial velocities. Gas expulsion occurs when the virial ratio is exactly $Q_{\rm f} = 0.5$ and when in the virial ratio oscillation Q is increasing for the second time. The point when gas expulsion begins is when the cluster reach a value of Q raises for the second time and reaches $Q_{\rm f} = 0.5$ (right after the green dashed line of Fig. 4.1). We expel the gas this late to avoid the initial relaxation phase where substructure is still dominant, such scenario was already explored in the previous chapter and we will test gas expulsion in highly substructured gaseous and stellar distributions in the next chapter. For now we want to see if any difference exists when expelling the gas when stars evolve in a live gas background. To expel the gas instantaneously we increase the internal energy of the SPH particle nearest to the center. This energy is extremely high, to ensure that all the gas is gone after the explosion.

We derived a simple theoretical model with several very simple assumptions (see Sec. 4.4.2 and show that it works surprisingly well when predicting how much mass a cluster will retain when gas expulsion happens instantaneously. We have measured the bound mass fraction $f_{\rm bound}$ and find that this relation still holds with a live gas background as we show in the left panel of Fig. 5.8. However, becomes clear that the theoretical prediction overestimates $f_{\rm bound}$ at low LSF and underestimates it when LSF is high.

One important assumption in the analytical curve is that stars follows a Maxwell-Boltzmann velocity distribution. In the right panel of Fig. 5.8 we show the mean velocity distribution for the 20 fractals with $Q_{\rm i} = 0.5$ in a black pattern histogram and $Q_{\rm i} = 0.0$ in a blue solid histogram with omitted error bars for clarity. We have fitted a Maxwell-Boltzmann velocity distribution for each set. We can see that for the initially

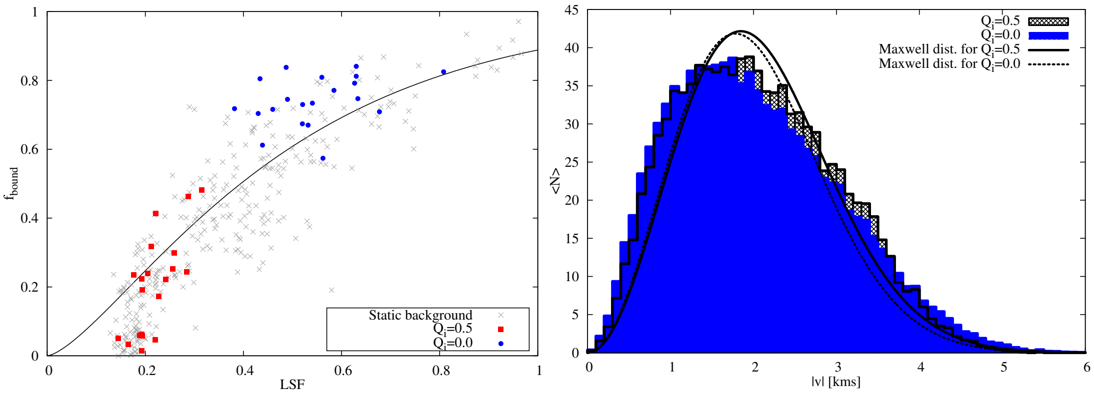

Figure 5.8: Survival rates to gas expulsion and a comparison with their velocity distributions. **Left:** Cluster survival to instantaneous gas expulsion with $Q_{\rm f} = 0.5$. Initially warm (red squares) and cold (blue circles) simulations expelling the gas when $Q = 0.5$ are shown. Gray crosses are all simulations with a static background gas of different shapes. Solid line represent the theoretical prediction introduced in Sec. 4.4.2. **Right:** Mean velocity distribution at the moment of gas expulsion for the 20 fractals. We see that initially cold simulations (blue solid histogram) follows a more stepper velocity distribution than a Maxwellian distribution (black dashed line). For the initially warm case (black pattern histogram) a Maxellian distribution (black solid line) of velocities is not such a bad assumption. Errorbars have been omitted for clarity

warm case a Maxwellian description is not such a bad assumption, however in the initially cold case, stars usually form a more steeper velocity distribution i.e. there are more stars with low velocities than in a Maxwellian description. For a given escape velocity $v_{\rm esc}$ there are more stars below $v_{\rm esc}$ and the cluster retain more mass than predicted. In contrast, when the LSF is low and the theory says that the cluster should retain only a small fraction of the total mass, the escape velocity drops considerably allowing more stars to escape, and thus, $f_{\rm bound}$ drops even more. This is not the case when the LSF is high, in this case the escape velocity does not change much and stars below the escape velocity stay bound.

Chapter 6

Gas Expulsion In Highly Substructured Gas Distributions

In the previous chapter we have seen that the inclusion of a live gas background to the static simulations performed in Chapter 4 does not change the relation between the LSF and f_{bound}. The only difference is the interchange of energy between stars and gas, where stars give some angular momentum to the initially static gas making the half mass radius to decrease which increase the LSF, however this change is not significant no matter the initial conditions of the cluster. The theoretical description introduced in Sec. 4.4.2 describe fairly well the observed results. However, the background gas is treated in a very simplistic way. The main point was to compare with the static Plummer background case, therefore gas was setup in a spherical and initially static distribution. In this chapter we explore gas expulsion in a more realistic scenario. Wide linewidths observed in molecular clouds suggest that molecular clouds are dominated by supersonic turbulent motions (Zuckerman and Evans, 1974). Such motions shapes the interstellar medium and star forming regions becomes substructured on all scales, i.e., it is possible to characterize these regions with a fractal dimension (Falgarone et al., 1991; Vogelaar and Wakker, 1994), very far from the spherical case explored so far in this work. We emulate these conditions by creating star formation simulations from an initial turbulent cloud of gas that ends up in a highly substructured stellar and gaseous distribution. We then expel the gas and measure how much mass the cluster can retain and we compare the results with the spherical case.

6.1 Setup

We perform star formation simulations with the purpose of recreate the substructure of the gas and a consequent stellar distribution, thus we are not interested in the microscopic details of star formation which are very computationally expensive and would exhaust all our recurses into one single simulation. Instead we perform several *cheaper* star formation simulations to obtain sufficient results to obtain statistics. We know from our previous studies, that working with substructured distributions results could change from one random realization to another.

6.1.1 Initial Conditions

We setup of a turbulent molecular cloud of $M_{\rm gas,i} = 2500$ M$_\odot$ distributed in an initially uniform sphere of $R_{\rm cl} = 1.5$ pc at a temperature of $T = 10$ K, that ends up in a $N_{\rm star} = 1000$ equal mass stellar distribution of $M_{\rm star} = 500$ M$_\odot$ embedded in a filamentary cloud of gas of $M_{\rm gas,f} = 2000$ M$_\odot$ matching a SFE= 0.2. This filamentary cloud of gas and star distribution is used as initial condition to then either evolve the cloud for some time with sensitive constraints to avoid further collapse or remove the gas just after the 1000 star particles form. We only create equal mass particles since the inclusion of an IMF is a problem that is been studied independently (Dominguez et. al. in preparation)

With this setup the initial mean Jeans mass of the cloud is $M_{\rm j} \approx 1$ M$_\odot$ which means that our cloud has ~ 2500 $M_{\rm j}$ that is more than enough to form 1000 equal mass particles. We use 250K SPH particles to perform our simulation, according to Bate et al. (2003) the minimum SPH particles needed to resolve fragmentation correctly is $1.5 N_{\rm smooth}$ per Jeans mass. The minimum Jeans mass that we are able to resolve with our setup is 0.75 M$_\odot$, however in our simulations we obtain densities above 10^9 M$_\odot$/pc^3 with local Jeans masses of ~ 0.0005 M$_\odot$. To properly resolve such densities in a cloud of the present size and mass, we would need 375 million SPH particles which is impossible to run with the computational resources at hand. However, in this work we are focused in the large scale substructure and we ignore this resolution problem for now since we are not interested in the local detail of fragmentation and star formation. In contrast, we are able to perform several cheap simulations instead of one single very expensive simulation.

6.1.2 Method

For the numerical treatment of the embedded star cluster, we split the simulation into four stages:

- **Collapse phase:** Which is the beginning of the simulation and ends when the star formation criterion for the first star meets.
- **Star formation phase:** In this stage all stars form and ends when enough stars form to match the desired SFE.
- **Embedded phase:** Is the stage where the collapse stops and evolution continues until the time we select for gas expulsion.

Table 6.1: Summary of the constraints used in this work to model young star clusters from their parent turbulent molecular cloud to the final gas free star cluster remnant. First column shows the physical stage modeled by the method, second column shows comments about the constraints related to the stellar component of the cluster, third row shows whether the Bridge integrator is enabled for the mutual interaction between gas and stars and fourth column shows comments about constraints and initial conditions related to the gaseous component such as the equation of state (EOS) used in the corresponding phase and the velocity field used as initial condition.

	Stars	Bridge interaction	**Gas**
Collapse phase	—	Off	EOS : **Isothermal** Initial velocity field: $P(k) \propto k^{-4}$
Star formation phase	1 star = N_{smooth} bound SPH particles	On	EOS: **Isothermal** If $h_{\text{i}} < h_{\text{crit}}$ then: check for star formation criterion
Embedded phase	1000 equal mass stars $m_{\text{star,i}} = 0.5$ M$_\odot$	On	EOS: **Isothermal** Self-gravity : Off EOS: **Adiabatic**, $\gamma = 5/3$ Self-gravity: On
Gas free phase	Evolution continues for 15 Myr	Off	—

- **Gas free phase:** The stage after gas expulsion where there are only stars in the cluster and evolving for 15 Myr when we stop the simulation.

We summarize this method in Table 6.1 and explain it in detail in this section.

In the *Collapse phase* gas is modeled using the hybrid Nbody/SPH code Fi with an isothermal equation of state to emulate the cooling of molecular clouds in a simple and cheap way. Such an approximation has been widely used in star formation simulations (Klessen et al., 1998; Klessen and Burkert, 2000; Heitsch et al., 2001; Li et al., 2003) to avoid the inclusion of radiative cooling recipes that are computationally expensive. We setup the initial velocity of the SPH particles creating an artificial turbulent velocity field in Fourier space with a energy power spectrum of $P(k) \propto k^{-\alpha}$ with $k = |\mathbf{k}|$ as the three dimensional wavenumber. A perturbation with a wavenumber k represent a velocity perturbation on scales $L = 2\pi/k$ i.e. small wavenumbers inserts energy on the large scales and high wavenumbers inserts energy perturbations on the small scales. To recreate observational substurctured star forming regions we choose a power law of $\alpha = 4$ so energy perturbations are distributed mainly on the large scales. We populate the k spectrum with integer wavenumbers from $k = 1 - 128$ then the Fourier space velocity perturbations are transformed to 3-D real space using the inverse Fourier transform that results a 3-D grid of $N_{\text{grid}} = 128^3$ cells as the velocity field. Then velocities of each SPH particle is linearly interpolated from the grid. The resulting turbulent velocity field is a combination of two extreme fields: the compressive forcing (curl-free) ; and the solenoidal forcing (divergence-free). On average a random field contains 2/3 in the solenoidal modes and 1/3 in the compressive modes (see Federrath et al., 2009, for details) different amount of energies in the different modes have strong consequences in the characteristics of the final distribution of the gas. In this work we setup the initial velocity field in the three extremes, pure compressive modes (curl-free), pure solenoidal modes (divergence-free) and random (mixed).

With an isothermal equation of state the gas collapses in different zones depending of the random seed that setup the initial velocity field. When the smoothing length of a SPH particle $h_{\rm i}$ is smaller than a critical radius $h_{\rm crit} = 0.0075$pc then the densest particle is selected and check if the $N_{\rm smooth} - 1$ nearest neighbours that are inside $h_{\rm i}$ are bound, if so the $N_{\rm smooth}$ selected SPH particles are combined into a star of $N_{\rm smooth} \times m_{\rm i}$ where $m_{\rm i}$ is the mass the individual SPH particle. We create only equal mass particles of $m_{*,\rm i} = 0.5$ $\rm M_\odot$ and choose $N_{\rm smooth} = 50$ for the simulation. The velocity of the new star is the mean velocity of the combined SPH particles. When at least 2 stars form the *Star formation phase* begins and we setup a Bridge scheme[1] in a similar way than in sec. 5.1, i.e., we follow the evolution of the stars with the direct Nbody integrator PH4, the gas continues being modelled in the same way than in the collapse phase and the gravitational interaction between stars and gas is done symmetrically with the Barnes and Hut (1986) tree scheme. We do not create sink particles, when a star forms, it only interact with its surroundings via gravity.

After we form 1000 equal mass particles, we choose either to continue evolving the gas or remove it at that point. Choosing to continue the evolution of the gas for more time is what we call the *embedded phase* and we stop the collapse of the cloud in two different ways. We turn off self gravity of the gas or we switch the equation of state of the gas to adiabatic with an adiabatic index $\gamma = 5/3$. In the first way, the gas disperses smoothly without significant dense regions. In the second way, the gas starts to form clumps that are supported by thermal pressure and starts to merge. We make simulations of both cases expelling the gas at 1 and 2 Myr after star formation stops. Hereafter we will refer to simulations with an adiabatic EOS for the gas as AEOS simulations, and simulations with the self gravity turned of for the gas as SGO simulations.

After gas expulsion happens, called the *gas free phase*, gas is not present anymore and we only follow the evolution of the stars using the code PH4 alone. We follow the evolution of the stars for 15 Myr after gas expulsion. At this point we measure the bound mass fraction of the biggest clump formed in the simulation using the Snowballing Method (see Chapter 3).

6.1.3 The $\mathcal{C}$ Parameter

We will measure the level of substructure in the young stellar cluster using the $\mathcal{C}$ parameter introduced by Cartwright and Whitworth (2004) (see also Cartwright, 2009)[2]. It is defined as the ratio between the mean length of a minimum spanning tree (MST) joining all the particles in the cluster, $\bar{m}$ and the average separation between stars in the cluster, $\bar{s}$:

$$\mathcal{C} = \frac{\bar{m}}{\bar{s}}. \tag{6.1}$$

To obtain a general description that does not depend either on the size or the number of particles in the cluster, the mean separation length is normalized by R_{cl} and the mean length of the MST is normalized by a factor $(NA)^{1/2}/(N-1)$ with A the area

---

[1] This is due only to a technical problem. A code like PH4 cannot calculate forces for only 1 particle. Before starting the Bridge scheme forces for the only present star are evaluated by the hybrid code FI in a tree scheme until another star is created

[2] Is actually called the $\mathcal{Q}$ parameter by the authors, however we call it $\mathcal{C}$ parameter in order to avoid confusion with the Virial ratio Q

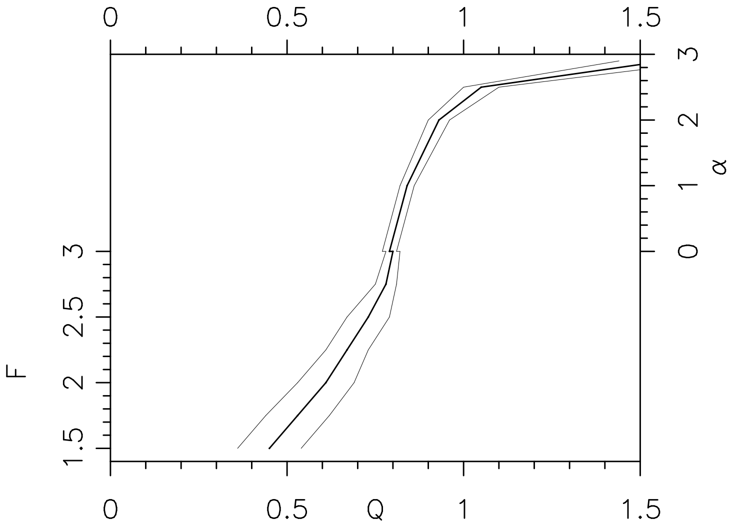

Figure 6.1: $\mathcal{C}$ parameter for artificial star clusters. From $\mathcal{C} \leq 0.8$ the fractal dimension D should be read from the left-hand axis, and for $\mathcal{C} \geq 0.8$ the radial density exponent α should be read from the right-hand axis. Figure taken from Cartwright and Whitworth (2004).

of the 2D projected cluster (see Cartwright and Whitworth, 2004, for details about the normalization). We measure a 2D projection of the cluster because of two reasons: It was shown by Cartwright (2009) that this parameter works better in 2D; Observationally, only a 2D projection is available, so we use a parameter that would be possible to measure in real star clusters. So we measure the $\mathcal{C}$ parameter in three canonical projections to take the mean and standard deviation as an error source.

One advantage of this parameter is that it not only quantifies substructure, it can also differentiate between a fractal distribution when $\mathcal{C} < 0.8$ where a lower value represent a higher level of substructure, and a spherical distributed cluster when $\mathcal{C} > 0.8$, where a higher value is a more centrally concentrated distribution. Fig. 6.1 shows the relation between the $\mathcal{C}$ parameter, the fractal dimension D and the power law of the density distribution α for a density distribution of the shape $\rho(r) \propto r^{-\alpha}$.

6.2 Improving the Model

Before analysing the results of the bound fractions in highly substructured embedded star clusters we need to make adaptations to the simple model introduced in sec. 4.4.2 in order to take into account the independent substructure of the gas and the stars. In terms of structure, even though stars are born into the structure of the gas, stars decouple very fast and form their our hierarchy. This happens because stars and gas respond to very different physical laws (Girichidis et al., 2012). We have shown that initially substructured clusters in a spherical background evolve into an equilibrium state given enough time. Stars rearrange into a spherical distribution with a scale length far smaller than the gaseous component (see Fig. 5.3). Considering that, it is quite surprising that the simple model of Chapter 4 worked that well, since an implicit assumption was assuming that the contribution to the potential energy from the gas and the stars is represented by the same expression.

Let's consider the potential energy just before ($\Omega_{*,1}$) and just after ($\Omega_{*,2}$) gas expulsion. We will denote quantities just before gas expulsion with subscript 1 and just after gas expulsion with subscript 2. Considering different spatial distribution we can write an estimation as:

$$\Omega_{*,1} = -A\frac{GM_*^2}{R_\mathrm{h}} + B\frac{GM_*M_\mathrm{gas}}{R_\mathrm{h}} \tag{6.2}$$

where we use the same scale radius in both contributions. In this work we choose R_h to be the half mass radius of the stellar cluster. A and B are structural parameters that depend of the distribution of the stars and the gas as well as the chosen scale radius R_h. A only depends on the stellar component while B is more complicated since it depends of how the stellar component is distributed with respect to the gas distribution. We will focus on these parameters in a later section. The LSF measure the relative amount of mass in stars relative to the total mass of the cluster inside the stellar half mass radius (see Eq.1.15). Therefore, an estimation of the total mass in the region where the stars are present is $M_\mathrm{gas} + M_* \sim M_*/\mathrm{LSF}$. From here we can obtain the amount of gas in this region as:

$$M_\mathrm{gas} \approx \frac{1-\mathrm{LSF}}{\mathrm{LSF}}M_* \tag{6.3}$$

After gas expulsion the potential energy of the cluster only depends of the stellar distribution. Considering instantaneous gas expulsion, stars have no time to change either their velocities or their positions. Thus the kinetic energy remains equal, i.e., $T_* = T_{*,1} = T_{*,2}$ and the structure parameter A remains the same.

The potential energy after gas expulsion is then:

$$\Omega_{*,2} = -A\frac{GM_*^2}{R_\mathrm{h}} \tag{6.4}$$

therefore we can rewrite Eq. 6.2 as:

$$\begin{aligned}\Omega_{*,1} &= \frac{\Omega_{*,2}}{A}\left[A + \frac{(1-\mathrm{LSF})}{\mathrm{LSF}}B\right] && (6.5)\\ &= \eta\Omega_{*,2} && (6.6)\end{aligned}$$

where we define :

$$\eta(\mathrm{LSF}, A, B) = 1 + \frac{(1-\mathrm{LSF})}{\mathrm{LSF}}\frac{B}{A} \tag{6.7}$$

The escape velocity after gas expulsion is:

$$v_\mathrm{esc} = \sqrt{-2\frac{\Omega_{*,2}}{M_*}} \tag{6.8}$$

Using the definition of the virial ratio and Eq. 6.6 :

$$\begin{aligned}Q_\mathrm{f} &= \frac{T_*}{-\Omega_{*,1}} && (6.9)\\ &= \frac{T_*}{-\eta\Omega_{*,2}} && (6.10)\end{aligned}$$

and assuming that the stars follow a Maxwellian velocity distribution, the kinetic energy of the stars can be written as:

$$T_* \;=\; \frac{3\kappa}{2} M_* \sigma_*^2 \tag{6.11}$$

where $\kappa = \pi/(3\pi - 8)$, we rewrite Eq. 6.8 as:

$$\begin{aligned} v_{\rm esc} &= \sqrt{\frac{2T_*}{\eta Q_{\rm f} M_*}} \qquad (6.12)\\ &= \sqrt{\frac{3\kappa}{\eta Q_{\rm f}}}\,\sigma_* \qquad (6.13) \end{aligned}$$

A reasonably first guess for the bound fraction would be the fraction of stars with velocities below the escape velocity. In a Maxwellian velocity distribution this fraction comes from the Cumulative Density Distribution (CDF) evaluated in $v = v_{\rm esc}$. With respect to σ_* this function is:

$$F(< X) \;=\; \mathrm{erf}\left(\frac{1}{2}X\right) - \sqrt{\frac{2}{\pi}}X \exp\left(-\frac{X^2}{2}\right) \tag{6.14}$$

where $X = v/\sqrt{\kappa}\sigma_*$. Evaluating in $v_{\rm esc}$ and using Eq. 6.13 we obtain:

$$f_{\rm bound} = \mathrm{erf}\left(\sqrt{\frac{3}{2\eta Q_{\rm f}}}\right) - \sqrt{\frac{6}{\pi\eta Q_{\rm f}}}\exp\left(-\frac{3}{2\eta Q_{\rm f}}\right) \tag{6.15}$$

Note, that when $B/A = 1$ then $\eta = 1/\mathrm{LSF}$ and Eq. 6.15 is then Eq. 4.8

6.2.1 The Structure Parameters

The structure parameters A and B are factors that account for the error in the estimation of the potential energy by the simple equation:

$$\Omega_{\rm est} = -M_* \frac{GM_{\rm source}}{R} \tag{6.16}$$

were $M_{\rm source}$ is the total mass of the system that provide the potential. We use the factor A when the potential energy comes only for the distribution itself, and B is used when the contribution for the total potential energy comes from an external field.

It is clear that Eq. 6.16 is only true for two point masses, however, it is the dimensional base for any analytical potential. We can take for example a stellar distribution that follows a Plummer sphere, in this case the "effective" potential energy is (see Heggie and Hut, 2003):

$$\begin{aligned} \Omega_{\rm eff} &= -\frac{3\pi}{32}\frac{GM_{\rm pl}^2}{R_{\rm pl}} \qquad (6.17)\\ &= -A\Omega_{\rm est} \qquad (6.18) \end{aligned}$$

where $M_{\rm pl}$ and $R_{\rm pl}$ are the Plummer mass and the Plummer radius respectively. Here the value of $A = 3\pi/32 = 0.29$, which is $\sim 30\%$ the estimated potential energy. Let's take the

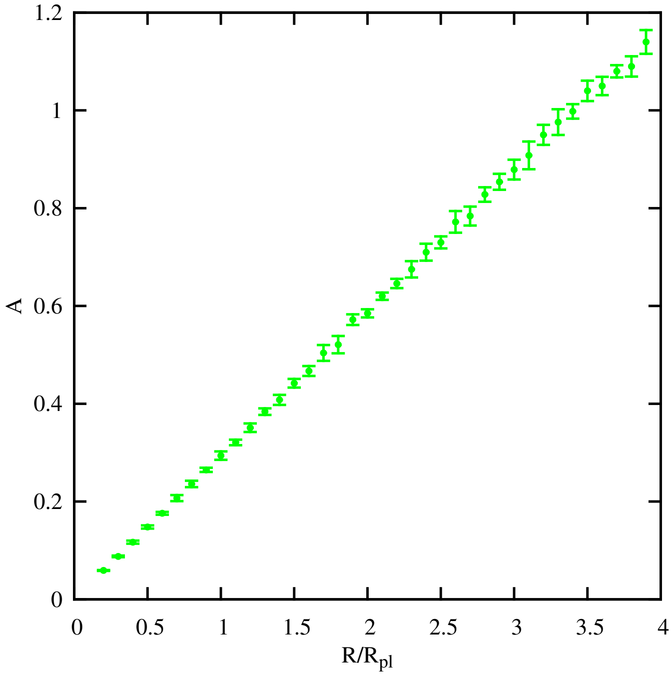

Figure 6.2: The dependence of A on the choice of the scale radius R for a Plummer distribution. We measure the A parameter for different sets of $N = 1000$ equal mass Plummer distributions varying the scale radius and taking the mean. We see the linear dependence on R for a Plummer sphere, however this correlation does not holds for a different distribution. But in general $A \propto R$.

other extreme as an example, a uniform sphere of particles would have a total potential energy of $3GM/5R$ (see Kittel et al., 1973, p268-269) which is 60% Ω_{est}. Considering these two examples the parameter A will be always < 1 when using a reasonable scale radius. However this parameter is also sensitive to the choice of this radius. If we increment the scale radius then Ω_{est} decreases, resulting in an increment of A, as we show on Fig. 6.2 for a Plummer distribution, thus $A \propto R$, i.e., a choice of a big scale radius (in comparison with the stellar distribution) could produce a scale factor $A > 1$. Another factor that would increase the value of A is substructure. Clumpiness also means that there are several stars that are very close to each other in comparison with the size of the cluster, a smaller distance between these stars will increment their contribution to the total potential energy since $A \propto \Omega_{\text{eff}}$.

The parameter A depends only on the characteristic structure of the stellar distribution, it is reasonable to think that a parameter quantifying substructure like the $\mathcal{C}$ parameter correlates with A. We construct different kinds of artificial clusters; Fractal clusters (Goodwin and Whitworth, 2004) with fractal dimensions D from 1.5 to 2.9; power law density distributions in the same way that Cartwright and Whitworth (2004) with power laws α between 0.2 and 2.8; King models (King, 1966) with concentration index $W_0 = \log(r_{\text{t}}/r_{\text{c}})$ between 1 and 16, r_{t} and r_{c} are the truncation radius and the core radius respectively; and a set of 20 Plummer spheres with different random seeds. Each distribution contains 1000 equal mass particles of 0.5 $\text{M}_{\odot}$ with a typical size of 1 pc. We measure the parameter A using several different scale radii. We find that the 40% percent mass radius R_{40} works best in collecting all the data into the same trend. The resulting correlation is shown in the left panel of Fig. 6.3 were a polynomial fit is shown as a black line.

We can see a clear correlation in the left panel of Fig. 6.3. However, our intention is not to provide a way to estimate the parameter A. Even though the distributions shown are constructed with equal mass particles, keep in in mind that the parameter A can also be heavily affected by the level of mass segregation present in the clusters (high mass segregation should result in an increase of A). However we will postpone this discussion

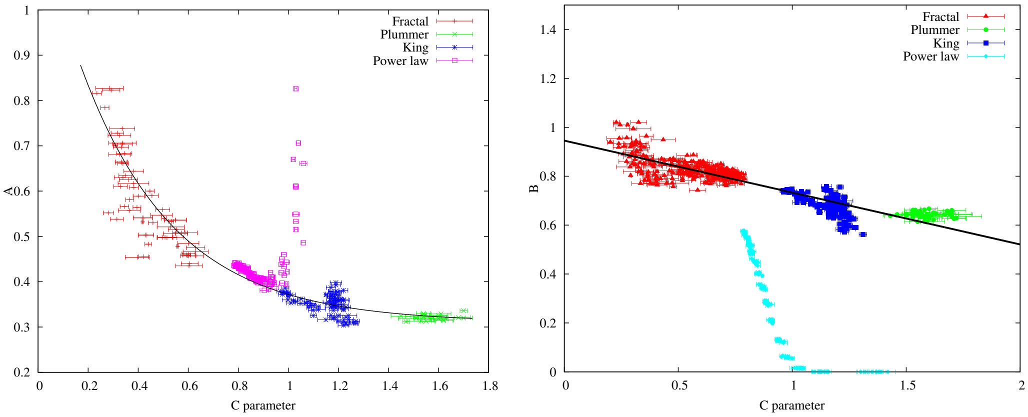

Figure 6.3: The structure parameters A (left) and B (right) for a set of different artificial equal mass distributions. Fractal clusters (red triangles), power law distribution (cyan diamonds); King models (blue squares) and Plummer spheres (green circles). The parameter B is measured with the same distributions embedded in a analytical Plummer potential of $M_{\rm pl} = 3472$ M$_{\odot}$ and $R_{\rm pl} = 1$ pc. Black solid lines are polynomial fits to the data as reference.

to a future project. The aim of this section is to better understand the nature of the parameters A and B.

The left panel of Fig. 6.3 illustrates the nature of the A parameter. In clumpy distributions, where stars are usually close to each other the value of $\Omega_{\rm eff}$ increases and so A. A power law distribution follow the same trend until it becomes too dense in the center. For power laws of $\alpha > 2.5$ the core is so populated that $\Omega_{\rm eff}$ increases significantly. Now the $\mathcal{C}$ parameters does not keep increasing because there are some stars away from the center that increase the value of $\bar{s}$ faster than $\bar{m}$ (see Sec. 6.1.3) because for one single star away from the center there is only one length connecting the star with the clump in the MST (one single contribution to $\bar{m}$) while there is $N - 1$ contribution to $\bar{s}$, hence distributions that have a very high contrast in densities show a “turn-over” in the $\mathcal{C}$ parameter. These densities also increase the value of A as shown in Fig. 6.3. The same turn-over is appreciated in the King models when $W_0 > 10$, however the A parameter does not increase so much since the central densities in the King models are not as extreme as in the power law distributions.

The structure parameter B depends of both, the source distribution and how the stellar population is distributed inside this potential. To analyse its behaviour we have embedded the distributions of the left panel of Fig. 6.3 in an analytical Plummer background potential and measure the B parameter that we show in the right panel of Fig.6.3. The nature of the Plummer potential is that it is weaker at smaller radii. This nature is expressed in the trend that we can see in the left panel of Fig. 6.3. Stellar distribution that are more extended (like the Fractal distributions) feel a bigger $\Omega_{\rm eff}$ that is also proportional to B. Distributions that are more concentrated in the center of the potential feel a weaker $\Omega_{\rm eff}$ and then B decreases (see the power law distributions on Fig. 6.3). This would be completely different if, in a extreme case, we would have the mass of the gas concentrated in the center. In this case the trend would be completely different, with the more concentrated distribution showing bigger B parameters than the open distributions. In general for any spherical potential the trend would be similar, the only difference would be how steep the trend would be. However in star formation regions and embedded star clusters a spherical potential is not the usual. We will keep

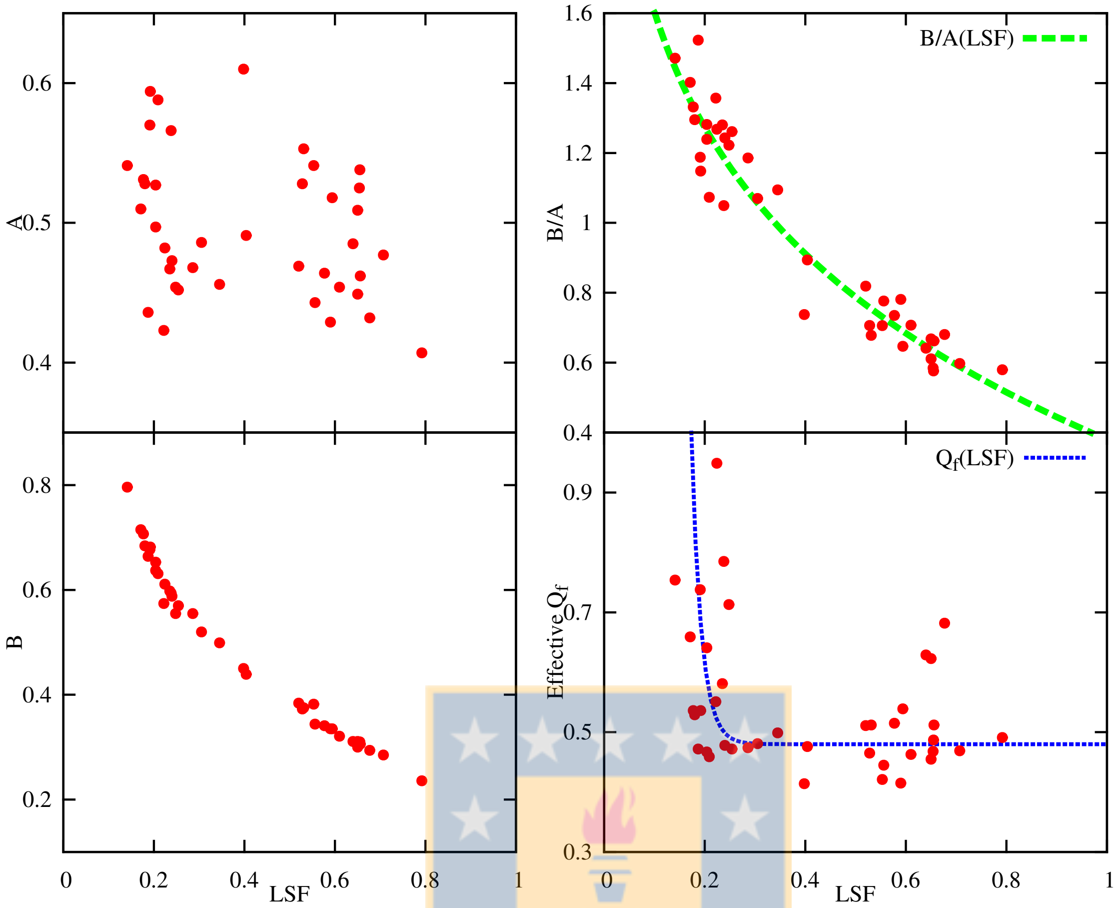

Figure 6.4: The structural parameters A and B measured for simulations with a live Plummer gas background. Left panels show the individual measure of A (top) and B (bottom). Right panels show the ratio B/A of the data (top) with a fitting function in a green dashed line, and the measure of the effective $Q_{\rm f}$ (bottom) with respect to the tracked bound clump (see main text) with a fitting function in the blue dotted line as reference. We see a clear difference between low and high LSF simulations. The strong correlation is because of the analytical background gas used in the simulations. This correlation could explain the difference between the $f_{\rm bound}$-LSF trend and the model introduced by Farias et al. (2015), however the disagreement with the model at low LSF can also be explained by the difference between $Q_{\rm f}$ and the effective $Q_{\rm f}$ that is usually higher.

the discussion of filamentary background structure for later sections when we analyse the outcome of our star forming simulations. First we will see how this analysis affects the case of spherical background gas and see if it does a better work explaining infant mortality in the stellar hierarchical scenario.

6.2.2 Testing the Model

In this section we will test our simple model described in the previous section using the characteristic trend of the Plummer Background case (see Sec. 5.4) as a reference. We saw in Sec. 5.4 that the simple model of Chapter 4 tends to heavily overestimate the $f_{\rm bound}$ at low LSF and underestimate it at high LSF. We will see now how this errors can be explained by the new model.

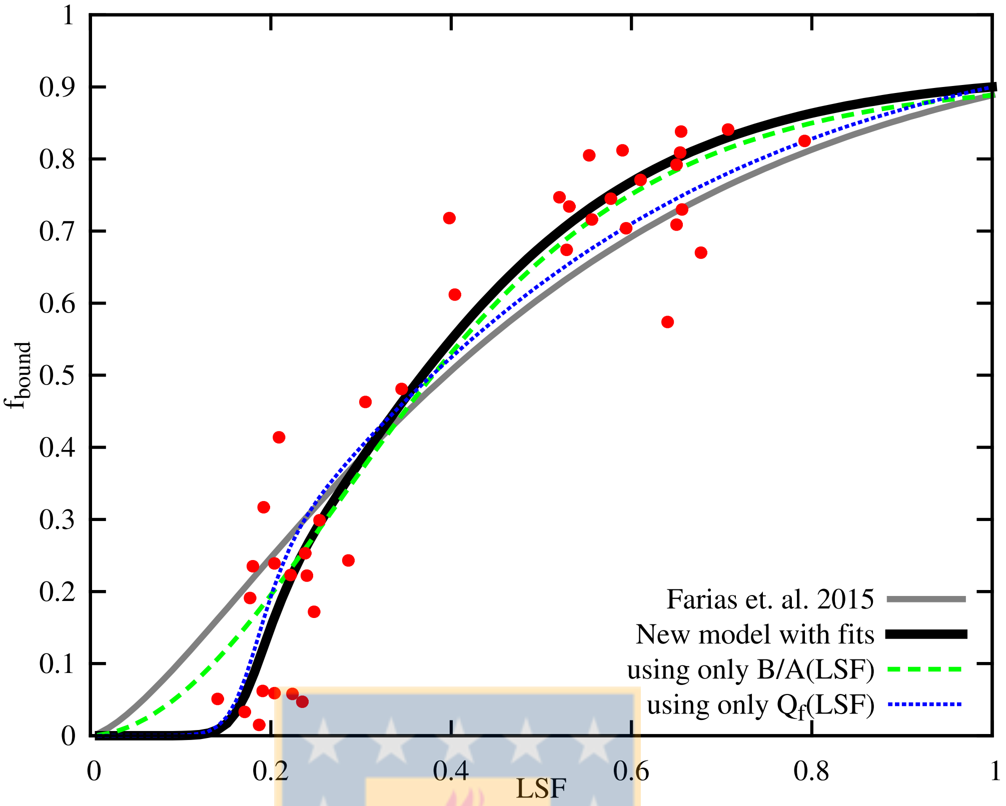

Figure 6.5: Testing the new model with simulations using a Plummer sphere of gas a background. Red circles show bound fractions from simulations using live gas background (see Chapter 5. Simple model introduced in sec. 4.4.2 is shown in a gray thin line, Thick black line shows Eq. 6.15 with fits to the data for the effective Q_f and the B/A ratio (see Fig. 6.4). The individual contributions of the fits are shown in a green dashed line for the B/A fit and in a blue dotted line for the effective Q_f fit. We can see that at high LSF disagreement between the gray line and the data is explained mostly by the B/A ratio, however at low LSF disagreement with the old model needs can not be explained only by the structural parameters, it also shows that the measure of Q_f is not representative for the bound clump.

First we measure the values of the structural parameters A and B numerically, measuring Ω_eff using the specific codes and smoothing lengths for each case in the same way that they were evolved and comparing them with Ω_est. We can see the resulting B/A ratio in the top right panel of Fig. 6.4 as a function of the LSF with a fit shown as green dashed line as a reference. We can see that there is a strong correlation between the B/A ratio and the LSF. However this trend is only because of the analytical background that we are using. We can see that the parameter A is similar for all the simulations with $A \sim 0.5$ and the parameter B is mainly responsible for the correlation in the right panel. At low LSF stars are not so concentrated in the center (otherwise the LSF would be higher) and so Ω_eff is stronger because of the nature of the Plummer background. The opposite happens at high LSF where stars are more concentrated in the center of the gas background where the potential is weaker and then B decreases.

As we said in Sec. 6.2 the model is equal to the one discussed in Chapter 4 if the ratio $B/A = 1$, top right panel of Fig. 6.4 shows two groups of points, the ones above $B/A = 1$ at low LSF, and the ones below $B/A = 1$ at high LSF. Note, that for the same value of Q_f it holds that $f_\mathrm{bound} \propto$ LSF, and since LSF $\propto 1/\eta$ and $\eta \propto B/A$ then $f_\mathrm{bound} \propto A/B$. In other words, $B/A > 1$ (low LSF) implies an even lower f_bound than in the old model and $B/A < 1$ (high LSF) results in a higher f_bound than the old model. This would be enough to explain the disagreement between the model of Chapter 4 and the simulations, however we will see that for the low LSF group this is not enough.

Even with this new model, we find that simulations with a small survival rate (usually small LSF) at the moment of gas expulsion loose more mass than predicted. We have found that this region (LSF< 0.25) is particularly difficult to model. A big problem is that since a small fraction of mass survives gas expulsion, this small bound cluster has its own velocity with respect to the star forming region as a whole. A critical step, when calculating Q_f, is the removal of the mean velocity of the cluster which does not necessarily represent the velocity of the clump that will finally remain bound. This is not a problem when f_bound is high (usually at high LSF). Here the mean velocity of the cluster is usually representative of the bound entity since a big fraction of the cluster will belong to the remaining clump.

To understand how much this problem would affect the measurement of Q_f we have tracked the bound clump back until the moment of gas expulsion, then we have measured again Q_f taking the zero velocity as the velocity of the bound clump at gas expulsion time. We have called this value the *effective* Q_f and the result is shown in the bottom right panel of Fig. 6.4 with a reference fit in a blue dotted line. We can see that at low LSF the value of the effective Q_f is substantially higher than 0.5, we remember that in this particular setup we have expelled the gas when the cluster had exactly $Q_\mathrm{f} = 0.5$ with respect to the center of mass. To see how much the measure of the effective Q_f and the ratio B/A reflects in the new model we have introduced the fits in the left panels of Fig. 6.4 into Eq. 6.15 and we show the resulting trend in Fig. 6.5.

At high LSF the data can be mostly explained by the structural parameters, however at low LSF this is not enough and even with a high B/A ratio the bound fractions are still overestimated (see green dashed line of Fig. 6.5). The only way of properly predict how much mass the cluster will retain when f_bound is low is to know the mean velocity of the clump that will survive at the moment of gas expulsion, i.e., knowing f_bound a priori. Simulations with a Plummer gas background suggest that a unpredictable regime emerges when $f_\mathrm{bound} \lesssim 0.3$.

6.3 Highly Substructured Clusters

In this section we analyse the distributions of the clusters obtained with the method described in section 6.1. Figure 6.6 shows four snapshots for each turbulent field used in this work. The three simulations showed in Fig. 6.6 are performed using the same random seed so we can see the difference caused by the type of turbulent field.

6.3.1 The New Initial Conditions

A random velocity field is a mixture of two independent velocity fields: a compressive (curl-free) field, a and a solenoidal (divergence-free) field (Federrath et al., 2009). In a divergence-free field velocities are oriented in a way that the cloud does not expand or contract as a whole. In this case the contraction of the cloud is only caused by the self gravity of the cloud in overdense regions. On the other hand the curl-free velocity field avoids the net rotation of the cloud, giving priority to either compressive

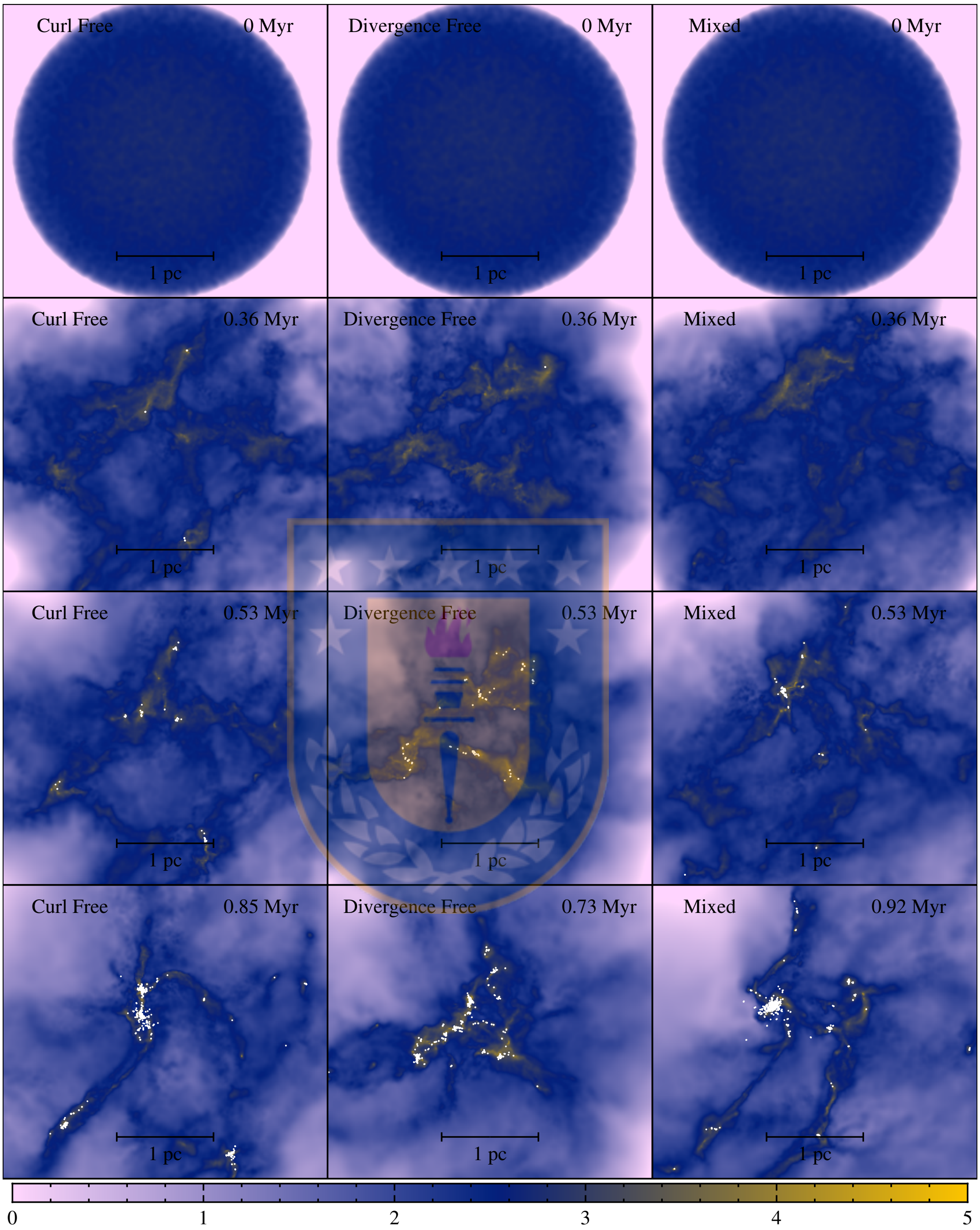

Figure 6.6: Evolution of the initially homogeneous turbulent molecular clouds until $N = 1000$ equal mass stars are formed. Simulations with curl-free (left column), divergence-free (middle column) and mixed (right column) turbulent fields are shown at (from top to bottom panels) 0 Myr, 0.36 Myr , 0.56 Myr and when 1000 stars are formed using the same random seed. Each panel has 3×3 pc^2 and the color bar represent the logarithmic column density measured in $\mathrm{M}_\odot/\mathrm{pc}^2$. This figure has been prepared with the SPLASH tool developed by Price (2011).

Table 6.2: A comparison between the initial conditions generated by the turbulent setup and simulations with fractal distributions embedded in a Plummer background. Values are means with respective standard deviations for each set of simulations described in column 1. Column 2 shows the initial half mass radius of the stellar distribution in parsecs, column 3 the initial local stellar fraction, column 4 the full radius containing all the stars in parsecs, column 5 the star formation efficiency measured at $R_{\max}$, column 6 the amount of primordial substructure measured by $\mathcal{C}$ parameter, column 7 the initial virial ratio and column 8 the velocity dispersion of the stellar component.

	$R_{\rm h}$[pc]	LSF	$R_{\max}$[pc]	SFE$_{R_{\max}}$	$\mathcal{C}$	$Q_{\rm i}$	σ_*[km/s]
Plummer Background							
Cold	0.9 ± 0.1	0.19 ± 0.03	1.5	0.2	0.39 ± 0.06	0.0	0
Warm	0.9 ± 0.1	0.19 ± 0.03	1.5	0.2	0.39 ± 0.06	0.5	1.0 ± 0.1
Turbulent Setup							
Div. Free	0.5 ± 0.3	0.6 ± 0.2	2.5 ± 0.9	0.24 ± 0.03	0.28 ± 0.07	0.31 ± 0.06	1.1 ± 0.2
Curl Free	0.6 ± 0.4	0.5 ± 0.2	2.5 ± 0.9	0.23 ± 0.03	0.24 ± 0.08	0.27 ± 0.06	0.9 ± 0.2
Mixed	0.4 ± 0.3	0.6 ± 0.2	2.7 ± 0.9	0.23 ± 0.02	0.27 ± 0.08	0.31 ± 0.07	1.1 ± 0.2

or expansive velocities. In terms of substructure, what we can see for example in Fig. 6.6 and also in Figure 1 of Federrath et al. (2009) is that the curl-free part of a velocity field is mostly responsible for most of the filamentary structure in star forming regions, while in divergence-free fields star formation seems to happen in a more "uniform" way. Regardless these differences in the turbulent modes, there is no significant difference in the final stellar distribution in our star formation simulations. Table 6.2 summarizes some important parameters in the three kinds of turbulence used in this work, together with a comparison of initial conditions used in Chap. 5 which are exactly like the simulations performed in Chapter 4.

The similarity of global parameters regardless the field type is in agreement with Girichidis et al. (2012) and Lomax et al. (2015) where the same turbulent modes have been tested on star formation on smaller clouds of < 100 M$_\odot$ in mass and < 0.1 parsec in radii that form < 500 low mass stars. The differences they found are significant in the amount of high mass stars relative to low mass stars , and the kinds of fragmentation of the clouds (Lomax et al., 2015) however both cases are not relevant to this work since we force the formation of equal mass particles and our resolution is not enough to distinguish the different kind of fragmentation. In terms of substructure Girichidis et al. (2012) showed that in general curl-free modes of turbulence form slightly more substructured clusters than divergence-free modes, i.e., $\mathcal{C}_{\rm comp} \lesssim \mathcal{C}_{\rm mix} \lesssim \mathcal{C}_{\rm sol}$ which agrees with our results. However, statistically, these differences are not significant in our simulations. Girichidis et al. (2012) conclude that these similarities between stellar distributions formed in different turbulent modes are because the newborn stars quickly decouple from its parent cloud dynamically, and N-body interactions dominate the motion of the stellar cluster. The continuous formation of stars with sub-virial velocities lead to a global sub-virial state which is in agreement with our simulations.

In comparison with to initial conditions of Chapter 4 we now form clusters with 2.5 pc radius and a SFE of a $\sim 24\%$, slightly higher than the setup SFE of 20% since there is always some gas outside of $R_{\max}$. We obtain distributions with lower $\mathcal{C}$ parameters ,i.e. with the turbulent setup we obtain higher substructured clusters than the $D = 1.6$ stellar distributions used in the Plummer background case. However, the new distributions show a higher initial LSF, this is a consequence of the shape of the background gas that is not concentrated in the center like a Plummer sphere, instead it is generally concentrated in a filamentary structure around the center of mass of the cloud. Furthermore, the half mass radius in the turbulent setup is smaller which means that we obtain a more centrally concentrated cluster in comparison with the fractal method described by Cartwright and Whitworth (2004).

Velocity dispersions in the turbulent setup are almost identical to the ones in the warm Plummer background case with $\sigma_* \approx 1$ km/s. Considering that the $Q_\mathrm{f} \approx 0.3$ for the stars in the turbulent cloud and the distributions are globally more extended than the Plummer background case, this already tells us something about the gravitational potential that the stars feel in a filamentary star formation scenario. Since the distributions are more extended, it is reasonable to think that the potential energy, felt by the stars, should decrease. However, Table 6.2 shows the opposite: the potential energy in a filamentary gas needs to be higher so σ_* (and in consequence the kinetic energy) remains equal for a low value of Q_f. This increase is because in the turbulent setup, even though gas and stars decouple, stars are quite near to the densest regions of the cloud, this would increase the potential energy of the stars decreasing the value of Q_f.

6.3.2 The Embedded Evolution

As described in Sec. 6.1 we use the distributions described in the previous section to perform simulations of the further evolution of the cluster in the embedded phase until we decide to expel the gas instantaneously. This evolution is chosen to be either with an adiabatic equation of state for the gas (AEOS simulations) or with self gravity of the gas turned off (SGO simulations).

Fig. 6.7 shows several parameters for both AEOS and SGO sets of simulations. Different line types show the different velocity field type from which stars were born, with dashed lines for the curl-free field, dot dashed lines for the divergence-free field and mixed velocity field is shown as a solid line. The evolution of the spatial distributions for the gas and the stars are shown in Fig. 6.8 and 6.9 where each set of 6 panels show the evolution of the cluster under the two setups, self-gravity turned off (top panels) and the adiabatic EOS (bottom panels) at three points of the evolution: the beginning of the embedded phase (left panels), after 1 Myr (middle panels) and at 2 Myr of evolution (right panels). These points of the evolution also represent the points were we have expelled the gas that we will analyse in the next section.

We can see the difference in the evolution of the half mass radius in the first panel of Fig: 6.7 where simulations with a curl-free velocity field born with a more extended stellar distribution than the other two field types. Later evolution depends of the treatment of the gas.

An adiabatic EOS for the gas causes the initially filamentary gas to rearrange in small clumps that eventually merge into bigger clumps as we can see in the bottom panels of Figs. 6.8 and 6.9 these gaseous clumps are strong enough to attract nearby stellar clumps so stars and gas couple again merging into a bigger clump. Eventually we would obtain a similar situation than in Chapter 5, however 2 Myr is not enough to erase all the primordial substructure. How fast substructure is erased will depend of how extended the initial distribution is, this is confirmed by the $\mathcal{C}$ parameter (last panel of Fig. 6.7) that show how clusters born in a curl-free velocity field (usually more extended) take more time to erase primordial substructure that is also higher for curl-free simulations.

In the case of SGO simulations, the gas is dispersed by the initial velocity of the gas and it is only attracted by the gravity of the stars. This is not enough to retain the fast

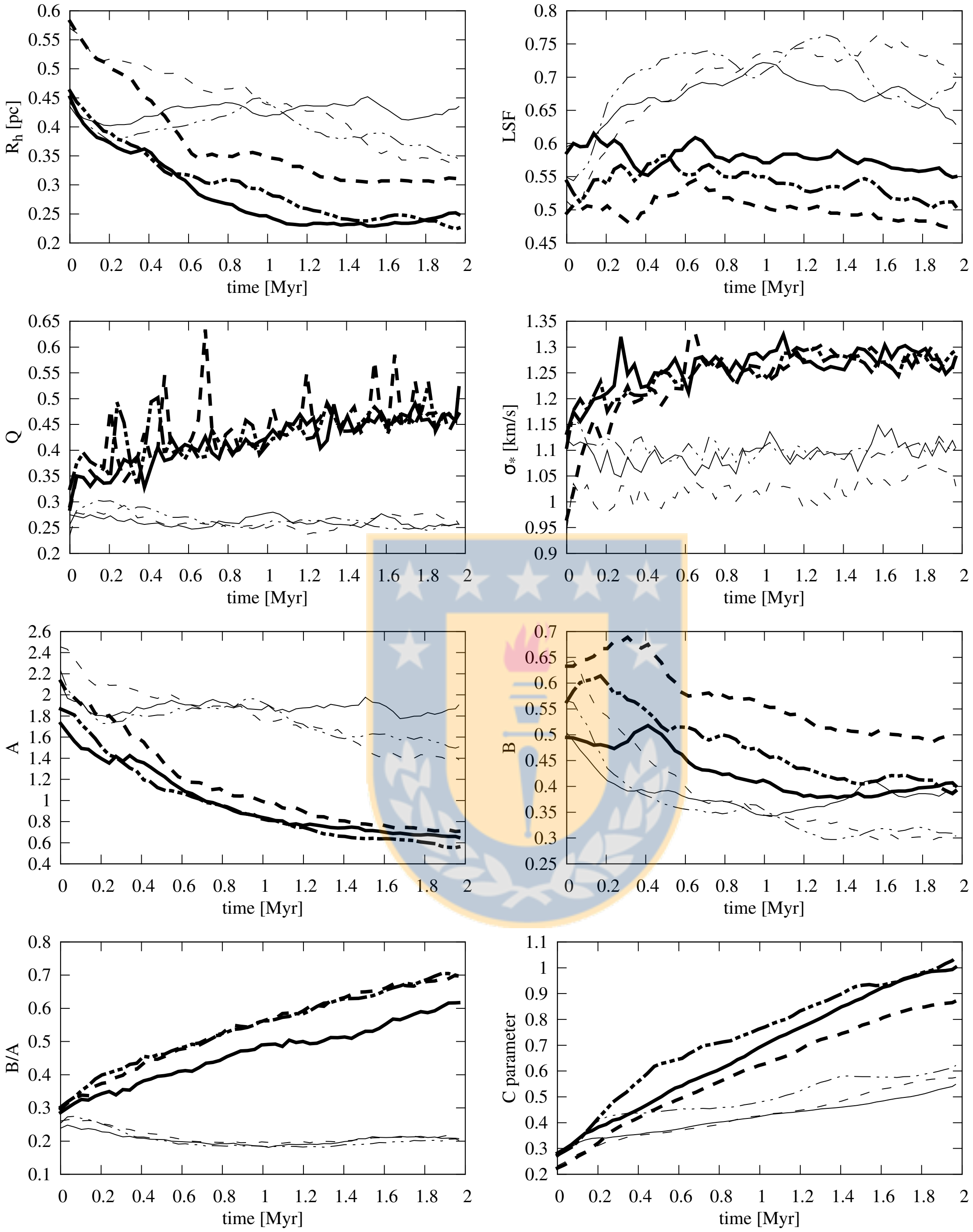

Figure 6.7: The evolution of the embedded star clusters for 2 Myr after the $N = 1000$ stars form. Values are means for each parameter of the 10 realizations for each setup where standard deviations have been omitted for clarity. From top to bottom: The stellar half mass radius R_{h}, the Local Stellar Fraction, the virial ratio Q, the stellar velocity dispersion σ_*, the structure parameters A and B, the B/A ratio and the $\mathcal{C}$ parameter. Thick lines are AEOS simulations and thin lines are SGO simulations. In both cases divergence free setup is shown in a dot dashed line, curl-free in a dashed line and mixed setup in solid lines.

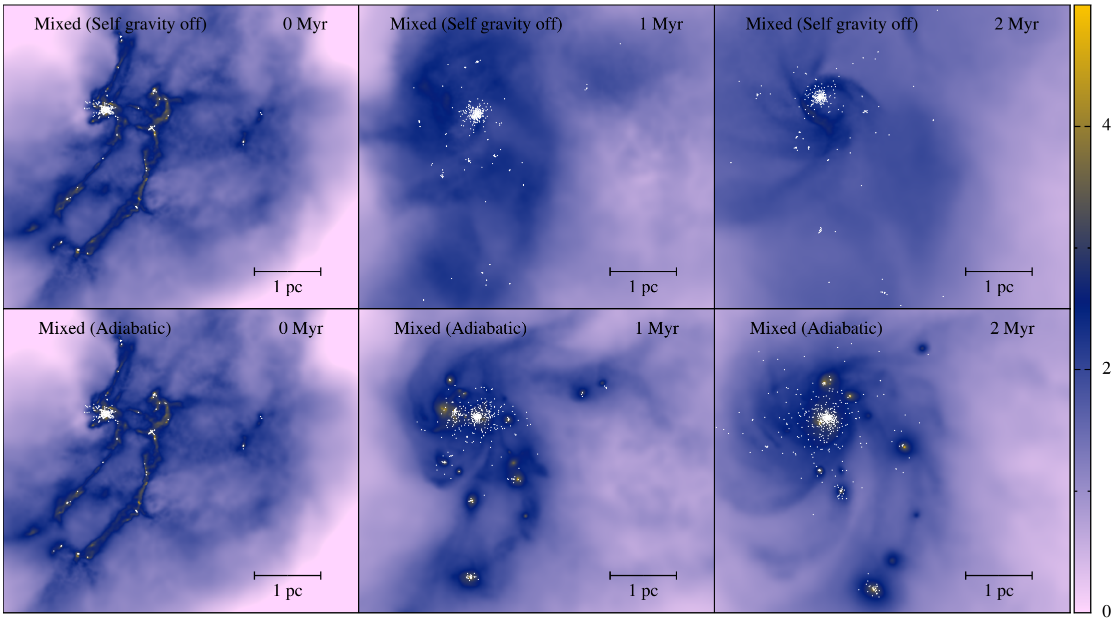

Figure 6.8: Snapshot of a embedded star cluster with a mixed initial velocity field at the times when gas is expelled. top panels shows the evolution of the cluster when self-gravity of the gas is turned off where each panel shows the evolution of the panel before, bottom panels show the same distribution under an adiabatic EOS for the gas. Colors represent the Log column density in $M_\odot/pc^2$. Image has been prepared with the SPLASH tool developed by Price (2011)

gas particles. R_h stays higher than in the adiabatic case since the background potential is weaker. For the same reason the LSF raises to values above 60%. Substructure also remains higher, which we can see in the evolution of the $\mathcal{C}$ parameter. Even after 2 Myr of embedded evolution clusters without self-gravity for the gas never leave the "clumpy" regime ($\mathcal{C} < 0.8$).

The difference in the substructure of the stars and the concentration of the gas in both cases have critical consequences in the values of the structural parameters A and B (see Fig. 6.7). The parameter A, which only depends on the stars, shows a strong decrease in the adiabatic case in contrast with the small decrease the simulations with no self-gravity for the gas. As discussed in Sec. 6.2.1 the parameter A increments with substructure which explains the high decrease in the adiabatic case (where substructure is erased efficiently) in comparison with the case without self-gravity. The evolution of the parameter B shows that in both cases the effective potential energy decreases. The parameter B is also proportional to substructure so it decreases with time as substructure is erased. However, we can see that the big change in the structure parameters originates mainly from the stellar component, i.e., the parameter A. This change causes that the B/A ratio split very clearly the two scenarios with low B/A ratios for simulations with no gaseous self-gravity and high values for the adiabatic simulations. These low values of B/A predict a higher survival rate than the model of Sec. 4.4.2 can predict. We will analyse the survival rates in the next section.

The rate at which substructure is erased also affects the dynamical state of the cluster. In the adiabatic case where substructure is erased quickly, the cluster reaches virial equilibrium faster than the case without self-gravity. When the background potential is weaker, the merging of clumps is supressed and the relative low velocities between

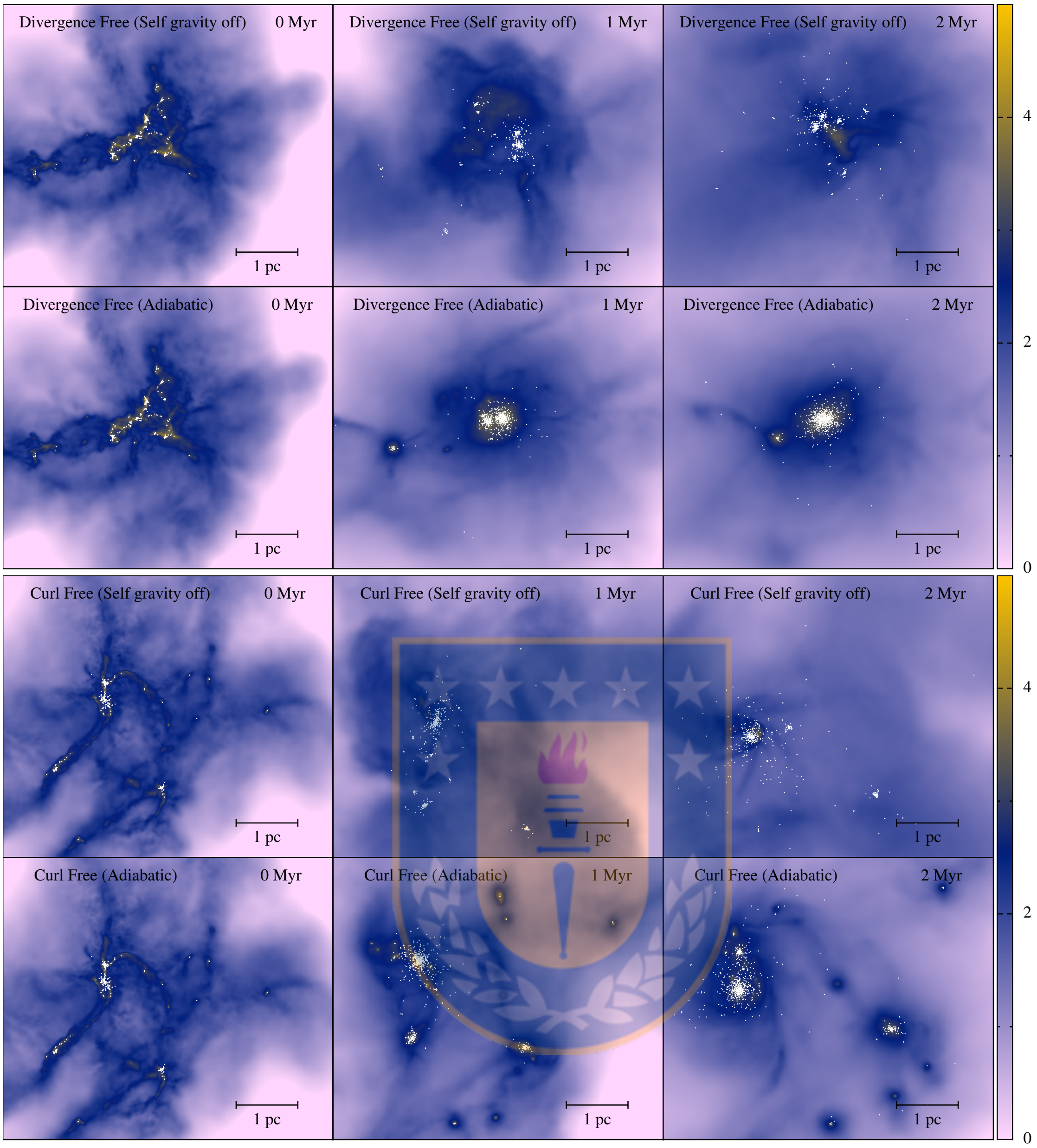

Figure 6.9: Same as Fig. 6.8 for an initial divergence free (top panels) and curl-free (bottom panels) velocity fields.

each clump remain the same for a longer time. A merging results in several two body encounters that raise the kinetic energy (and hence the velocity dispersion), increasing the value of Q. In the SGO case this doesn't happen and velocities remain similar during the 2 Myr that we have follow the evolution as we can see in the values of the velocity dispersion in Fig. 6.7.

6.3.3 Survival to Gas Expulsion

After following the evolution of the embedded star clusters with two extremes treatments for the background gas, we expel the gas instantaneously at 0, 1 and 2 Myr after 1000 stars have formed in the star formation phase. Then we measured the fraction of bound stars at 15 Myr after the moment of gas expulsion.

We can see in Fig. 6.10 the results of the measurements of $f_{\rm bound}$ together with the estimations from the model presented in Sec. 6.2 as errorbars and the estimations of the model introduced in Chapter 4 as crosses for the two different treatments of the background gas. SGO simulations are shown in the left panels and AEOS simulations are shown in the right panels for the different moments of gas expulsion.

The high survival rates of the simulations expelling the gas at 0 Myr and SGO that are explained mainly by the low $Q_{\rm f}$ and B/A ratios (see Fig. 6.7). Both parameters keep low in SGO simulations in contrast with the AEOS simulations where both parameters increase with time. In SGO simulations the LSF does not help to estimate $f_{\rm bound}$ and bound fractions are mainly estimated by $Q_{\rm f}$. Considering substructure into the models does not always increment accuracy as we can see some crosses inside the errorbars in Fig. 6.10, however we will see later that in general it does a better job.

For AEOS simulations a similar trend to simulations with a Plummer Background potential (see left panel of Fig. 5.8) raises. This is because in general this simulations tend to erase substructure, i.e., the ratio B/A increases to values near 1 and at the same time the embedded star cluster quickly reaches equilibrium (Q evolves to 0.5) in contrast with the SGO simulations were Q remains low for long times (see Fig. 6.7).

A closer look to the crosses and the errorbars in Fig. 6.10 show that the model with substructure does, in general, a better job when substructure is high. However everything seems to be fairly well explained when measuring the effective $Q_{\rm f}$ (see Sec. 6.2.2) and considerations of substructure does not improve the predictions significantly. Hence we have to quantify how well the models represent the results from all the simulations in this work.

Fig. 6.11 shows the differences between the analytical models, i.e. our analytical predictions, with the different considerations and the measured bound fractions for all the simulations performed with a live gas background (including Chapter 5 simulations). We measure the standard deviation (σ) from the analytical model considering four cases: Models not considering substructure, i.e., assuming $B/A = 1$ (top panels); models considering substructure through the numerical measurement of the structure parameters A and B (bottom panels): Models where the value of $Q_{\rm f}$ is measured considering the mean velocity of the whole cluster, i.e., the global $Q_{\rm f}$ (left panels); and models where $Q_{\rm f}$ is measured by knowing the mean velocity of the clump that finally survives gas expulsion a priori, i.e., the effective $Q_{\rm f}$ (right panels). We can see no changes when considering the global $Q_{\rm f}$ or the effective $Q_{\rm f}$, i.e., shaded areas in the top panels are the same than in the bottom panels, this is because, in general, we obtain high bound fractions for all the simulations with a live gas background, with the exception of a small group of low LSF simulations in Chapter 5 that have not affected the results. Considering the structural parameters only improves our model on a 1% level as we can see by comparing the left panels with the right panels of Fig. 6.11. But this is only true for simulations with $f_{\rm bound} \gtrsim 0.3$.

Including or not the structural parameters we can see that all the simulations performed utilizing a live gas background, even the simulations where gas expulsion happens at the beginning of the embedded phase when gas and stars are highly substructured, we can estimate the bound fractions with a $\sim 10\%$ of uncertainly. This results shows that

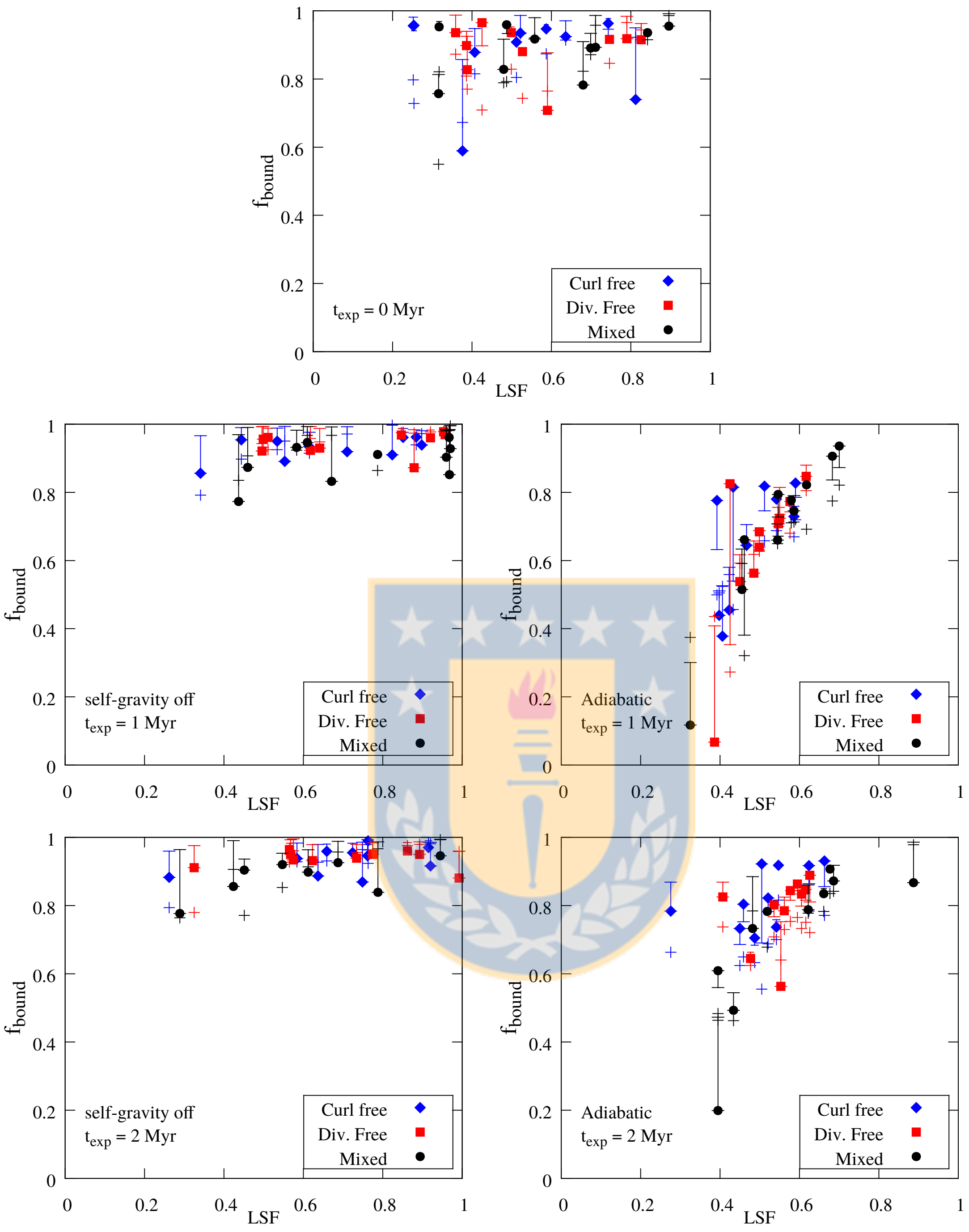

Figure 6.10: Bound fractions for embedded star clusters at 15 Myr the moment of gas expulsion. Different panels show sets of simulations expelling the gas at 0 Myr (top panel), 1 Myr (middle panels) and 2 Myr (bottom) after the end of the star formation phase. Panels at the left are the results from SGO simulations and right panels show the resulting bound fractions from AEOS simulations. The different natal velocity fields are shown as different symbols with curl-free velocity fields in blue diamonds, divergence free fields in red squared and the mixture of both in black circles. Errorbars show the prediction of the model presented in this work taking in account the substructure of the gas and the stars through the parameters A and B. Crosses are the predictions of the model without considering substructure as described in (Farias et al., 2015), i.e., assuming $B/A = 1$. All model predictions are calculated using the effective $Q_{\rm f}$ discussed in Sec. 6.2.2.

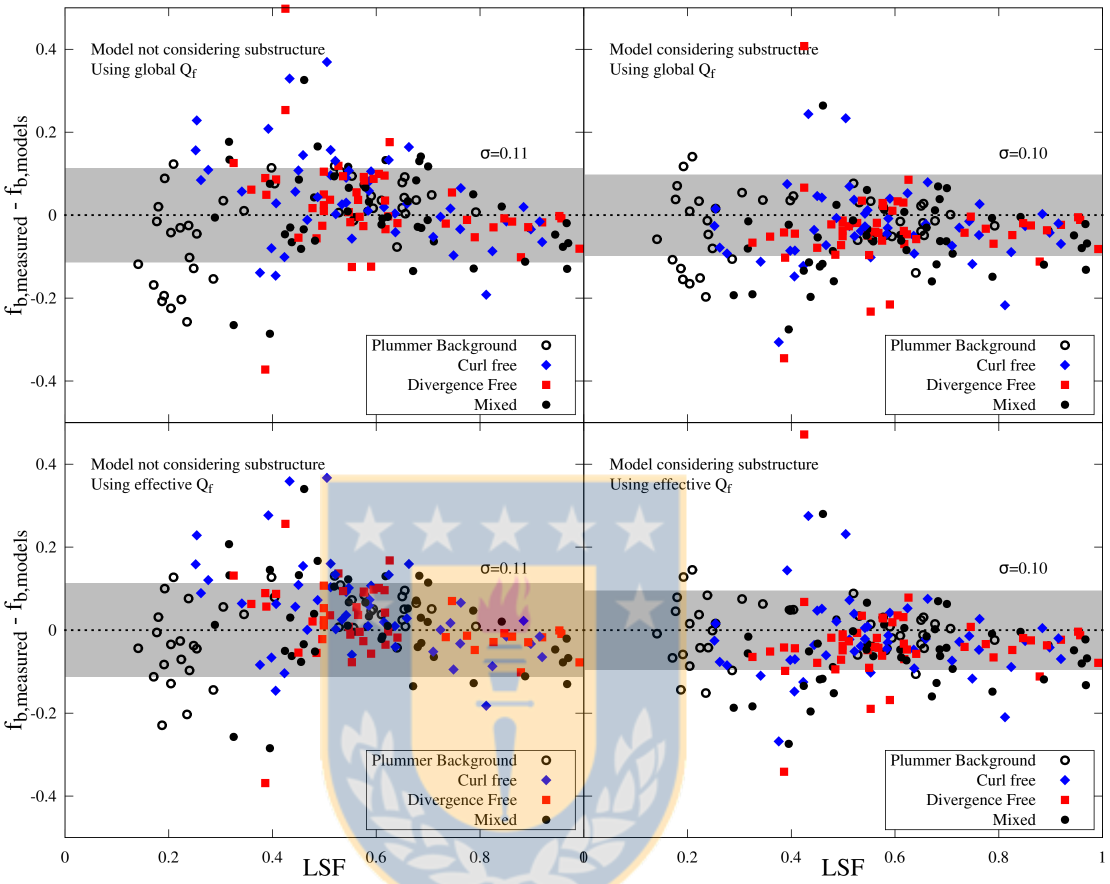

Figure 6.11: The differences between the analytic models and the measured bound fractions for all the simulations performed with a dynamically live gas background. Top panels show the performance of the models when measuring Q_{f} with respect to the global mean velocity while bottom panels show the performance of the models when measuring the effective Q_{f} i.e. when using the mean velocity of the clump that remains bound after gas expulsion (see Sec. 6.2.2). Left panels show the behaviour of the models when we do not take into account structure parameters (assuming $B/A = 1$) and right panels shows results when substructure is included through the measure of the parameters A and B. Different natal velocity fields are shown in the same way than in Fig. 6.10 and simulations with a Plummer background gas (see Fig. 5.8) are shown as black open circles. We show the performance of the models through the standard deviation from the models represented by the gray shaded areas. We can see that the consideration of the effective Q_{f} does not change the performance (due to the generally big f_{bound} obtained in this work) and the consideration of substructure only improves the accuracy of the models on a 1% level. We can see that we can predict the outcome of all the simulations on this work with a 10% of uncertainly even in cases of high levels of substructure in the gas and stars.

the inclusion of an arbitrary distribution for the gas and the stars does not result in an unpredictable scenario, in fact this results suggests that it is possible to predict how much mass a cluster can retain in any distribution if it is possible to measure at least the virial ratio and the LSF without caring for the presence of substructure. However, we must keep in mind that we test these models in equal mass stellar distributions. Inclusion of an initial mass function could alter the results depending of the level of mass segregation at the moment of gas expulsion since we don't know how much it will affect the values of the structure parameters that we have shown are not very important but we haven't reached extremes values yet that could be possible with massive stars. How much an IMF will affect the results is a question that we will explore in a future work.

6.4 Limitations of the Model

Analysing our analytical model, we note that there is a simple way to distinguish if the model described in Sec. 6.2 is well defined or not. Let's consider the virial ratio just after the gas is expelled ($Q_{\rm a}$). We assume that the kinetic energy before gas expulsion is the same that the kinetic energy after gas expulsion. The only thing that changes is the potential felt by the stars. Thus we have that:

$$Q_{\rm a} = \frac{T_*}{\Omega_{*,2}}. \tag{6.19}$$

Using Eq. 6.10 we obtain:

$$\frac{Q_{\rm a}}{Q_{\rm f}} = \eta. \tag{6.20}$$

Thus, according to our model it is possible to estimate the value of η by measuring the virial ratio before and after the gas is expelled, i.e., measuring the virial ratio ignoring the presence of the gas. If our model is correct Then measuring $Q_{\rm f}$ and $Q_{\rm a}$ would give us an easy method to deduce η or vice-versa determining η would give us a measure for the virial ratios before and after gas-expulsion. However, we need to be aware that our model is based on several assumptions and we need to know the limits where those assumptions aren't too bad. Fig. 6.12 shows the ratio $Q_{\rm a}/Q_{\rm f}$ against the measured value of η with different symbols for the different sets of simulations utilizing a dynamically live gas background[1]. Colors represent the level of stellar substructure, at the time of gas expulsion, measured by the $\mathcal{C}$ parameter, i.e.: no stellar substructure in green to dark-green ($\mathcal{C} > 0.8$), clumpy stellar distributions in red to yellow ($\mathcal{C} < 0.8$). We show in a black solid line what our analytical model expects, i.e. Eq. 6.20.

We see that simulations with a Plummer background (open circles) seem to follow a different trend (black dashed line). The same trend seems to be followed by any simulation where substructure in the stellar component is erased (green symbols). We cannot tell if at high values of η the trend is the same than in the Plummer background simulations since we haven't obtained high values of η for simulations with gas substructure. But at least if $\eta < 4$ our analytical model seems to work quite well for most of the simulations.

---

[1] Note that what we choose as a zero mean velocity to calculate the ratio $Q_{\rm a}/Q_{\rm f}$ is not important (as long as we are consistent) since the kinetic energy is the same in both values. Thus the ratio $Q_{\rm a}/Q_{\rm f}$ only depends on the spatial distribution of the gas and the stars as well as η.

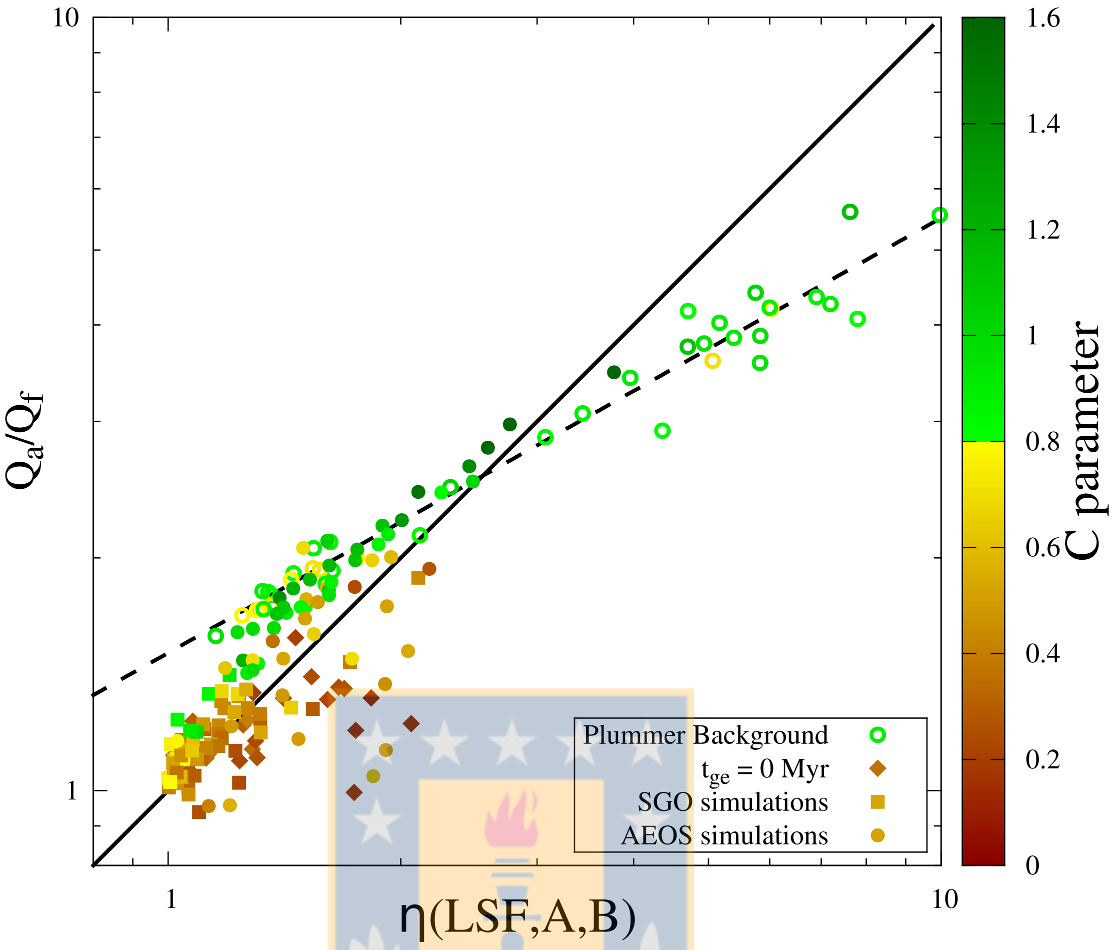

Figure 6.12: Estimation of the value of η through the measure of $Q_{\rm a}/Q_{\rm f}$ ratio. Symbols represent the different setups used in this setup: Simulations with a Plummer background potential are shown in open circles, simulations where gas is expelled at $t_{\rm ge} = 0 Myr$ (no embedded phase) are shown in diamonds, squares shows SGO simulations and AEOS simulations are shown in filled circles. Colors show the level of substructure in the stellar component using the $\mathcal{C}$ parameter as estimator, i.e., $\mathcal{C} < 0.8$ are high substructured star clusters (red to yellow) and $\mathcal{C} > 8$ are spherical distributions (light green to dark green). Black solid line shows the curve where $\eta = Q_{\rm a}/Q_{\rm f}$ and black dashed line is a fit utilizing only the Plummer background simulations. As soon as substructure is erased data shows that the model start to follow the dashed line, however when substructure is high data seems to be well defined by the model.

We must take into account that our analytical model makes several assumptions considering the potential energy of the system. We assume that the total amount of mass in gas in the region the cluster is present is related to the LSF. Strictly speaking this is not true since this only gives us information about the gaseous mass inside the half mass radius of the cluster giving no information about what happens in the exterior. Our analytical model fails to estimate the relevant gas mass, that has a direct consequence on the value of the $Q_{\rm a}/Q_{\rm f}$ ratio, when η is high (LSF is low). $Q_{\rm a}$ only depends of the stellar component, thus an error in the estimation of the relevant gas mass only affects $Q_{\rm f}$. Fig: 6.12 shows that when η is high ($\eta > 4$), the value of $Q_{\rm f}$ is higher than expected (since the ratio $Q_{\rm a}/Q_{\rm f}$ is lower than what by Eq. 6.20 predicts). But the only way that $Q_{\rm f}$ would be higher than expected is if we overestimate the contribution of the gaseous mass. Then the question is: Why does our model overestimate the amount of gas mass when the LSF is low, even though we are considering a more relevant fraction of the total gas mass? Let's assume that the relevant gas mass for the potential of the cluster is the one inside the full radius of the cluster $R_{\rm full}$ (which is true for a spherical gas distribution), then, for a given LSF, our analytical treatment expect that the fraction of stellar mass remains the same outside $R_{\rm h}$ until the full radius of the cluster, this means that when the LSF is low, i.e., there is a big fraction of gas inside $R_{\rm h}$, the model expects a high amount of gas in the shell between $R_{\rm h}$ and $R_{\rm full}$ as well. Let's take as an example the critical case when the LSF=SFE=0.2, with a total mass in gas of $M_{\rm gas} = 2000$ M$_\odot$ and thus $M_* = 500$ M$_\odot$. Inside $R_{\rm h}$ there is then 250 M$_\odot$ in stars and 1000 M$_\odot$ in gas (LSF=0.2), now the model expect that in the shell between $R_{\rm h}$ and $R_{\rm full}$ there is the same amount of mass in stars and gas than inside $R_{\rm h}$, this will only be true if $R_{\rm full}$ and the radius where the sphere of gas contains 2000 M$_\odot$ ($R_{\rm g,full}$) are the same. However if $R_{\rm full}$ is smaller $R_{\rm g,full}$ (which is usually the case) then the SFE in the outsider shell will be higher than the model expect causing that the model "think" that there is more mass in the outsider shell that it actually is. SFE=LSF is the critical case because for a lower LSF will be impossible to have enough gas mass in the outsider shell simply because there is not enough gas mass in the system. For high LSF there is more chances that the LSF holds outside $R_{\rm h}$, since there is more available gas mass outside $R_{\rm h}$. This is another source of error in the prediction of $f_{\rm bound}$.

This explains why at low LSF the model does not work that well. If we want to avoid this problem we would need to use the full radius of the cluster and the LSF would become the SFE. However it has been shown in previous work that the use of this parameter tells us nothing about the state of the cluster at gas expulsion time since the parameter is a global parameter and does not evolve (see Smith et al., 2011). Even though the full radius of the cluster changes with time (and thus the local SFE) the use of such a long radius would lead into a loss of important information about how much the cluster is concentrated in the centre. Maybe the half mass radius is not the best choice and particularly bad when it is too small. However, it has proven to be a very good estimator even when high levels of substructure are present. Results suggest then that at least with the use of the LSF this is the best we can do.

The LSF is not, however, the only important parameter in our analytical model. Equally important is the virial ratio at gas expulsion time $Q_{\rm f}$ that comes with an important and independent problem. As discussed in Sec. 6.2.2 when $f_{\rm bound}$ is low the value of $Q_{\rm f}$ is not necessarily representative for the entity that will remain bound. A correct measure of $Q_{\rm f}$ involves the knowledge a priori of the stars that will remain bound after gas expulsion. This problem again raises at low LSF where the only way to survive is to have a very low value of $Q_{\rm f}$. In all the simulations performed in this Chapter we did not have that problem since in general $f_{\rm bound}$ is high and LSF> 0.25 where this problem is relevant.

Our results suggest that there are some values where our model can not guaranty a good estimation, that regime raises when: 1) The $LSF < 0.25$ and the virial ratio is not low, i.e., $Q_{\rm f} \gtrsim 0.4$; 2) when the predicted $f_{\rm bound} < 0.3$ then $Q_{\rm f}$ is not reliable ; 3) When the measure of η via estimation ($Q_{\rm a}/Q_{\rm f}$) or direct measure (measuring the LSF, A and B) gives $\eta > 4$.

Otherwise the estimations of $f_{\rm bound}$ are within $\sim 10\%$ of uncertainty no matter if substructure is taking into account or not, as shown in Fig. 6.11.

Chapter 7

Discussion And Conclusions

7.1 Summary

We have have performed simulations of initially substructured young embedded star clusters of $N = 1000$ equal mass stars with a global SFE of 20% with three very different treatments for the background gas: Using static background potentials on Chapter 4; using a dynamically live and initially static Plummer sphere for the gas in Chapter 5; and with initially substructured gas distributions from which the stellar component was born in Chapter 6. In this section we will summarize what we have learned from each numerical experiment.

In Chapter 4 we performed simulations of initially fractal distributions under the influence of three different shapes of background potentials, a Plummer sphere, a very concentrated Plummer sphere and a uniform sphere. We expel the gas instantaneously at early stages of the evolution of the fractal clusters at points where the virial ratio Q was at three extremes points of its evolution: At the first low peak, at the first high peak, and when $Q = 0.5$ at very early stages of the evolution (before $2\ t_{\mathrm{cross}}$) when stellar substructure is dominant. We can summarize the results as follows:

- For early gas expulsion we find the dynamical state of our model star clusters, measured at the time of gas expulsion, plays a key role at influencing cluster survival to gas expulsion. At these early stages, star clusters could be highly super- or sub-virial.

- We found that the f_{bound}-LSF relation can be well approximated by a very simple analytical model. This model matches the simulations best when the dynamical state of the cluster is not at an extreme.
- Clusters which have LSFs in the range 0.2-0.4 (physically reasonable values) are the most sensitive to the pre-gas-expulsion virial ratio.
- Clusters with low virial ratio have a very steep rise in the f_{bound}-LSF trend. For such a clusters it is not possible to accurately predict how much mass will be retained when the LSF~ 0.2 - even knowing both the LSF and the virial ratio.
- We found no difference on the f_{bound}-LSF trend when using background potential of different shapes. The only difference we found is the range in LSF that star clusters populate.

This first study highlights the difficulties faced in trying to determine survival rates of real star clusters to gas expulsion. However, the last item suggests that the shape of the background potential is not relevant, and thus our analytical model may work in a more realistic scenario.

In Chapter 5 we gave to the gas the ability to dynamically evolve and gravitationally interact with the stellar component using an adiabatic equation of state. In order to check how much both components are affected by each other we performed simulations with a range of SFE from 10 to 90%. We made comparisons with the systems evolved with a static background potential with and without gas expulsion. The key results we obtained for this comparison are:

- Only the rearrangement of the stars from stellar fractal distribution to denser spherical systems is not enough to affect the equilibrium of the gas even when 90% of the system's mass is made of stars.
- Fractal clusters collapse into the same radial distributions no matter how strong the background potential is.
- The gravitational interaction between stars and gas causes that stars gives some of their angular momentum to the gas. We find that the amount of angular momentum that the gas obtains does not depend on the initial angular momentum budget of the stellar component.
- The reduction of angular momentum of the stars produces a decrease of their half mass radius, and since the background gas remains stable against the stellar collapse, it results in an increase of the LSF in comparison with the static case. However, this change is not significant.
- There is no difference in the shape of the f_{bound}-LSF trend when using a live gas background. However, our analytical model shows an evident overestimation of the f_{bound} at low LSF and underestimation of f_{bound} at high LSF.

This last numerical experiment shows that the gravitational interaction between stars and gas is not relevant neither for the evolution of the cluster or the response of stars to gas expulsion. The last item, however, suggests that our analytical model does not do a good job at extremes values of LSF, so in the next experiment we attempt to improve the analytical model.

In Chapter 6 we attempt to test our previous results on a more realistic scenario. We performed star formation simulations of equal mass particles that end up in substructured stellar and gaseous distributions of similar size than our previous systems. We used these distributions as initial conditions for subsequent embedded evolution and gas expulsion. In the embedded stage we evolved the background gas using two different treatments: The AEOS simulations we follow the evolution of the gas using an adiabatic equation of state, that quickly forms small clumps that starts to merge into bigger ones; and the SGO simulations where we switch off the self gravity of the gas causing that the gas disperses depending on its initial velocities. We expelled the gas at 0, 1 and 2 Myr of embedded evolution in both setups. The key results can be summarized as follows:

- We improve the simple model introduced in Chapter 4 introducing structure dependent parameters A and B that successfully explain the disagreement in the characteristic shape of the f_{bound}-LSF trend observed and predicted for the Plummer background simulations by the simple analytical model of Chapter 4.
- We shown that the B/A ratio can increase the chances to survive for a cluster if $B/A < 1$ and decrease the survival rates if $B/A > 1$, but it is not enough to explain the high disagreement at low values of LSF.
- It is impossible to measure correctly the virial ratio for clusters that end up with $f_{\mathrm{bound}} < 0.3$ (usually low LSFs). On those clusters, the only way to confidently measure the effective virial ratio is to know the mean velocity of the entity that will stay bound *a priori*.
- When gas disperses in the embedded evolution, clusters that are born with subvirial velocities stay with subvirial velocities for a longer time than in simulations where gas forms clumps that merge into a bigger clump, in this case the embedded cluster reaches equilibrium faster.
- When the gas disperses, it also causes the LSF to raise that, together with the previous finding, results in that all simulations, where the gas disperses (SGO simulations), show f_{bound} close to 1. Simulations that merge faster (AEOS simulations) result in a f_{bound}-LSF trend similar to the trend with simulations using a Plummer background potential with $Q_{\mathrm{f}} = 0.5$.
- Even though the new analytical model works better, it only improves the predictions by a 1% level. This shows that stellar and gaseous substructure are not the principal source of error in the predictions and our model can work equally well in substructured or smooth background envirionments.
- Our analytical model, with or without accounting for substructure, successfully predicts the fraction of stars that remain bound after instantaneous gas expulsion within a $\sim 10\%$ of error, and its more reliable for values where LSF>SFE and the estimated $f_{\mathrm{bound}} > 0.3$.

This results suggests that in a realistic scenario estimations of the fraction of stellar mass that survives gas expulsion are not considerably affected by the stellar or gaseous substructure. The most important parameters that determines if a cluster survives or not are the LSF and the pre-gas-expulsion virial ratio.

7.2 Discussion and Conclusions

We have shown how difficult is to estimate the response of star clusters to gas expulsion. We use very simple models of star clusters and this simplicity enables us to identify what are the most important parameters that rule the infant mortality problem. Our major result is that no matter how realistic the background gas is, the most important parameters to estimate cluster response to gas expulsion are the LSF and the virial ratio at the moment of gas expulsion. We expel the gas instantaneously in all our simulations, since this is the most destructive mode of gas expulsion. Therefore, our results can be seen as estimations of the lower limit of cluster survival.

Even though we treat the background gas in three very different ways, we find that our estimations work equally well in all of them. We find that the interaction between the stars and the gas weakly affects the evolution of the stars, because the gas absorbs some of stars angular momentum. This is not enough to be reflected in the dynamical state of the stellar cluster and only increases the LSF by a small amount. However, we have not tested if the number of SPH particles used in the simulations or the SFE could increase the amount of energy that the gas absorbs. Even if the amount of energy that the star cluster loses is big, our goal is to properly estimate final bound fractions, and we show in Chapter 5 that this effect does not affect our ability to do so.

We performed cheap star forming simulations, that do not have enough resolution to simulate the small details of cluster collapse. However, our resulting embedded star clusters agree with more sophisticated numerical studies, where stars form with subvirial velocities, filamentary structure (e.g. Girichidis et al., 2012) and that global stellar parameters do not depend on the initial conditions of the natal cloud (Bate, 2009; Girichidis et al., 2012; Lomax et al., 2015). After the stars form, we follow the evolution in two equally simplified conditions but at the two extremes of real clusters. We use an adiabatic equation of state to follow the embedded evolution being aware that this is not true in real embedded star clusters. Stars from all masses radiate energy into the surrounding gas. Because of this an adiabatic equation of state fails to model such a cloud, since there is external heating. However, we can see this experiment as an extreme scenario where the stars do not radiate energy into the cloud. On the other hand, we also follow the embedded evolution turning off the self-gravity of the gas. While this is unphysical, this resulting gaseous distribution is similar to what would happen when stars starts to radiate energy into the medium. Stars disperse the surrounding gas suppressing the formation of gas clumps (like in the adiabatic case) thus the final gaseous distributions obtained in our simulations, would be similar to a star cluster without massive stars (which feedback would be so strong that would expel the gas instead of just dispersing it). We are aware that both cases are completely unrealistic, however, what we try to prove is that no matter how substructured, clumpy or dispersed the background gas is, we can still estimate the response of a star cluster to gas expulsion as well as when using a smooth static background potential.

We develop a very simple analytical model in two flavours, with and without accounting for substructure. Both analytical models estimate equally well the amount of mass that cluster retains after gas expulsion, and the two critical factors are the LSF and the pre-gas-expulsion virial ratio Q_{f}. We include two parameters that account for the errors in the estimation of the potential energies due to the particular stellar (A) and gaseous (B) distributions. While we have found that their inclusion actually improves our predictions, in general the improvement is very small. Thus, we conclude that the level of substructure does not considerably affects the response of star clusters to gas expulsion. However, we have only worked with equal mass particles. We must be aware that we have not reached extremes values of B/A yet, the inclusion of an initial mass function and subsequent mass segregation may lead to extremes values of B/A which could considerably affect the survival rate.

Our analytical models are based on very challenging observables. While it is not unconceivable to measure the LSF by deprojection, there is not yet a reliable method of measuring embedded star cluster's virial ratio. This last parameter is crucial to estimate the bound mass, even when accounting for substructure. An interesting result is that in our analytical model, the parameter η which depends of the LSF and the structural parameters A and B, can be estimated if we can measure the virial ratio before gas expulsion (Q_f) and just after gas expulsion (Q_a) through the relation $Q_\mathrm{a}/Q_\mathrm{f} = \eta$. If it is possible to measure Q_f, it would even be easier to measure Q_a since we don't need to consider the mass of the gas. Of course, it is very unlikely to catch a cluster just at the moment of gas expulsion, this method would give us an idea of the current *effective* bound mass of an embedded star cluster. The relation between the pre and post-virial ratio and the parameter η also expose the major error in our analytical model (see Fig. 6.12). We assume that the LSF represents the relative amount of mass in stars and gas in the cluster, however, this is only true inside the half mass radius of the cluster, thus in our analytical model the total amount of gas is not well estimated.

Figure 7.1 shows two scenarios one with high LSF and also high f_bound (left) and another with low LSF and a low f_bound (right). In those examples, the LSF defined inside R_h is different of the fraction of stars relative to the gas outside R_h. In the left case, the fraction of stars to gas outside R_h (green shaded area) is smaller than the LSF (red shaded area). In the right case, the fraction of stars to gas outside R_h (red shaded area) is bigger because most of the gas mass is inside R_h (green shaded area) where the LSF is low, and there is not enough gas mass in the system to maintain the stars to gas ratio outside R_h.

Note that:

$$\eta \propto \frac{1}{Q_\mathrm{f}} \propto M_\mathrm{gas} \tag{7.1}$$

then, if Q_f is bigger than expected for a given η, means that M_gas is been underestimated by the model. And thus the contribution to the potential energy from the gas is bigger than what the model accounts. Since we measure Q_f, this results in a underestimation of the kinetic energy of the stars and a consequent overestimation of f_bound. In contrast, if Q_f is lower than expected for a given η, M_gas is overestimated and thus the kinetic energy of the star cluster is overestimated causing the model to predict a lower f_bound than by knowing the correct amount of gas mass.

This problem is present at all values of LSF, however when the LSF $\sim$ SFE this problem becomes more significant since it is more probable that the SFE outside the half mass radius is lower than the LSF since most of the gas mass is actually inside. This results in a overestimation of the bound fraction at LSF $\sim$ SFE.

In general, a low LSF results in a low bound fraction (if Q_f is not too small). When the estimated bound fraction is low ($f_\mathrm{bound} < 0.3$) measuring the virial ratio is not only a observational challenge. As we show in Fig. 7.1, in the case with a high f_bound , the mean velocity of the clump that will remain bound (red arrow) is similar to the mean velocity

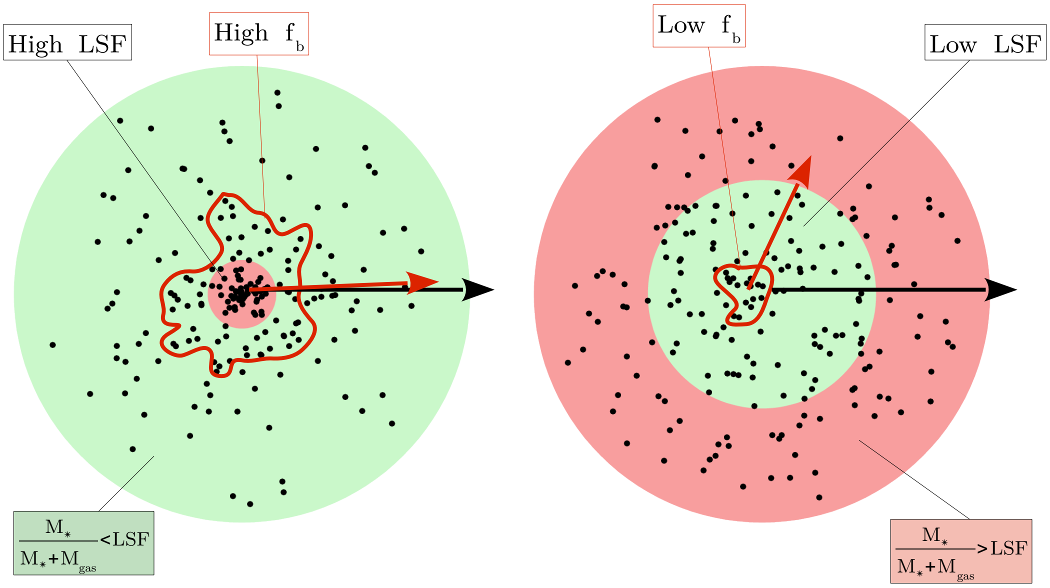

Figure 7.1: Schematic diagram showing the limitations of our analytical model in two extreme scenarios. In the left the cluster have a high LSF (red shaded area) and a high f_{bound} where the cluster that will remain bound is enclosed by the thick red line. Since f_{bound} is high the mean velocity of the bound cluster (red arrow) is similar to the mean velocity of the whole cluster (black arrow). On the right the cluster has a low LSF since the R_{h} is bigger and there is more gas mass inside. It this case f_{bound} is low and the main velocity of the clump that will remain bound is different that the mean velocity of the whole cluster, the virial ratio of the cluster will be heavily affected if considering the velocity of the clump or the velocity of the whole cluster. The gas mass inside R_{h} in the left larger than outside R_{h} (green shaded area) then we underestimate the gaseous mass in the analytical model. In the right case, the gas mass inside R_{h} (green shaded area) is smaller than in the outside (red shaded area), and thus we underestimate the gas mass in the analytical model. In both cases the use of the LSF does not give information about the outside, making our analytical model to (under)overestimate the amount of gas in the cluster.

of the whole cluster (black arrow) since they share most of the stars. In the case with a low f_{bound}, the clump that survives only have a few stars in comparison with the whole cluster, thus the mean velocity of the clump that survives is very likely to be different of the mean velocity of the whole cluster. A confident measure of Q_{f} comes with the need of removing the mean velocity of the survival clump that, when the cluster is embedded in the gas, is technically impossible to know a priori. This is a challenge even in our simulations where we have all the data we need in our hands. If the estimated bound fraction is low and substructure is present, there are several potential small survivors at the moment of gas expulsion, is not possible to know which of those candidates will be the bigger clump or even harder, which stars will finally become part of the clump. Therefore, estimating the correct zero velocity is not an easy task and maybe impossible for real star clusters.

However, we have found that when clusters form with subvirial velocities, the survival to gas expulsion will be determined by how the LSF and Q_{f} evolve before gas expulsion. Our simulations show that in the absence of radiative feedback, the gas tends to form clumps that quickly merge. This mergers produce that the cluster reaches equilibrium very fast and then the survival rate will be mostly determined by the LSF that the cluster reaches when (depending of the size of the cluster) the first supernovae explodes.

However, stars do radiate energy into the medium once they are born. Considering that, embedded clusters are not likely to form clumps of gas, they are more likely to disperse the gas into the medium. In such scenario, our simulations suggest that the star clusters have higher chances to have low virial ratios since the background potential of the gas is not strong enough to cause mergers on short time-scales. If this is the case then stars can survive quite well explosive gas expulsion at all values of LSF (that in this scenario will be higher). Our results suggest that cluster have several chances to survive gas expulsion, even when gas is removed violently. Thus, maybe gas expulsion is not the main responsible cause of the infant mortality problem. However, this is not the last word about it and there are several other parameters that need to be explored, which could change the results. They need to be studied in a future work.

Bibliography

Aarseth, S. J., *Gravitational N-Body Simulations* (2003).

Agertz, O., Moore, B., Stadel, J., Potter, D., Miniati, F., Read, J., Mayer, L., Gawryszczak, A., Kravtsov, A., Nordlund, Å., Pearce, F., Quilis, V., Rudd, D., Springel, V., Stone, J., Tasker, E., Teyssier, R., Wadsley, J. and Walder, R., 2007. *Fundamental differences between SPH and grid methods.* MNRAS, 380, pp. 963–978.

Allen, L., Megeath, S. T., Gutermuth, R., Myers, P. C., Wolk, S., Adams, F. C., Muzerolle, J., Young, E. and Pipher, J. L., 2007. *The Structure and Evolution of Young Stellar Clusters.* Protostars and Planets V, pp. 361–376.

Allison, R. J., Goodwin, S. P., Parker, R. J., Portegies Zwart, S. F., de Grijs, R. and Kouwenhoven, M. B. N., 2009. *Using the minimum spanning tree to trace mass segregation.* MNRAS, 395, pp. 1449–1454.

Barnes, J. and Hut, P., 1986. *A hierarchical O(N log N) force-calculation algorithm.* Nature, 324, pp. 446–449.

Bastian, N., Covey, K. R. and Meyer, M. R., 2010. *A Universal Stellar Initial Mass Function? A Critical Look at Variations.* ARA&A, 48, pp. 339–389.

Bate, M. R., 2009. *The dependence of star formation on initial conditions and molecular cloud structure.* MNRAS, 397, pp. 232–248.

Bate, M. R., Bonnell, I. A. and Bromm, V., 2003. *The formation of a star cluster: predicting the properties of stars and brown dwarfs.* MNRAS, 339, pp. 577–599.

Bate, M. R., Bonnell, I. A. and Price, N. M., 1995. *Modelling accretion in protobinary systems.* MNRAS, 277, pp. 362–376.

Baumgardt, H. and Kroupa, P., 2007. *A comprehensive set of simulations studying the influence of gas expulsion on star cluster evolution.* MNRAS, 380, pp. 1589–1598.

Binney, J. and Tremaine, S., *Galactic dynamics* (Princeton, NJ, Princeton University Press, 1987, 747 p., 1987).

Boily, C. M. and Kroupa, P., 2003. *The impact of mass loss on star cluster formation - I. Analytical results.* MNRAS, 338, pp. 665–672.

Bondi, H. and Hoyle, F., 1944. *On the mechanism of accretion by stars.* MNRAS, 104, p. 273.

Bressert, E., Bastian, N., Gutermuth, R., Megeath, S. T., Allen, L., Evans, N. J., II, Rebull, L. M., Hatchell, J., Johnstone, D., Bourke, T. L., Cieza, L. A., Harvey, P. M., Merin, B., Ray, T. P. and Tothill, N. F. H., 2010. *The spatial distribution of star formation in the solar neighbourhood: do all stars form in dense clusters?* MNRAS, 409, pp. L54–L58.

Carpenter, J. M., 2000. *2MASS Observations of the Perseus, Orion A, Orion B, and Monoceros R2 Molecular Clouds.* AJ, 120, pp. 3139–3161.

Cartwright, A., 2009. *Measuring clustering in 2dv space.* MNRAS, 400, pp. 1427–1430.

Cartwright, A. and Whitworth, A. P., 2004. *The statistical analysis of star clusters.* MNRAS, 348, pp. 589–598.

Chatterjee, S., Rasio, F. A., Sills, A. and Glebbeek, E., 2013. *Stellar Collisions and Blue Straggler Stars in Dense Globular Clusters.* ApJ, 777, 106.

Dale, J. E., Ercolano, B. and Bonnell, I. A., 2013. *Ionizing feedback from massive stars in massive clusters - III. Disruption of partially unbound clouds.* MNRAS, 430, pp. 234–246.

Efremov, Y. N. and Elmegreen, B. G., 1998. *Hierarchical star formation from the time-space distribution of star clusters in the Large Magellanic Cloud.* MNRAS, 299, pp. 588–594.

Elmegreen, B. G., 1983. *Quiescent formation of bound galactic clusters.* MNRAS, 203, pp. 1011–1020.

Elmegreen, B. G., Efremov, Y., Pudritz, R. E. and Zinnecker, H., 2000. *Observations and Theory of Star Cluster Formation.* Protostars and Planets IV, p. 179.

Elmegreen, B. G. and Elmegreen, D. M., 2001. *Fractal Structure in Galactic Star Fields.* AJ, 121, pp. 1507–1511.

Elmegreen, B. G. and Lada, C. J., 1977. *Sequential formation of subgroups in OB associations.* ApJ, 214, pp. 725–741.

Evans, N. J., II, Dunham, M. M., Jørgensen, J. K., Enoch, M. L., Merín, B., van Dishoeck, E. F., Alcalá, J. M., Myers, P. C., Stapelfeldt, K. R., Huard, T. L., Allen, L. E., Harvey, P. M., van Kempen, T., Blake, G. A., Koerner, D. W., Mundy, L. G., Padgett, D. L. and Sargent, A. I., 2009. *The Spitzer c2d Legacy Results: Star-Formation Rates and Efficiencies; Evolution and Lifetimes.* ApJS, 181, 321-350.

Falgarone, E., Phillips, T. G. and Walker, C. K., 1991. *The edges of molecular clouds - Fractal boundaries and density structure.* ApJ, 378, pp. 186–201.

Farias, J. P., Smith, R., Fellhauer, M., Goodwin, S., Candlish, G. N., Blaña, M. and Dominguez, R., 2015. *The difficult early stages of embedded star clusters and the importance of the pre-gas expulsion virial ratio.* MNRAS, 450, pp. 2451–2458.

Federrath, C. and Klessen, R. S., 2012. *The Star Formation Rate of Turbulent Magnetized Clouds: Comparing Theory, Simulations, and Observations.* ApJ, 761, 156.

Federrath, C., Klessen, R. S. and Schmidt, W., 2009. *The Fractal Density Structure in Supersonic Isothermal Turbulence: Solenoidal Versus Compressive Energy Injection.* ApJ, 692, pp. 364–374.

Fellhauer, M. and Kroupa, P., *A possible formation scenario for the heavy-weight young cluster W3 in NGC 7252.* In de Grijs, R. and González Delgado, R. M., eds., *Starbursts: From 30 Doradus to Lyman Break Galaxies*, vol. 329 of *Astrophysics and Space Science Library*, pp. 18P–+ (2005).

Fujii, M., Iwasawa, M., Funato, Y. and Makino, J., 2007. *BRIDGE: A Direct-Tree Hybrid N-Body Algorithm for Fully Self-Consistent Simulations of Star Clusters and Their Parent Galaxies.* PASJ, 59, pp. 1095–.

Gerritsen, J. P. E. and Icke, V., 1997. *Star formation in N-body simulations. I. The impact of the stellar ultraviolet radiation on star formation.* A&A, 325, pp. 972–986.

Geyer, M. P. and Burkert, A., 2001. *The effect of gas loss on the formation of bound stellar clusters.* MNRAS, 323, pp. 988–994.

Gingold, R. A. and Monaghan, J. J., 1977. *Smoothed particle hydrodynamics - Theory and application to non-spherical stars.* MNRAS, 181, pp. 375–389.

Girichidis, P., Federrath, C., Allison, R., Banerjee, R. and Klessen, R. S., 2012. *Importance of the initial conditions for star formation - III. Statistical properties of embedded protostellar clusters.* MNRAS, 420, pp. 3264–3280.

Goodwin, S. P., 1997. *Residual gas expulsion from young globular clusters.* MNRAS, 284, pp. 785–802.

Goodwin, S. P., 2009. *The effect of the dynamical state of clusters on gas expulsion and infant mortality.* Ap&SS, 324, pp. 259–263.

Goodwin, S. P. and Bastian, N., 2006. *Gas expulsion and the destruction of massive young clusters.* MNRAS, 373, pp. 752–758.

Goodwin, S. P. and Whitworth, A. P., 2004. *The dynamical evolution of fractal star clusters: The survival of substructure.* A&A, 413, pp. 929–937.

Gutermuth, R. A., Megeath, S. T., Myers, P. C., Allen, L. E., Pipher, J. L. and Fazio, G. G., 2009. *A Spitzer Survey of Young Stellar Clusters Within One Kiloparsec of the Sun: Cluster Core Extraction and Basic Structural Analysis.* ApJS, 184, pp. 18–83.

Harris, W. E., 1996. *A Catalog of Parameters for Globular Clusters in the Milky Way.* Astron.J., 112, p. 1487.

Heggie, D. and Hut, P., *The Gravitational Million-Body Problem: A Multidisciplinary Approach to Star Cluster Dynamics* (2003).

Heitsch, F., Mac Low, M.-M. and Klessen, R. S., 2001. *Gravitational Collapse in Turbulent Molecular Clouds. II. Magnetohydrodynamical Turbulence.* ApJ, 547, pp. 280–291.

Hernquist, L. and Katz, N., 1989. *TREESPH - A unification of SPH with the hierarchical tree method.* ApJS, 70, pp. 419–446.

Hills, J. G., 1980. *The effect of mass loss on the dynamical evolution of a stellar system - Analytic approximations.* ApJ, 235, pp. 986–991.

Holtzman, J. A., Faber, S. M., Shaya, E. J., Lauer, T. R., Groth, J., Hunter, D. A., Baum, W. A., Ewald, S. P., Hester, J. J., Light, R. M., Lynds, C. R., O'Neil, E. J., Jr. and Westphal, J. A., 1992. *Planetary Camera observations of NGC 1275 - Discovery of a central population of compact massive blue star clusters.* AJ, 103, pp. 691–702.

Jeffries, R. D., Littlefair, S. P., Naylor, T. and Mayne, N. J., 2011. *No wide spread of stellar ages in the Orion Nebula Cluster.* MNRAS, 418, pp. 1948–1958.

King, I. R., 1966. *The structure of star clusters. III. Some simple dynamical models.* AJ, 71, p. 64.

Kittel, C., Knight, W. D., Ruderman, M. A., Helmholz, A. C. and Moyer, B. J., *Mechanics* (1973).

Klessen, R. S. and Burkert, A., 2000. *The Formation of Stellar Clusters: Gaussian Cloud Conditions. I.* ApJS, 128, pp. 287–319.

Klessen, R. S. and Burkert, A., 2001. *The Formation of Stellar Clusters: Gaussian Cloud Conditions. II.* ApJ, 549, pp. 386–401.

Klessen, R. S., Burkert, A. and Bate, M. R., 1998. *Fragmentation of Molecular Clouds: The Initial Phase of a Stellar Cluster.* ApJL, 501, pp. L205–L208.

Kroupa, P., Aarseth, S. and Hurley, J., 2001. *The formation of a bound star cluster: from the Orion nebula cluster to the Pleiades.* MNRAS, 321, pp. 699–712.

Kruijssen, J. M. D., 2012. *On the fraction of star formation occurring in bound stellar clusters.* MNRAS, 426, pp. 3008–3040.

Lada, C. J. and Lada, E. A., 2003. *Embedded Clusters in Molecular Clouds.* ARA&A, 41, pp. 57–115.

Lada, C. J., Margulis, M. and Dearborn, D., 1984. *The formation and early dynamical evolution of bound stellar systems.* ApJ, 285, pp. 141–152.

Larsen, S. S. and Richtler, T., 1999. *Young massive star clusters in nearby galaxies . I. Identification and general properties of the cluster systems.* A&A, 345, pp. 59–72.

Li, Y., Klessen, R. S. and Mac Low, M.-M., 2003. *The Formation of Stellar Clusters in Turbulent Molecular Clouds: Effects of the Equation of State.* ApJ, 592, pp. 975–985.

Lomax, O., Whitworth, A. P. and Hubber, D. A., 2015. *On the effects of solenoidal and compressive turbulence in pre-stellar cores.* MNRAS, 449, pp. 662–669.

Lucy, L. B., 1977. *A numerical approach to the testing of the fission hypothesis.* AJ, 82, pp. 1013–1024.

Maxwell, J. E., Cohn, H. N., Lugger, P. M., Heinke, C. O. and Budac, S. A., *X-ray Binaries in the Ultrahigh Collision Rate Globular Cluster NGC 6388.* In *American Astronomical Society Meeting Abstracts #219*, vol. 219 of *American Astronomical Society Meeting Abstracts*, p. 153.02 (2012).

Mellema, G., Eulderink, F. and Icke, V., 1991. *Hydrodynamical models of aspherical planetary nebulae.* A&A, 252, pp. 718–732.

Monaghan, J. J., 1992. *Smoothed particle hydrodynamics.* ARA&A, 30, pp. 543–574.

Narayanan, V. K. and Gould, A., 1999. *A Precision Test of HIPPARCOS Systematics toward the Hyades.* ApJ, 515, pp. 256–264.

Padoan, P., Federrath, C., Chabrier, G., Evans, N. J., II, Johnstone, D., Jørgensen, J. K., McKee, C. F. and Nordlund, Å., 2014. *The Star Formation Rate of Molecular Clouds.* Protostars and Planets VI, pp. 77–100.

Padoan, P., Haugbølle, T. and Nordlund, Å., 2012. *A Simple Law of Star Formation.* ApJL, 759, L27.

Padoan, P. and Nordlund, Å., *Theory of the Star Formation Rate.* In Alves, J., Elmegreen, B. G., Girart, J. M. and Trimble, V., eds., *Computational Star Formation*, vol. 270 of *IAU Symposium*, pp. 347–354 (2011).

Parker, R. J., Wright, N. J., Goodwin, S. P. and Meyer, M. R., 2014. *Dynamical evolution of star-forming regions.* MNRAS, 438, pp. 620–638.

Parmentier, G., 2014. *Local-density driven clustered star formation: Model and (some) implications.* Astronomische Nachrichten, 335, pp. 543–548.

Parmentier, G. and Pfalzner, S., 2013. *Local-density-driven clustered star formation.* A&A, 549, A132.

Pelupessy, F. I., 2005. *Thesis: Numerical Studies of the Interestellar Medium on Galactic Scales.* Ph.D. thesis, Leiden Univerisy.

Pelupessy, F. I., van der Werf, P. P. and Icke, V., 2004. *Periodic bursts of star formation in irregular galaxies.* A&A, 422, pp. 55–64.

Pelupessy, F. I., van Elteren, A., de Vries, N., McMillan, S. L. W., Drost, N. and Portegies Zwart, S. F., 2013. *The Astrophysical Multipurpose Software Environment.* A&A, 557, A84.

Portegies Zwart, S., McMillan, S. L. W., van Elteren, E., Pelupessy, I. and de Vries, N., 2013. *Multi-physics simulations using a hierarchical interchangeable software interface.* Computer Physics Communications, 183, pp. 456–468.

Price, D. J., 2011. *SPLASH: An Interactive Visualization Tool for Smoothed Particle Hydrodynamics Simulations.* Astrophysics Source Code Library.

Rasio, F. A. and Lombardi, J. C., Jr., 1999. *Smoothed particle hydrodynamics calculations of stellar interactions.* Journal of Computational and Applied Mathematics, 109, pp. 213–230.

Schmeja, S. and Klessen, R. S., 2006. *Evolving structures of star-forming clusters.* A&A, 449, pp. 151–159.

Smith, R., Fellhauer, M., Goodwin, S. and Assmann, P., 2011. *Surviving infant mortality in the hierarchical merging scenario.* MNRAS, 414, pp. 3036–3043.

Smith, R., Goodwin, S., Fellhauer, M. and Assmann, P., 2013. *Infant mortality in the hierarchical merging scenario: dependence on gas expulsion time-scales.* MNRAS, 428, pp. 1303–1311.

Springel, V., 2005. *The cosmological simulation code GADGET-2.* MNRAS, 364, pp. 1105–1134.

Springel, V., Yoshida, N. and White, S. D. M., 2001. *GADGET: a code for collisionless and gasdynamical cosmological simulations.* New Astron., 6, pp. 79–117.

Stone, J. M. and Norman, M. L., 1992. *ZEUS-2D: A radiation magnetohydrodynamics code for astrophysical flows in two space dimensions. I - The hydrodynamic algorithms and tests.* ApJS, 80, pp. 753–790.

Tsitali, A. E., Bourke, T. L., Peterson, D. E., Myers, P. C., Dunham, M. M., Evans, N. J., II and Huard, T. L., 2010. *The Spitzer c2d Survey of Nearby Dense Cores. X. Star Formation in L673 and CB188.* ApJ, 725, 2461-2479.

Verschueren, W. and David, M., 1989. *The effect of gas removal on the dynamical evolution of young stellar clusters.* A&A, 219, pp. 105–120.

Vogelaar, M. G. R. and Wakker, B. P., 1994. *Measuring the fratal structure of interstellar clouds.* A&A, 291, pp. 557–568.

Wetzstein, M., Nelson, A. F., Naab, T. and Burkert, A., 2009. *VineA Numerical Code for Simulating Astrophysical Systems Using Particles. I. Description of the Physics and the Numerical Methods.* ApJS, 184, pp. 298–325.

Whitmore, B. C., *Globular clusters as distance indicators.* In Livio, M., Donahue, M. and Panagia, N., eds., *The Extragalactic Distance Scale*, pp. 254–272 (1997).

Whitmore, B. C. and Schweizer, F., 1995. *Hubble space telescope observations of young star clusters in NGC-4038/4039, 'the antennae' galaxies.* AJ, 109, pp. 960–980.

Wilking, B. A. and Lada, C. J., 1983. *The discovery of new embedded sources in the centrally condensed core of the Rho Ophiuchi dark cloud - The formation of a bound cluster.* ApJ, 274, pp. 698–716.

Zuckerman, B. and Evans, N. J., II, 1974. *Models of massive molecular clouds.* ApJL, 192, pp. L149–L152.